

**INVESTIGATION OF GRAIN SIZE EFFECTS
ON THE DIFFUSION RATE OF
NANOPOROUS METAL ORGANIC FRAMEWORKS**

M.Sc. THESIS

Fatih KUZAK

Department of Metallurgy and Material Engineering

Materials Engineering Programme

SEPTEMBER 2013

**INVESTIGATION OF GRAIN SIZE EFFECTS
ON THE DIFFUSION RATE OF
NANOPOROUS METAL ORGANIC FRAMEWORKS**

M.Sc. THESIS

**Fatih KUZAK
(506101410)**

Department of Metallurgy and Material Engineering

Materials Engineering Programme

Thesis Advisor: Assoc. Prof. Dr. Özgül KELEŞ

SEPTEMBER 2013

**NANO GÖZENEKLİ METAL ORGANİK YAPILARDA
TANE BOYUTUNUN DİFUZYON HIZINA ETKİSİ**

YÜKSEK LİSANS TEZİ

**Fatih KUZAK
(506101410)**

Metalurji ve Malzeme Mühendisliği Anabilim Dalı

Malzeme Mühendisliği Programı

Tez Danışmanı: Assoc. Prof. Dr. Özgül KELEŞ

EYLÜL 2013

Fatih KUZAK, a M.Sc. student of ITU Institute of Science and Technology 506101410 successfully defended the thesis entitled “**INVESTIGATION OF GRAIN SIZE EFFECTS ON THE DIFFUSION RATE OF NANOPOROUS METAL ORGANIC FRAMEWORKS**”, which he/she prepared after fulfilling the requirements specified in the associated legislations, before the jury whose signatures are below.

Thesis Advisor : **Assoc. Prof. Dr. Özgül KELEŞ**
Istanbul Technical University

Jury Members : **Prof. Dr. Sebahattin GÜRMEN**
Istanbul Technical University

Prof. Dr. Müzeyyen MARŞOĞLU
Yıldız Technical University

Date of Submission : **4 September 2013**
Date of Defense : **25 September 2013**

“tiger got to hunt, bird got to fly; man got to sit and wonder ‘why, why, why?’ tiger got to sleep, bird got to land; man got to tell himself he understand.”

– Kurt Vonnegut, *Cat’s Craddle*.

FOREWORD

This thesis have been written in the department of Modern Magnetic Materials in Max Planck Institute for Intelligent Systems (MPI-IS), in Germany, during my Erasmus-Student Exchange Program 2011-2012, as completion to the master Material Engineering at Istanbul Technical University. First of all, I would like to thank Assoc. Prof. Dr. Özgül KELEŞ, who is my thesis supervisor at Istanbul Technical University, for her great effort on reviewing and specifying the critical points in the thesis during my work. Of course, I would like to kindly thank Dr. Michael HIRSCHER, my advisor in Max Planck Institute, who has provided me a friendly environment to develop myself in sciences, and supporting me to complete my master thesis under his supervision. Special thanks to Hyunchul Oh, for his remarkable guidance and great effort on me to find the way out to assemble my studies. There is always something to regulate and/or calibrate. Bernd Ludescher, thank you for the thoughtful technical support. To all my friends from all over the world, most of you contributed to my psychological situation with your motivations, and wishes. You are all well missed. Great thanks to both universities Istanbul Technical University and Universität Stuttgart for granting me with exceptional experiences both scientific and social communication with the people around the world by providing Erasmus-Student Exchange Program.

September 2013

Fatih KUZAK

TABLE OF CONTENTS

	<u>Page</u>
FOREWORD.....	ix
TABLE OF CONTENTS.....	xi
ABBREVIATIONS	xiii
LIST OF TABLES	xv
LIST OF FIGURES	xvii
SUMMARY	xxi
ÖZET	xxiii
1. INTRODUCTION	1
1.1 Hydrogen Storage	3
1.2 Storage Methods	4
1.2.1 Chemical storage	5
1.2.2 Physical storage	6
1.2.2.1 Adsorption measurements	8
Isotherms	11
1.2.2.2 Surface area	13
Henry model.....	14
Langmuir isotherm model	14
BET isotherm model	16
1.2.2.3 Isosteric heat of adsorption.....	18
1.3 Fundamentals of Diffusion	19
1.3.1 Random walk, self- and transport diffusion	21
1.3.2 Diffusion in porous media	24
1.3.3 Macropore diffusion mechanisms	26
1.3.3.1 Knudsen mechanism.....	27
1.3.3.2 Viscous flow.....	28
1.3.3.3 Molecular diffusion.....	29
1.3.3.4 Surface diffusion.....	29
1.3.4 Measurement techniques	30
1.3.4.1 Sorption kinetics	32
1.4 Metal-Organic Frameworks.....	33
1.4.1 Production methods	41
1.4.1.1 Solvothermal synthesis	41
1.4.1.2 Microwave irradiation synthesis	42
2. EXPERIMENTAL METHOD.....	45
2.1 Sample Preparation.....	45

2.2 Sample Characterization.....	46
2.2.1 Sem & xrd investigations.....	46
2.2.2 High pressure hydrogen storage	48
2.2.2.1 Measurement device	48
2.2.2.2 Calibration	53
2.2.2.3 Procedures for measurements	56
3. RESULTS AND DISCUSSION	63
3.1 H ₂ Uptake Results	63
3.1.1 Heat of adsorption	69
3.2 Kinetic Evaluations.....	71
4. CONCLUSION	83
REFERENCES.....	85
APPENDICES.....	93
APPENDIX A.1	95
APPENDIX A.2	98
CURRICULUM VITAE.....	101

ABBREVIATIONS

ABDC	: <i>2-aminobenzene-1,4-dicarboxylate</i>
BBTA	: <i>benzobistriazolate</i>
BDC	: <i>benzenedicarboxylic acid</i>
BTB	: <i>benzenetribenzoate</i>
BTC	: <i>1,3,5-benzenetricarboxylic acid;</i>
DEF	: <i>N, N-diethyl formamide</i>
DMA	: <i>N,N'-dimethylacetamide</i>
DMF	: <i>N, N-dimethyl formamide</i>
CuTEI	: <i>Cu5-((triisopropylsilyl)ethynyl)isophthalic acid</i>
H2-BBTA	: <i>1H,5H-benzo(1,2-d:4,5-d')bistriazole</i>
H2-BTTD	: <i>bis(1H-1,2,3- triazolo[4,5-b],[4',5'-i])dibenzo[1,4]dioxin</i>
MFU	: Metal Organic Framework Ulm
NDC	: <i>naphthalenedicarboxylate</i>
PBPC	: <i>pyridine-3,5-bis(phenyl-4-carboxylic acid</i>
PEM	: Proton Exchange Membrane
PID	: Proportion Integral Derivative
SBU	: Secondary Building Unit
TMBDC	: <i>2,3,5,6-tetramethyl-1,4-benzenedicarboxylate)</i>
XRD	: X-Ray Diffractometry
ZIF	: Zeolitic Imidazole Framework

LIST OF TABLES

	<u>Page</u>
Table 1.1 : Number of MOFs with their production methods and H ₂ sorption data.....	43
Table 2.1 : Adsorption and desorption measurement characteristics of MFU4.Br-1 and MFU4.Br-2.....	59
Table 2.1 : Adsorption and desorption measurement characteristics of MFU4.Br-1 and MFU4.Br-2.....	60
Table 3.1 : H ₂ uptakes in wt% and corresponding measurement times of MFU4.Br-1 and MFU4.Br-2.....	68
Table 3.2 : H ₂ uptake measurement completion time of MFU4.Br-1 and MFU4.Br-2.....	76
Table 3.3 : Diffusion Coefficients of MFU4.Br-1 and MFU4.Br-2 at different temperatures.....	80

LIST OF FIGURES

	<u>Page</u>
Figure 1.1 : Specific Energy Comparison Between Fuel Cell Technologies and Different Battery Types	2
Figure 1.2 : Hydrogen storage options for on-board applications.....	4
Figure 1.3 : A depiction of chemisorption into a material	6
Figure 1.4 : A depiction of physisorption on surfaces [13].....	7
Figure 1.5 : Presentation of van der Waals Forces	8
Figure 1.6 : A Depiction of Excess, Absolute, Total Uptake and Pore with Adsorbed Molecules	10
Figure 1.7 : The IUPAC Classification of Adsorption Isotherms for Gas-Solid Equilibria	12
Figure 1.8 : Diffusion of particles, they spread over the volume to eliminate concentration gradient.....	19
Figure 1.9 : A depiction of Fick's First and Second Law	20
Figure 1.10 : Schematic representations for the measurement of (a) transport diffusion and of self-diffusion by (b) following the (counter-) flux of differently labeled molecules (red, green) or by (c) recording the displacement of the individual molecules	23
Figure 1.11 : Micropore and Macropore Diffusion	24
Figure 1.12 : Intracrystalline diffusion paths in MFU4.Br structure	25
Figure 1.13 : Effective diffusion mechanism and corresponding activation energy according to the pore size	26
Figure 1.14 : Knudsen Diffusion Mechanism: Magenta balls represent the diffusing particles in a pore whereas the green ball refers to particle that is diffusing on the surface	27
Figure 1.15 : A depiction of Viscous Flow	28
Figure 1.16 : Experimental diffusion measurement techniques for porous media	31
Figure 1.17 : Zeolite Structure	33
Figure 1.18 : Assembly of nodes and linkers to form structures: Nodes on the left top, and linkers on the top right, forming metal-organic structures in the middle	34
Figure 1.19 : MOF-5 Crystal Structure: Metal Zn_4O node and carboxylate linker (left), and the complete structure (right).....	35
Figure 1.20 : Examples of Metal-Organic Frameworks: a)MOF-177 b)IRMOF-8 c) MIL-53s (<i>Matériaux de l'Institut Lavoisier</i>) d) $Zn_2 - (bdc)_2(dabco)$ ($dabco = 1,4 - diazabicyclo[2.2.2]octane$)	36

Figure 1.21: Triazolate based linkers: 1,2,3-Triazole, 1,2,4-triazole, and the coordination modes of 1,2,4-triazole and 1,2,4-triazolate	37
Figure 1.22: MFU4 Crystal Structure	37
Figure 1.23: Excess high pressure H ₂ uptake capacities at 77 K versus BET surface areas for some highly porous MOFs	39
Figure 1.24: A depiction of gate opening process by adsorptive pressure	40
Figure 2.1 : SEM Images of the Samples at 20000x magnification. Left: MFU4.Br-1 Right: MFU4.Br-2	46
Figure 2.2 : SEM Images of the Samples at 50000x magnification. Left: MFU4.Br-1 Right: MFU4.Br-2	46
Figure 2.3 : A Comparison of XRD Results between MFU4 Samples. Red: MFU4 Blue: MFU4.Br	47
Figure 2.4 : XRD Results of the Samples. Red: MFU4.Br-1 Blue: MFU4.Br-2 .	48
Figure 2.5 : Representation of operating system of PCT.	49
Figure 2.6 : Cooling systems for the PCTPro-2000. Cryostat Bath for cooling with liquid nitrogen or liquid argon (a). Cooling system for temperatures above 87 K (b).	52
Figure 2.7 : The adsorption measurements at 87 K. MFU4.Br-1, blue spheres show the adsorption isotherm at 87 K with liquid argon, and the white spheres show the adsorption isotherm at adjusted liquid nitrogen temperature ~87 K (a). MFU4.Br-2 blue spheres show the adsorption isotherm at 87 K with liquid argon and the red plus signs show the adsorption isotherm at adjusted liquid nitrogen temperature ~87 K (b).	53
Figure 2.8 : The adsorption measurements with different sea sand weights at different temperatures	55
Figure 2.9 : The slope of adsorption measurements with different sea sand masses and at different temperatures	56
Figure 2.10: Progress of the PCT Measurement	57
Figure 3.1 : Full isotherm of MFU4.Br-1 at 77 K ¹ , 87 K ² , 97 K ⁴ , 112 K ⁶ , 127 K ⁷ , and RT ⁸	63
Figure 3.2 : Adsorption and desorption measurements of MFU4.Br-1 at 77 K, 87 K, and 97 K: The full symbols show adsorption part of the measurement whereas the open symbols indicate the desorption part. The small numbers in uppcase refers to the measurement number in Table 2.1	65
Figure 3.3 : Full isotherm of MFU4.Br-2 at 77 K ⁸ , 87 K ¹⁰ , 97 K ¹³ , 112 K ¹⁴ , 127 K ¹⁵ , and RT ¹⁶	67
Figure 3.4 : Adsorption and desorption measurements of MFU4.Br-2 at 77 K, and 87 K: The full symbols show adsorption part of the measurement whereas the open symbols indicate the desorption part. The small numbers in uppcase refers to the measurement number in Table 2.1	67

Figure 3.5 :	Excess uptake comparison between MFU4.Br-1 and MFU4.Br-2 at reversible temperatures, 112 K and 127 K. Same colors indicate same temperatures whereas same symbols indicate the uptake data for that sample at different temperatures. L and S in the figure, indicate the mean particle size as large and small, respectively.	69
Figure 3.6 :	Heat of adsorption of MFU4.Br-1 (left) and MFU4.Br-2 (right).	70
Figure 3.7 :	Kinetic Behavior Comparison between MFU4.Br-1 and MFU4.Br-2 at 77 K	71
Figure 3.8 :	Kinetic Behavior Comparison between MFU4.Br-1 and MFU4.Br-2 at 87 K	72
Figure 3.9 :	Kinetic Behavior Comparison between MFU4.Br-1 and MFU4.Br-2 at 97 K	73
Figure 3.10 :	Kinetic Behavior Comparison between MFU4.Br-1 and MFU4.Br-2 at 112 K	74
Figure 3.11 :	Kinetic Behavior Comparison between MFU4.Br-1 and MFU4.Br-2 at 127 K	75
Figure 3.12 :	A depiction of diffusion ways for large and small grain.	76
Figure 3.13 :	A visual depiction for the diffusion calculation.	78
Figure 3.14 :	Plot of $\ln(1 - (C/C_\infty))$ versus time for MFU4.Br-1 at 127 K.	79
Figure 3.15 :	Diffusion Coefficients of MFU4.Br-1 and MFU4.Br-2 at different temperatures. L and S in the figure, indicate the mean particle size as large and small, respectively.	80
Figure A.1 :	Plot of $\ln(1 - (C/C_\infty))$ versus time for MFU4.Br-1 at 77 K.	95
Figure A.2 :	Plot of $\ln(1 - (C/C_\infty))$ versus time for MFU4.Br-1 at 87 K.	96
Figure A.3 :	Plot of $\ln(1 - (C/C_\infty))$ versus time for MFU4.Br-1 at 97 K.	96
Figure A.4 :	Plot of $\ln(1 - (C/C_\infty))$ versus time for MFU4.Br-1 at 112 K.	97
Figure A.5 :	Plot of $\ln(1 - (C/C_\infty))$ versus time for MFU4.Br-1 at 127 K.	97
Figure A.6 :	Plot of $\ln(1 - (C/C_\infty))$ versus time for MFU4.Br-2 at 77 K.	98
Figure A.7 :	Plot of $\ln(1 - (C/C_\infty))$ versus time for MFU4.Br-2 at 87 K.	98
Figure A.8 :	Plot of $\ln(1 - (C/C_\infty))$ versus time for MFU4.Br-2 at 97 K.	99
Figure A.9 :	Plot of $\ln(1 - (C/C_\infty))$ versus time for MFU4.Br-2 at 112 K.	99
Figure A.10 :	Plot of $\ln(1 - (C/C_\infty))$ versus time for MFU4.Br-2 at 127 K.	100

INVESTIGATION OF GRAIN SIZE EFFECTS ON THE DIFFUSION RATE OF NANOPOROUS METAL ORGANIC FRAMEWORKS

SUMMARY

Energy need of the world is constantly increasing whereas the sources that we use for energy consumption are assumed to come an end, soon. For this reason, new energy sources has been being searched to find appropriate candidates in the usage purpose of transportation area, instead of using the conventional energy production methods.

Hydrogen is a promising energy carrier to use in mobile applications, because of its high energy content. Nevertheless, the storage of hydrogen in vehicles is still a problem to be solved. Therefore, several methods developed to overcome this issue. These methods can be grouped into two categories as physical and chemical methods.

One remarkable method in the physical methods is physisorption. In this method hydrogen is stored at the surface of host materials. Therefore, the effective force for the adsorption, mostly depends on van der Waals interactions between the surface and the hydrogen molecule. The binding strength of hydrogen molecules to surfaces of a surface is called as heat of adsorption. Heat of adsorption of a porous material increases as the pore size decreases because of overlapping mechanism of van der Waals interactions of pore walls in structure, in other words, adsorption enthalpy becomes strong in small pores.

Metal-organic Frameworks (MOFs) have been being used to store hydrogen by physisorption mechanism. MOFs are constructed by attaching metal nodes and organic linkers to each other to form porous structure. They offer ease of control over the pore size, pore shape, and electronic environment of the pores by varying the metal nodes and/or linkers. Therefore, they draw great attention of researchers within the porous material area.

One of the targets in the studies of MOFs is, the enhancement of loading and unloading times. This characteristic of MOFs is mostly related with pore sizes and apertures (if exist) in MOFs. Nevertheless, large pore sizes cause low H₂ uptake. Therefore, an optimization should be made in the design of metal-organic frameworks.

In this work, two different powders of [Zn₅Br₄(BBTA)₃] (MFU4.Br-1 and MFU4.Br-2) -that they have similar physical and chemical properties with [Zn₅Cl₄(BBTA)₃] (MFU4)-, have been studied. They are possessing different grain size distributions as homogenous and bimodal, leading average grain size as large and small. The adsorption measurements have been performed at different temperatures with Sieverts' type PCT-Pro2000 manometric device. Scanning electron microscopy has been utilized to characterize the shape and the grain size of both powders. These results have been used for calculating the diffusion coefficient and the activation energy for the diffusion. XRD measurements have been performed to gather the information about the crystal structure and the chemical composition of the powders.

In summary, it has been found that the aperture in MFU4.Br structure has strong kinetic blocking effect against H₂ diffusion in the samples that it is stronger in large grains than small grains. Additionally, this kinetic blocking effect leads where the uptake isotherms of the samples will be reversible. The small pores and/or apertures in the MFU4.Br structure are responsible for almost constant high heat of adsorption.

NANO GÖZENEKLİ METAL ORGANİK YAPILARDA TANE BOYUTUNUN DİFUZYON HIZINA ETKİSİ

ÖZET

Dünya enerji ihtiyacı gittikçe artmakta ve buna karşın enerji ihtiyacımızı karşıladığımız geleneksel enerji kaynakları doğa için zararlı olduğu bilinmekte ve üstüne üstlük geleneksel enerji kaynakları tükenmektedir. Bu sebeplerden dolayı geleneksel enerji kaynakları (fosil yakıtlar) yerine yenilenebilir enerji kaynakları araştırılmakta, araştırmanın uygulama alanlarından biri olarak ulaşım sektörünün petrol bağımlılığını alt edecek yeni yöntemler geliştirilmesi amaçlanmaktadır. Bu bağlamda, enerji yoğunluğuna göre diğer alternatiflerinden üstün olan hidrojenin, mobil araçlarda yakıt olarak kullanımı gündeme gelmiştir. Hidrojenin üstün enerji yoğunluğuna rağmen depolanması sorunu bugün onun ticari olarak ulaşım sektöründe kullanılmasında karşı karşıya olduğumuz en büyük sorundur.

Hidrojenin depolanması amacıyla, çeşitli yöntemler geliştirilmekte ve bu yöntemlerden herhangi birinin Amerika Birleşik Devletleri Enerji Departmanı (Department of Energy) tarafından, ortalama ağırlıktaki bir ulaşım aracının ihtiyaç duyacağı hidrojen miktarına (volümetrik ve gravimetrik) göre belirlenen depolama hedeflerine ulaşması amaçlanmaktadır. Hidrojen depolama, fiziksel ve kimyasal yöntem olmak üzere iki grup altında incelenmekte, kimyasal depolama, içeriğinde hidrojen bulunan hidratların sıcaklık ile ayrıştırılması sonucu hidrojenin kullanılması temeline dayanmakta ancak ayrıştırma işlemi bazı hidratlar için yüksek sıcaklıklar gerektirmekte ve hatta bu yüksek sıcaklıklar yakıt pilinin çalışma sıcaklıklarını aştığından dolayı bu yöndeki araştırmalar hidrojenin kimyasal olarak depolanmış malzemeden salınma sıcaklığını düşürecek bir yöntem bulunması yönünde devam etmektedir.

Hidrojenin fiziksel depolama yöntemlerinden biri olarak yüksek basınca dayanımlı kompozit tanklarda depolanması denenmekte, ancak bu yöntemin ulaşım aracı içerisinde yakıtın iletim hatlarındaki yüksek basınç farklılıklarından dolayı güvenlik sorunu teşkil edebileceğinden, henüz ulaşım araçlarında kullanımı yönünde bir uygulamaya gidilmemiş olup bu konudaki araştırmalar devam etmektedir. Bunun yanı sıra, kriyojenik sıcaklıklarda ve böylece düşük basınçlarda hidrojenin depolanması amaçlanmış, ancak bu yöntemde hidrojeni sıvılaştırma prosesinin büyük enerji ihtiyacı doğuracağından ve çevreden tanka doğru akan ısıнын hidrojeni gazı dönüştürmesi ve bu gazın ventilasyon ile dışarı atılması ihtiyacı olduğundan, hidrojenin bu yöntemle depolanması düşük verim oranlarına sebebiyet vermiştir.

Fiziksel yöntemlerden bir diğeri olarak adsorpsiyon ile hidrojenin malzeme yüzeylerinde depolanması son yıllarda araştırmacıların dikkatini çekmektedir. Yüksek kapasitede depolama sağlanması için öncelik geniş malzeme yüzey alanı yaratmak ve böylece hidrojen molekülünün depolanabileceği bölgeler oluşturmaktır. Bu sebeple, daha önce filtrasyon alanında kullanılan gözenekli yapılar, zeolitler, denenmiş

ancak yapılarında modifikasyon imkanı çok fazla tanımadığından yeni bir gözenekli malzeme sınıfı ihtiyacı çıkmıştır. Bunun üzerine metal-organik kafesler keşfedilmiş ve hidrojen depolanması amacı ile çeşitli yapılarda ve kimyasal bileşiklerde üretilip test edilmektedir. Metal-organik kafesler, metal bileşiklerin oluşturduğu düğüm noktaları ve bu düğüm noktalarını birbirine bağlayan organik zincirlerin çeşitli yönlerde birbirlerine bağlanmaları sonucu oluşturdukları -hidrojenin depolanması amaçlanan- gözeneklerden meydana gelmektedir. Bu gözeneklerin yüzey alanı, büyüklüğü, ve elektronik ortamı onları oluşturan metal düğüm ve organik zincirlerin değiştirilmesi ile kolayca kontrol edilebildiğinden, metal-organik kafesler ilgili araştırmacılar arasında dikkat çeken bir araştırma konusu ola gelmiştir.

Hidrojenin malzeme yüzeyinde adsorpsiyonu çoğunlukla zayıf van der Waals etkileşiminin bir sonucu olarak gerçekleşmekte ancak gözenek boyutu küçülmesiyle birlikte gözenek duvarlarının van der Waals potansiyellerinin üst üste binmesi sonucu adsorpsiyon kuvveti arttırılmaktadır. Hidrojen adsorpsiyonunun çoğunlukla zayıf etkileşimler sonucu gerçekleşmesinden dolayı, hidrojen adsorpsiyon karakteristiği ölçülecek malzemeler, düşük sıcaklıklarda test edilerek adsorpsiyon karakteri elde edilmekte buna ek olarak, oda sıcaklığında da nihai kullanım için hidrojen adsorpsiyonu ölçülmektedir. Düşük sıcaklık ölçümleri, kolay elde edilebilir olduğundan genellikle sıvı nitrojen (77 K) ve sıvı helyumun (87 K) buharlaşma sıcaklıklarında, gerçekleştirilmektedir.

Hidrojenin malzeme yüzeylerinde depolanmasındaki hedeflerden biri de, araçların dolum istasyonlarındaki sürelerini azaltmak amacı ile yüksek dolum ve boşaltım hızlarına sahip olan bir malzeme geliştirilmesidir. Bu yüzden, kafes içerisinde bulunan gözeneklerin ve eğer var ise bu gözenekleri birbirine bağlayan açıklıkların olabildiğince büyük olması gerekmektedir. Ancak, diğer taraftan büyük gözenekler hidrojen adsorpsiyon kapasitesini düşürmekte olduğundan, bu dengeyi sağlayacak optimum kafes yapısı araştırılmaktadır.

Bu çalışmada birbirleriyle değişen düzende yerleştirilmiş, sırasıyla 3.84 Å ve 11.94 Å gözenek genişliklerine ve bu gözenekleri birbirine bağlayan 2.52 Å açıklığa sahip $[Zn_5Cl_4(BBTA)_3]$ (MFU4) kafes yapısının benzeri fiziksel ve kimyasal özelliklerine sahip olan $[Zn_5Br_4(BBTA)_3]$ (MFU4.Br) malzemesinin solvothermal ve microwave irradiation yöntemleri ile üretilen, dolayısıyla farklı tane boyutuna sahip iki kopyasının hidrojen adsorpsiyon karakteristikleri ölçülmüş ve sonuçlardaki kinetik verilerden yola çıkılarak hidrojenin iki malzeme içerisindeki difüzyon hızları karşılaştırılmıştır.

Çalışma kapsamında malzemelerin hidrojen adsorpsiyon özellikleri, Sieverts' tipi PCT-Pro2000 manometrik ölçüm cihazı kullanılarak 77 K, 87 K, 97 K, 112 K, 127 K ve oda sıcaklığında test edilmiştir. Bu verilerden yola çıkılarak adsorpsiyon ısısı, difüzyon katsayısı ve difüzyon aktivasyon enerjisi hesaplanmaya çalışılmıştır. Tara- malı elektron mikroskopi yöntemi ile malzemelerin tane karakteristikleri belirlenmiş ve tane boyutu dağılımındaki farklılık dikkate alınarak difüzyon hesaplamaları yapılmıştır. X-Ray Difraksiyon analizi ile malzemelelerin kristal yapıları belirlenmiş tane boyutundaki dağılım XRD analizlerinde gözlenmiştir.

Sonuç olarak, MFU4.Br kristal yapısı içerisinde var olan dar açıklıkların hidrojen difüzyonunu kontrol ettiği ve bu dar açıklıkların hidrojen difüzyonuna etkisi ortalama tane boyutu büyük olan malzemede -ortalama tane boyutu küçük olana göre- daha

güçlü olduğu görülmüştür. Aynı zamanda, dar açıklıkların blokaj etkisi malzemelerin H₂ adsorpsiyon izotermelerinin hangi sıcaklıkta tersinir olacağı üzerine etkisi olduğu gözlemlenmiştir. Bunun dışında, malzemenin içerisindeki küçük gözeneklerin ve/veya dar açıklıkların yüksek ve neredeyse sabit adsorbsiyon ısısına sebep olduğu anlaşılmıştır.

1. INTRODUCTION

Day by day energy demand of mankind has been increasing and it turns into a difficult issue to satisfy the demands with conventional methods. In last two centuries, fossil sources (e.g. coal, and natural gas) have been used. In fact, fossil sources are quite harmful for the natural environment and they will come to an end. There is no doubt about that the global warming is a sign of a serious environmental degradation. To preclude the undesired consequences of fossil fuel consumption and to satisfy our energy demands, we must invent/find new energy sources. For this purpose, renewable energy technologies have been studied for decades, such as solar energy, wind energy, geothermal energy, bio energy, hydropower, ocean energy (ocean waves, tides, salinity), and hydrogen&fuel cells.

Hydrogen is a colorless, odorless, and tasteless gas that burns with a pale blue flame that is virtually invisible in daylight. It is the lightest of all elements; 14 times lighter than air which causes to be buoyant and rapidly disperse when released into air, which turns an important safety asset in the event of hydrogen leak from a stored media, compared to other fuel gases [1].

On the other hand, energy density of hydrogen is much greater than gasoline, moreover, hydrogen does not emit carbon dioxide when burning. On the weight basis, hydrogen has nearly three times higher energy content than gasoline. A comparison of energy contents among the rechargeable batteries and H_2 , is given in Figure 1.1 [2].

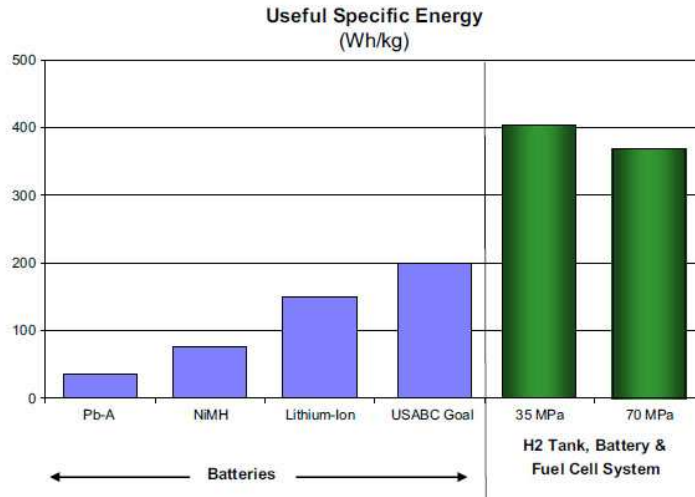


Figure 1.1: Specific Energy Comparison Between Fuel Cell Technologies and Different Battery Types [2].

Apart from its energy content supremacy, for the following reasons, hydrogen is being considered as a future energy carrier in sustainable energy society [3]:

- Hydrogen can be produced in many ways from locally available energy sources including electrolysis of water using electricity produced by wind or solar energy, or from gasification of biomass.
- The pollution levels of hydrogen combustion are relatively low and, if it is produced from sources with low emission, hydrogen is a relatively clean fuel. Mobile applications fuelled with pure hydrogen can improve local air quality by replacing petrol and diesel in cars and buses.
- As pure hydrogen can be converted by fuel cells into electricity and vice-versa with high efficiency, it has potential for storage of electrical energy (similar to the case of electricity generation from wind energy).

From political view, European Union (EU) has been investing significant amount of money by deeper research of hydrogen as fuel. For example, between the years 2002-2006, £216.3 million has been spent within the scope of Sixth European Framework Program (FP6), and the investments are being enhanced in the FP7 program [1]. Particularly, in Germany, by the collaboration of automotive industries, 20 hydrogen filling stations will be installed by 2015. Construction will take place

Stuttgart, Berlin, and Hamburg as well as along two routes that criss-cross the nation north-south and east-west [4].

From the scale of the automotive industries, by the end of 2003, at least 16 of the world's leading car manufacturers were actively developing fuel cell technology and fuel cell vehicles [5].

Although the mentioned advantages above indicate that hydrogen is a strong candidate in the area of renewable energy technologies, unfortunately there are some obstacles standing before utilization of hydrogen in vehicular systems. The main issue with the usage of hydrogen is storing hydrogen in a fuel cell [6]. The rest and less significant are, to develop efficient hydrogen delivery system, to reduce the cost of hydrogen production, and to capture carbon dioxide which is the by-product of hydrogen production from coal processes. It would seem that, hydrogen storage materials need to be studied to meet with proper usage conditions.

1.1 Hydrogen Storage

Research for hydrogen storage materials is currently remarkable topic among scientific community. Following requirements have been defined by US Department of Energy (DOE) for hydrogen fueled vehicle, According to DOE, a hydrogen fueled vehicle should overcome following requirements; greater than 300 miles of driving range with the complete system, including tank, material, valves, regulators, piping, mounting brackets, insulation, added cooling capacity, and/or other balance-of-plant components, high safety, and low cost. To satisfy these requirements, targets are specified and are announced by the reports, annually. Hydrogen storage targets for the year of 2017 are, 1.8 kWh kg^{-1} for the gravimetric evaluation ($\text{kg H}_2/\text{kg}$), and 1.3 kWh l^{-1} for the volumetric considerations [7].

Hydrocarbons have been satisfying these requirements with a 40-60 l gas tank, but unlike hydrocarbons, hydrogen exists at low densities under atmospheric conditions. For example, 1 kg hydrogen occupies 11 m^3 . A modern, commercially available car with a range of 400 km, burns about 24 kg of petrol in a combustion engine; however 4 kg of hydrogen would be needed to cover the same range with a fuel cell equipped

car [8], which yields that 45 m³ amount of volume would be needed for the storage. Clearly, to store this amount of volume within the vehicular systems is not applicable. Hence, the storage issue of hydrogen should be investigated.

1.2 Storage Methods

Storage of hydrogen is a key element for the utilization of hydrogen. Therefore, researchers have been studying for varying applicable storage technologies (Figure 1.2 [9]), to reach the requirements set by DOE.

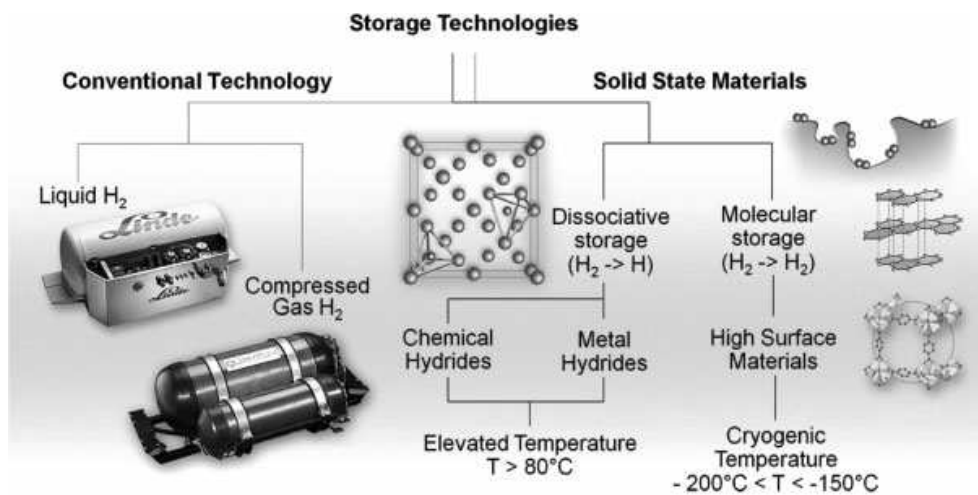


Figure 1.2: Hydrogen storage options for on-board applications [9].

Conventionally, hydrogen is stored in highly pressurized tanks made of various materials. One is made of steel that can endure to 200 bar gas pressure, whereas carbon fiber reinforced composite steel tanks have been tested up to 700 bar [10, 11]. The problem with the high pressurized tanks is that hydrogen needs to be transported through the pressurized lines in order to join conversion in the fuel cell which requires the gas pressure should be decreased by valves, down to atmospheric pressures. In that pressure adjustment process, leakage of the hydrogen can be encountered that would cause terrific consequences when the mobile tank applications are considered.

Another route can be adopted to store hydrogen that is to store it in liquid form within storage tanks at ambient pressure. In order to keep hydrogen in liquid state, temperature should be set under its critical temperature (33 K) which requires a large

amount of energy for liquefaction process. In addition to that hydrogen boils-off from the storage tank. For example, double-walled, vacuum-insulated spherical dewars, boil-off losses are typically 0.4 % per day for those with a storage volume of 50 m³, 0.2 % for 100 m³ tanks, and 0.06 % for 20 000 m³ tanks [12].

Fortunately, researchers in hydrogen storage society found another way to store hydrogen in materials (Solid State Materials Figure 1.2). Solid state storage is simply based on the sorption of hydrogen by a material that can be split into two methods by the location of the sorbed species. One of them, adsorption, that is the enrichment of an interfacial layer of the material, called physisorption, and the other one, that is absorption, it occurs when the sorbed species are incorporated with the structure of material, called chemisorption. In other words, in the adsorption, sorbed species are located on the surfaces of material, whereas in the absorption process, guest molecules take a place in the bulk of material.

1.2.1 Chemical storage

Chemisorption is defined as a process whereby hydrogen is released by a chemical reaction from material that is induced by hydrolysis or thermolysis. Due to small radii and high activity of hydrogen, it can be stored by forming strong bonds (Figure 1.3 [13]) with convincing amount of storage capacity. Although storing amount is an essential property in the hydrogen storage technologies, thermodynamic and kinetic properties have to be taken into account for the convenience of mobile applications. For example, the main problem of chemical hydrogen storage is; long refueling time which may take several hours. Additionally, releasing the chemically bonded hydrogen requires high temperatures, that may reach up to 300 °C, which is much higher than 60–100 °C, as the operating temperature of hydrogen fuel cell (PEM). Studies are focused to overcome these obstacles, by using different compounds to store hydrogen in materials, those can be grouped as hydrides [14], amin-borane adducts [15] and amide/imide systems [13].

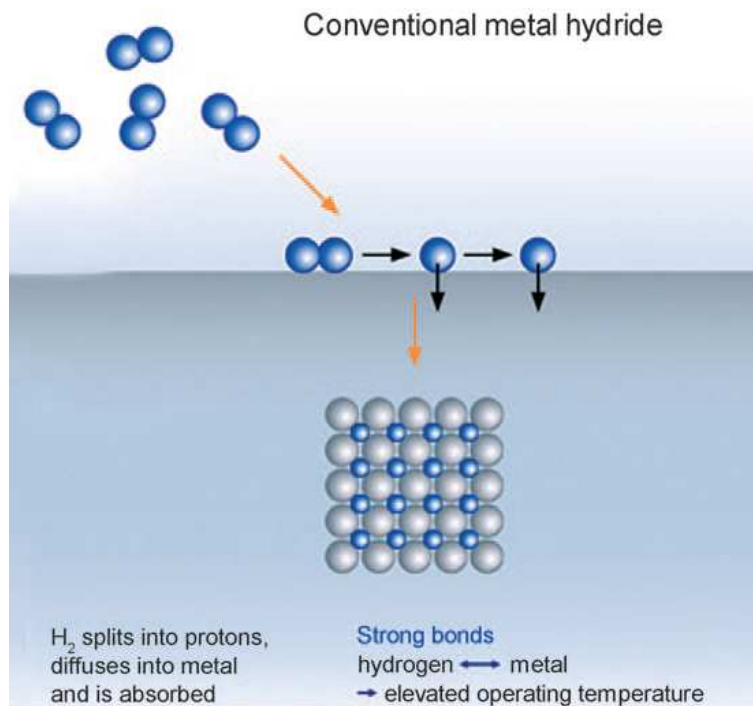


Figure 1.3: A depiction of chemisorption into a material [13].

In the hydrides group, MgH_2 shows remarkable storage capacity 7.7 wt% with low material cost, and good reversibility during cycling process, in metal hydrides group. However, its thermodynamic properties prevent MgH_2 to use for on-board applications. Hydrogen sorption equilibrium temperature of MgH_2 is around 300°C that is not viable for PEM fuel cell operation temperature. By decreasing the grain size of MgH_2 down to 0.9 nm, it is possible to obtain a desorption temperature around 200°C [16].

1.2.2 Physical storage

Physical storage based on a phenomenon called physisorption that occurs when guest molecules (in the hydrogen storage case H_2 molecules) adsorbed on the surfaces of porous materials by physical interactions (Figure 1.4 [13]). The physical interactions are composed of weak forces that are defined by *van der Waals* forces, and in some cases strong electrostatic forces when the ionic interactions is introduced to structure. Binding energy of guest molecules to surfaces of host materials is usually defined

by *heat of adsorption*, which provides useful information about applicability of the material in varying temperature conditions.

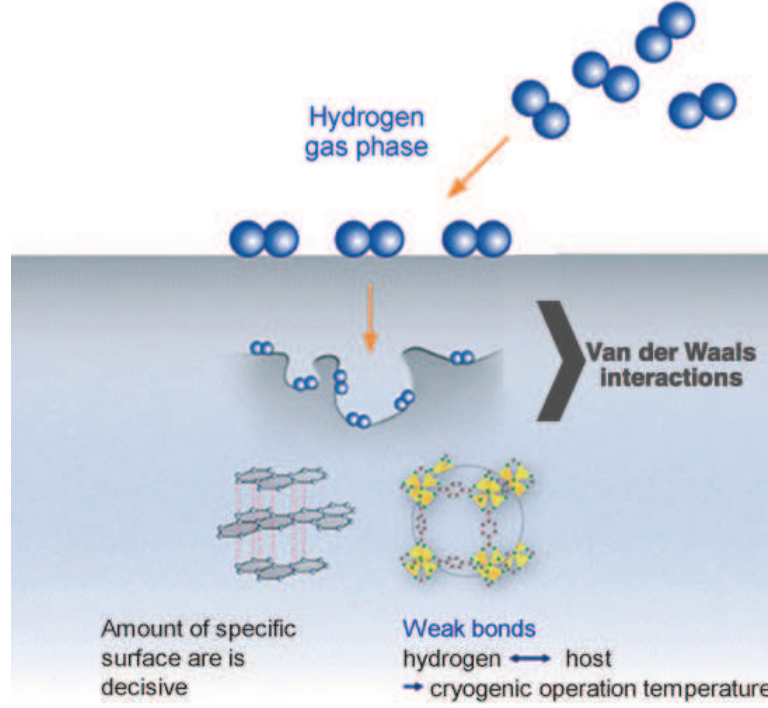


Figure 1.4: A depiction of physisorption on surfaces [13].

Van der Waals interaction is a balance of attractive and repulsive forces (Figure 1.5) which decreases with -6 and -12 power of the distances among molecules, respectively. The attractive force is even operative at long distances between gas molecules and surface atoms. At distances shorter than the sum of the radii of gas molecules and surface atoms, repulsive forces become effective to separate them with the force which is proportional to actual distance by power of -12 . Overall potential for van der Waals interaction is defined by Lennard–Jones (LJ) potential that is given in Equation (1.1):

$$V_{(r_i)} = 4\epsilon \left[\left(\frac{\sigma}{r_i} \right)^{12} - \left(\frac{\sigma}{r_i} \right)^6 \right] \quad (1.1)$$

where ϵ is the depth of the energy well, r_i the distance between a gas molecule and a generic atom i on the surface and σ the value of r_i for which the potential is zero [17]. Figure 1.5 shows the attractive and the repulsive energies change according to distance.

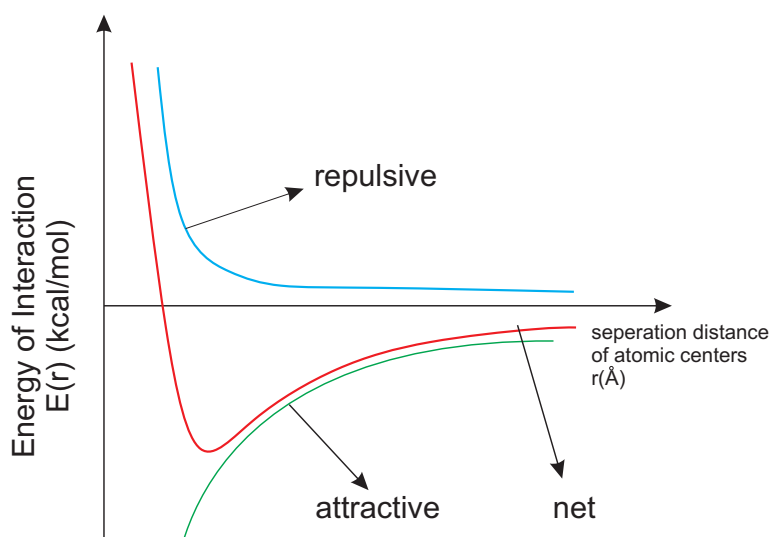


Figure 1.5: Presentation of van der Waals Forces [18].

Van der Waals forces are always ascendant in the adsorption phenomenon whereas electrostatic forces become significant when only ionic structures are involved to framework, such as in the case of zeolites and metal-organic frameworks (MOFs). However, those electrostatic forces cause guest molecules to be strongly attached to host surfaces, therefore, total binding strength (heat of adsorption) is improved. This increment in total binding energy due to electronic interactions, may arise from polarization, field-dipole, and field gradient-quadrupole interactions of the interacting molecules [18].

It should be noted that the weak interactions control the adsorbed amount in adsorption processes. To prevent an adsorbed molecule that may be easily desorbed from surface, adsorption measurements needs to be taken at low temperatures. If adsorbed guest molecules acquire a thermal energy that exceeds the binding energy, then the guest molecules overcome heat of adsorption which means that molecules are detached from their adsorbed positions.

1.2.2.1 Adsorption measurements

Adsorption measurements are usually processed as following: holding an adsorbent (a material that will adsorb guest molecules) at a constant temperature and exposing it for some time with guest molecules (adsorptive) within a well-known volume (a chamber).

After obtaining a constant adsorptive pressure in chamber, then adsorptive gas pressure is increased. This increment in the adsorptive pressure continues till sample in chamber get saturated by adsorptive molecules.

There are two methods to take adsorption measurements: one measures sorbed amount of hydrogen by detecting a difference in weight while adsorption progress that is called gravimetric method, and the other method measures adsorbed amount by detecting the change of gas pressure in the well-known volume, called volumetric method.

Gravimetric measurements are performed with highly sensitive microbalance for precise evaluation. Although the weight of sample can be precisely determined, there is one fundamental issue causes an error: H_2 molecules in pores of adsorbent, lead to buoyancy during a sorption measurement which means the microbalance measures the weight lighter than as it is. Therefore, the weight of the adsorbent is corrected by non-adsorbing gas (typically He) uptake measurements. Since adsorbent sample weight will decrease linearly as He pressure increases because of buoyancy of He gas, therefore the slope of the sample weight vs He pressure can be used for the weight correction [19].

On the other hand, volumetric method determines a change in the amount of hydrogen by monitoring the pressure in a fixed, known volume. A gas pressure decrease in the chamber refers to adsorbed amount of hydrogen whereas an increase refers to desorbed amount of hydrogen. Analogous to the gravimetric method the amount of sorbed hydrogen obtained from volumetric measurement, cannot be equated to the total amount of H_2 in an adsorbent. The hydrogen molecules that they are not adsorbed on surfaces of an adsorbent, therefore stored at the free volumes of adsorbent (cavities, spaces) cannot be detected by a measurement device, since the measurement device detects only the adsorbed H_2 molecules. Therefore, to obtain the total H_2 uptake of adsorbent material further calculations are needed.

In the volumetric evaluation, the data which is obtained from adsorption measurement refers to *excess uptake*, as it is reported commonly in publications [20, 21]. This is the difference between the amount of hydrogen that would be present in the volume of the adsorbate layer or region in the absence of adsorption and the total amount of

adsorbate in the layer. This excess value gives maximum at a point as the pressure increases and subsequent to the maximum point. It starts to decrease as the density of adsorbed layer is limited by density of liquid as it is shown in Figure 1.6 [22];

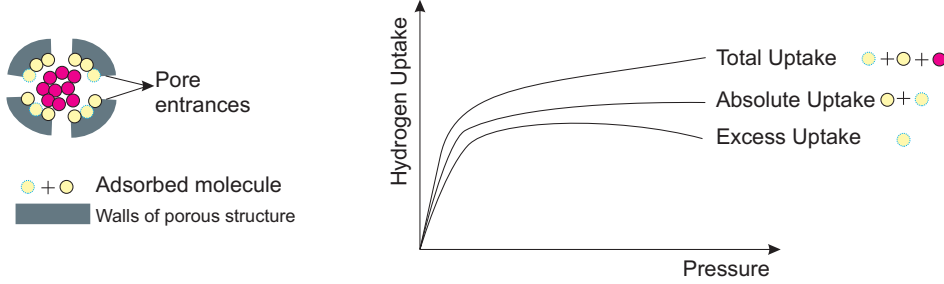


Figure 1.6: A Depiction of Excess, Absolute, Total Uptake and Pore with Adsorbed Molecules (a modified version of [22]).

Despite the decrease in the excess uptake as the applied pressure increases, adsorptive molecules start to filling up the free voids of adsorbent that amount is called total uptake. The total uptake refers to the amount of gas in the adsorbent including the amount of hydrogen that is adsorbed on the intercrystalline surfaces and voids in porous structure of adsorbent. However, absolute uptake refers to total adsorptive placed only on surfaces of adsorbent. Absolute adsorption is calculated from experimental output (excess uptake) using approximations for the average density of adsorbed gas and volume of the adsorbed layer. By assuming that density of adsorbed layer is equal to density of bulk liquid, P_{lq} , volume of excess adsorbed layer is given by Equation (1.2);

$$V_{excess} = \frac{n_{excess}}{P_{lq}} \quad (1.2)$$

The estimated amount of gas present in the volume of adsorbed layer which is the difference in the amount of adsorbed layer (absolute amount) and excess amount is given by Equation (1.3);

$$n_{absolute} - n_{excess} = \frac{P}{Z \cdot R \cdot T} \cdot V_{excess} \quad (1.3)$$

The evaluation of absolute, and total uptake from the excess uptake is shown in Equations (1.4) and (1.5);

$$n_{absolute} = n_{excess} \left(\frac{P}{Z \cdot R \cdot T \cdot P_{lq}} + 1 \right) \quad (1.4)$$

Although, up to 1 bar, typically, total uptake and excess uptake are nearly identical. Nevertheless, when the fact has been considered that higher pressures are used to store hydrogen in adsorbents, therefore calculation of total uptake becomes crucial;

$$n_{total} = n_{excess} + \left(\frac{P \cdot V_{pore}}{Z \cdot R \cdot T} \right) \quad (1.5)$$

As indicated, this equation follows the ideal gas equation to evaluate the amount of gas addition to excess amount, where P is pressure, V_{pore} is volume of the pores and Z stands for the correction factor of non-ideal gas, R universal gas constant, T is temperature.

Adsorption measurement data (excess uptake) is shown on a plot which consists of equilibrium adsorptive pressures against the corresponding hydrogen uptake in wt%, that is called uptake isotherm.

Isotherms

As introduced in the previous section, uptake isotherms are formed to help us, for the sake of interpretation of hydrogen uptake behavior of a material. However, there are many different kind of porous materials have been designed these have different physical and chemical properties. Therefore, their hydrogen uptake results, in other words, adsorption isotherms vary with their characteristics.

Uptake isotherms of porous adsorbents generate common patterns that they can be grouped into six categories. These isotherms have been classified by IUPAC in 1985 as shown in Figure 1.7 [23];

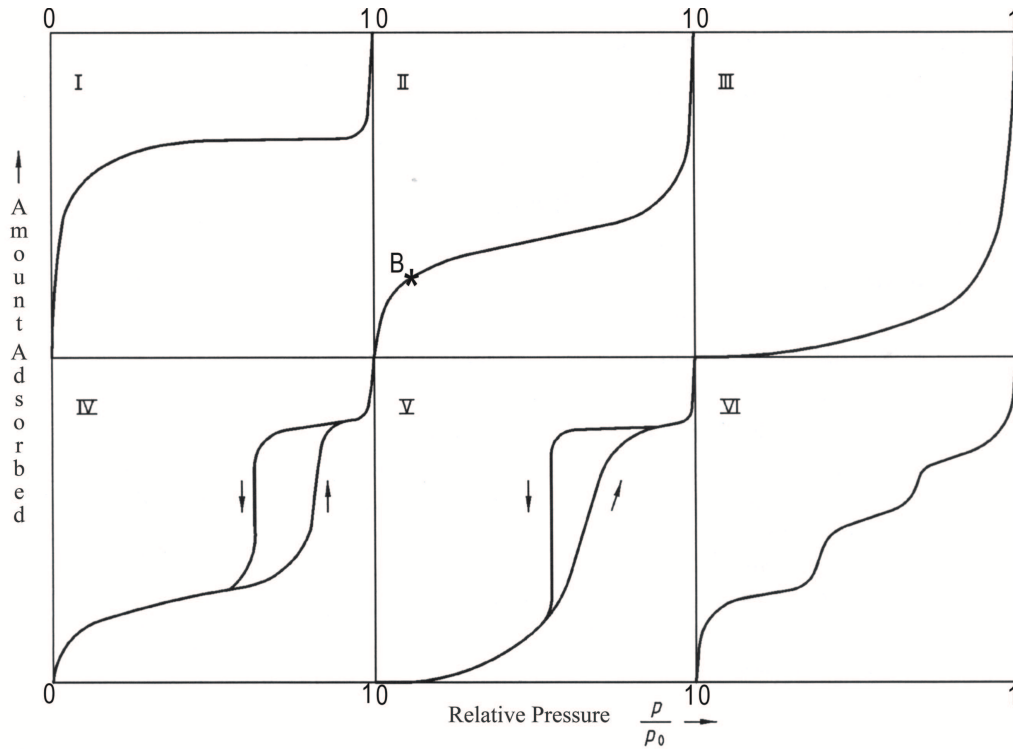


Figure 1.7: The IUPAC Classification of Adsorption Isotherms for Gas-Solid Equilibria [23].

The Type I isotherm has a sharp rise at low relative pressures, then it reaches a plateau, and at the following relative pressures it approaches a limiting value. As it indicates, a formation of an adsorbed layer at low pressures whose thickness increases progressively as the relative pressure increases. Generally microporous materials shows such isotherms.

The Type II isotherm concave to abscissa, similar to Type I. When the knee is sharp as in the Type I and Type II, it is considered, the monolayer is formed on surface of pores up to bending point, after that point multilayer formation begin. This point can be used to evaluate the amount of hydrogen that is required to cover the surface of porous material with a complete monolayer. Macroporous materials show that kind of isotherms in general. Or these isotherms represent the behavior of non-porous materials.

In type III isotherm, when the adsorbate-adsorbent interaction is relatively weak the adsorption process is not as effective as in the porous materials. This kind of host-guest interactions is not appropriate for the hydrogen storage applications.

Type IV isotherm is similar to the type II, but its desorption behavior differs from adsorption behavior which indicates, non reversible sorption process. This is because, at certain ranges of applied pressure, the amount of H₂ molecules sorbed by the host is higher on desorption than on adsorption. Thus, H₂ molecules that are adsorbed at high pressures can be stored at lower pressures beyond equilibrium density. This kind of isotherm can be related with high energy adsorption within mesoporous materials. The type V isotherm, similar to the type III, nevertheless, it shows hysteresis loop. These kinds of isotherms are rare.

The hysteresis may arise because of the capillary condensation while filling and emptying the pores whereas there are other possibilities to explain this behavior as well, such as changes in the structure of porous material during adsorption or desorption processes (gate-opening), which occurs in some *Metal-Organic Frameworks (MOFS)*, e.g. MIL-53.

In the type VI isotherm, there are two possibilities to have this behavior. One is, if the temperature is below the critical point of adsorptive then gradual adsorption can be formed within the material which brings epitaxial growth on its surfaces. The other possibility is that the varying pore size in the material, it could cause gradual adsorption.

Consequently, isotherms represent the adsorption behavior of an adsorbent as mentioned above and beyond from that isotherms gives hand to evaluate characteristic properties of adsorbent, such as heat of adsorption, and surface area of adsorbent.

1.2.2.2 Surface area

Calculation of a surface area among ideal shapes such as cubes, spheres is relatively easy. Since surface of porous materials do not provide ideal shapes, therefore another approach to calculation of surface area should be adopted.

Possessing fine pore structure in porous material cause an increase in the strength of van der Waals interactions, also helps to create large inner surface area. To be able to get a successful surface area determination, adsorption isotherm should be fit onto the one of theoretical isotherm models. From the theoretical models, the required number of adsorbate molecules to cover one layer of surface can be predicted. After obtaining

the number of the adsorbate molecules, one gets the surface area of porous material by multiplication with the area of the adsorbate molecules.

Henry model

For adsorption on a surface at low concentrations (low loading pressures), such that all adsorbed molecules isolated from each other, amount of adsorbed molecules correlate linearly with loading pressure. This phenomenon is described by Henry's Law, as Equation (1.6) states;

$$n_{ads} = k_H \cdot P \quad (1.6)$$

where k_H is the Henry constant in equation, P is pressure and n_{ads} is adsorbed amount in this region. Although Henry's Law is well documented and it is explanatory, some isotherms deviate from linearity even at low concentrations. In fact this kind of relationship is not surprising for adsorbent materials. The reason for that might be pores are not open at that low temperatures, therefore uptake becomes possible as loading pressure increases.

Langmuir isotherm model

Langmuir isotherm can be assumed as a basic introduction to calculation of surface area of microporous materials, which is used for the materials those have behavior of type I isotherm. In order to get appropriate evaluation of surface area, Langmuir isotherm has some assumptions as following [24];

- The adsorbate is immobile
- All the adsorption sites are equivalent (Homogeneous)
- Every possible site can hold only one molecule (No stacking)
- There are no interactions among the adsorbed molecules

$$\begin{aligned} N_{ads} &= N_{des} \\ N_m \theta_1 v_1 e^{-E/RT} &= k P \theta_0 A_1 \end{aligned} \quad (1.7)$$

where N_m is the number of adsorbate molecules in a completed monolayer of unit area, ν_1 is the vibrational frequency of the adsorbate, E is the energy of adsorption, A_1 is the probability of a molecule is being adsorbed and, the θ_1 and θ_0 are the fraction of a completed monolayer and the fully empty layer, respectively. Remembering the $\theta_0 = 1 - \theta_1$ Equation (1.7) yields:

$$\theta_1 = \frac{kPA_1}{N_m\nu_1 e^{-E/RT}} \quad (1.8)$$

$$K = \frac{kA_1}{N_m\nu_1 e^{-E/RT}} \quad (1.9)$$

by bringing θ_1 in Equation (1.8) and K in Equation (1.9) to one equation it yields to Equation (1.10);

$$\theta_1 = \frac{KP}{1 + KP} \quad (1.10)$$

Up to and including one layer of coverage, θ_1 can be expressed as;

$$\theta_1 = \frac{N}{N_m} = \frac{W}{W_m} \quad (1.11)$$

where N and N_m are the number of molecules in the incomplete and complete monolayer respectively, and W/W_m is the weight adsorbed in a completed monolayer. Rearrangement of Equation (1.11) gives;

$$\frac{P}{W} = \frac{1}{KW_m} + \frac{P}{W_m} \quad (1.12)$$

a plot of P/W versus P in Equation (1.12) would give a straight line with a slope $1/W_m$, then W_m can be calculated. And the surface area of the adsorbent becomes;

$$S = \frac{W_m N A_x}{M} \quad (1.13)$$

where A_x and M are the cross-sectional area and the molecular weight of the adsorbate, respectively, and N is the Avogadro's number in Equation (1.13).

For most adsorption cases adsorbed molecules are located preferentially (heterogeneity). Upon the lacks of Langmuir theory, in 1938, Stephen Brunauer, Paul Hugh Emmett, and Edward Teller published their article [25] by considering the multilayer adsorption issue. Nevertheless, Langmuir isotherm is widely used in the case that only one adsorbate layer (monolayer) is bound to host surface e.g. chemisorption.

BET isotherm model

In reality, most of porous materials possess energetically heterogeneous surface, since the narrower pores would have the most energetic sites on their surfaces -because of the overlapping of van der Waals forces [22]. Even though, adsorption surface is flat (non-porous material), energy distribution of adsorption surface may vary as the presence of different functional groups on the surface.

As mentioned before, during adsorption process, first, energetically higher sites are occupied rather than the less ones. When the high energetically sites are fully covered, guest molecules sit on the lower energetic sites as guest molecule pressure increases or they may prefer to sit on the molecules those exist on energetic sites. So, first layer of adsorption can act as possible adsorption sites for molecules those will form second layer. Therefore, completely covered monolayer formation is not possible by any pressure. BET theory tries to calculate the surface area, from the number of molecules would have required to form monolayer, by considering the number of molecules that actually formed as multilayer, during adsorption.

Derivation of BET isotherm starts with equalization of adsorption rate to desorption rate at equilibrium that is given by Equation (1.14):

$$a_1 P \theta_0 = b_1 \theta_1 \exp - \frac{E_1}{RT} \quad (1.14)$$

where a_1 and b_1 adsorption and desorption constants for the first layer and E_1 is the energy for the adsorption on the first layer. It should be noted that, according to BET theory second and all the following layers will have same energy, E_L , which is liquefaction energy. And keeping in mind that, sum of the all fractional coverage

will be equal to $1 \sum_{i=1}^{\infty} \theta_i = 1$ and the adsorbed total amount on the layers will be the sum of the individual adsorbed quantities on the all layers $n = n_m \sum_{i=1}^{\infty} i \theta_i$. Then the equation(1.14), can be written as;

$$\frac{P}{n(1-P)} = \frac{1}{n_m C} + \frac{C-1}{n_m C} P \quad (1.15)$$

where C is an constant in Equation (1.15) which is approximately $C \approx \exp\left(\frac{E_1-E_L}{RT}\right)$.

A plot $\frac{P}{n(1-P)}$ against P will yield a straight line usually in the range $0.05 \leq P \leq 0.35$ with a slope $\frac{C-1}{n_m C}$ and intercept $\frac{1}{n_m C}$ by solving preceding equations for n_m the weight adsorbed in a *monolayer* yields to Equation (1.16);

$$n_m = \frac{1}{s+i} \quad (1.16)$$

then the total surface area can be calculated by using Equation (1.17);

$$S = \frac{n_m N A_x}{M} \quad (1.17)$$

A_x cross-sectional area of adsorbate, M is the molecular weight of adsorbate , and N is Avagadro' s number. For further explanations and greater determinations of heat of adsorption in detail, Lowell [26], is very good source for the interested readers.

Researchers supported the applicability of BET isotherms, by comparing two isotherms; one is obtained experimentally and the other one is predicted by using Monte Carlo simulation techniques, and results were satisfying enough [27].

Since guest molecules adsorb on surface, it is clear that high surface area is crucial for adsorption materials, and calculation of surface area allows us to have a sense of uptake results. Even though this is true, when adsorbents are having same surface area their uptake might be different from each other. It is because, the binding strength of guest molecules, in other words heat of adsorption varies with the physical structure of porous materials.

1.2.2.3 Isosteric heat of adsorption

Isosteric heat of adsorption is a result of interactions including van der Waals, ionic e.g. forces, therefore a magnitude of overall binding energy between adsorbed molecules and host molecules. On a flat surface, adsorbed molecules feel the van der Waals interaction of one or two atoms at the surface of the adsorbent. For surfaces exhibiting curvature, e.g. in spherical pores, the van der Waals potentials of these surface atoms overlap and strengthen the adsorption potential of the material. In addition, when the pore diameter and adsorptive diameter of adsorbed molecule becomes closer to each other, the overlapping of van der Waals potential increases. As a consequence of that, the binding energy of the guest molecules in the smaller pores is stronger than that of larger ones.

Since the translational freedom of adsorbed molecule on a surface is less than the molecules that are free in space (not able to move in 3D when they adsorbed), freedom of a molecule decreases when it is adsorbed on a surface. Considering that entropy is a measure of number of specific ways which a system may be arranged, entropy change at the end of adsorption process will be negative, ($\Delta S = S_{ads} - S_{gas}$). Thermodynamically, a process to be happen Gibb's Free Energy change should be negative as well. Therefore;

$$\Delta G = \Delta H - T\Delta S \quad (1.18)$$

according to Equation (1.18), ΔH , enthalpy change in the process will be negative, in other words, adsorption is an exothermic process.

To calculate the heat of adsorption, adsorption isotherms are fit to one of the following equations, (the virial-type equation, the following virial-type equation and, Langmuir-Freundlich equation), heat of adsorption is used [20].

In this study, adsorption data obtained at constant T and constant V for each measurement. Helmholtz-Free energy that is given by Equation (1.19), was fit to experimental data to calculate the heat of adsorption.

$$\Delta H_{ads} = R \cdot \left(\frac{\partial \ln P}{\partial \frac{1}{T}} \right)_{\theta} \quad (1.19)$$

R is the gas constant, T is temperature and, P is equilibrium pressure. A plot, which is drawn P against to T will converge to a linear correlation with the slope, ΔH_{ads} .

1.3 Fundamentals of Diffusion

Diffusion is a process that validates tendency of the matter to migrate in such a way to eliminate spatial variations in composition, by causing increase in entropy of the system to reach maximum randomness above the temperature absolute zero. In an alternative expression, diffusion is a spontaneous tendency of all systems to equalize concentration in space that can be depicted as it in Figure 1.8;

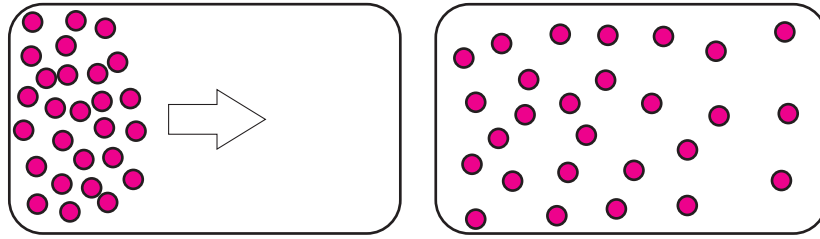


Figure 1.8: Diffusion of particles, they spread over the volume to eliminate concentration gradient.

Diffusion in gasses occurs in the scale of seconds, minutes in liquids, and it takes years or millennia to occur within solids. Therefore, the calculation of the rate which diffusion occurs turns out a significant issue. In 1855, Adolf Fick, who wants to mathematically contribute to the Graham's observations related to diffusion phenomenon, by adopting Fourier's law of heat conduction, stated an equation for diffusivity which is known generally Fick's first law of diffusion;

$$J = -D \frac{\partial C}{\partial x} \quad (1.20)$$

as it shown in Equation (1.20), where J is the flux per unit area of section, C the concentration of diffusing substance, x the space coordinate measured normal to the section, and D is called the diffusion coefficient.

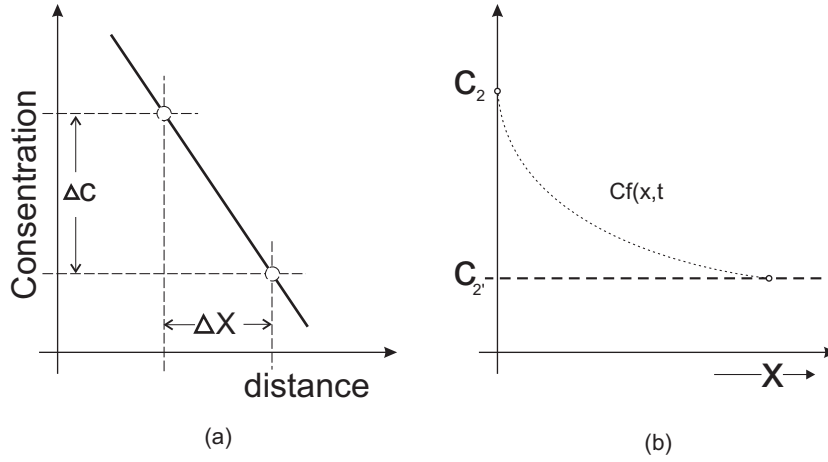


Figure 1.9: A depiction of Fick's First and Second Law [28]

Fick's first law proposes the diffusion is the net flux of particles down a concentration gradient by the random movement of included particles, and the flux is directly proportional to the steepness of the gradient (Figure 1.9a, [28]). In the sense of first law, as it is assumed that the diffusion occurs in steady state conditions. To develop the first law in an unconfined volume, within the sense of the law of mass conservation (Equation (1.21)), Fick developed the second law of diffusion that is given by Equation (1.22);

$$\frac{\partial C}{\partial t} = -\frac{\partial J}{\partial x} \quad (1.21)$$

$$\frac{\partial C}{\partial t} = -D \frac{\partial^2 C}{\partial x^2} \quad (1.22)$$

Fick's second law of diffusion involves time t , it asserts that concentration change within unit time, is proportional to the change in flux at corresponding length. As it is seen from the Equation (1.22), diffusivity makes no such assumption in the case that diffusivity varies with concentration, therefore the solution of the equation can be achieved by applying appropriate initial and boundary conditions [29]. However, in some cases (e.g. diffusion in microporous materials) diffusivity can be affected by concentration gradient, in such cases D becomes non-linear and takes the form of $D(c)$. In the case of that the diffusivity becomes concentration dependent, solution of

the Fick's second law cannot be obtained by analytical approaches, therefore it should be solved by numerical methods [30,31].

The calculation of diffusivity explained above, adopts macroscopic approach that it considers total mass change (transport diffusivity) in a system. There is also another approach being used that by following individual marked atoms/molecules those involved the diffusion process, therefore performing calculations for whole system, called tracer or self-diffusivity.

1.3.1 Random walk, self- and transport diffusion

A random walk is defined as a mathematical formalization of a path that consists of successive random steps. Atoms or molecules do this random motion under the thermal impacts and the total displacement of the individuals is interpreted in the means of diffusion. With a given number of jumps per second and mean jump distances of any particle, after some very large number of jumps, the displacement of the particles from an arbitrary starting point can be calculated. Because of the random nature of the diffusion process and the large number of jumps, it can be turn relatively easy to calculate the average distance that a group of atoms will have migrated from their initial sites. So the mean square displacement after n steps of a random walk, is calculated by [32];

$$\langle z^2(n) \rangle = \left\langle \left(\sum_{i=1}^n l_i \right)^2 \right\rangle \quad (1.23)$$

$$\langle z^2(n) \rangle = nl^2$$

l is the mean jump distance and z is the mean displacement of the particles. Such a movement, a correspondence to the movement of a man that he moves on a straight line and giving his decisions according to the results of a tossing coin, with equal probabilities to move($\pm 1/2$) forward or backwards. When the number of steps is

related with the time by $n = t/\tau$ which τ , is the time between jumps; Equation (1.23), yields to the Equation (1.24) with $\mathcal{D} = l^2/2\tau$;

$$\langle z^2(n) \rangle = 2\mathcal{D}t$$

Or in 3-dimension; (1.24)

$$\langle z^2(n) \rangle = 6\mathcal{D}t$$

The relationship between random walk and diffusing molecules in an environment was first elucidated by Einstein [33]. To approach the Fick's equation in the means of random walk, the particles (atoms or molecules) must be regarded as they are labeled. The concentration distribution of these labeled particles will be the same as stated in the Equation (1.22), and a solution of Fick's second law (1.22) is obtained with appropriate initial and boundary conditions that is given by Equation (1.25);

$$C = \frac{A}{\sqrt{t}} e^{-z^2/4Dt} \quad (1.25)$$

and therefore the amount of substance diffusing in a parallel-sided container of unit cross-sectional area and infinite length in the z direction given by Equation (1.26);

$$M = \int_{-\infty}^{+\infty} C dz \quad (1.26)$$

and by writing $\xi^2 = z^2/4Dt$ into Equation (1.26) it yields to Equation (1.27);

$$M = 2A\sqrt{D} \int_{-\infty}^{+\infty} e^{-\xi^2} d\xi = 2A\sqrt{\pi D} \quad (1.27)$$

and the distribution of the solute at all later time will be given by;

$$\frac{c}{M} = \frac{e^{-z^2/4Dt}}{\sqrt{4\pi Dt}} \quad (1.28)$$

Equation (1.28), gives the probability of a particle finding at position z , that was located at the origin at time zero. And it can be completely defined by the mean square displacement of the diffusing particles, by integration Equation (1.28);

$$\langle z^2(t) \rangle = \int_{-\infty}^{+\infty} z^2 \frac{e^{-z^2/4Dt}}{\sqrt{4\pi Dt}} dz = 2Dt \quad (1.29)$$

$$\langle r^2(t) \rangle = \int \frac{e^{-r^2/4Dt}}{4\pi Dt^{3/2}} = 6Dt$$

first line in the equation states the diffusivity in one direction and the latter one states the diffusion which considered in 3-dimension. It can be seen that Equation (1.24) exactly the same with the Equation (1.29) above. These equations are known as Einstein's relations and provide us to approach to diffusion phenomenon by considering individual atom movements by the means of random walk.

Transport diffusion, is a definition of massively moving particles in an environment, resulting from a concentration gradient which lies between the moving particles and the corresponding surrounding. In fact, it means the net particle transport. Figure 1.10 depicts the difference between self and transport diffusion.

Self-diffusion, can be measured by either tagging a certain fraction of the diffusing particles or by following the trajectories of the particles resulting with mean square displacement, and therefore using the Equation (1.24) self-diffusion coefficient(\mathcal{D}) can be calculated. In addition to that some studies provide a calculation of the transport diffusivity from self-diffusivity by using MD and GCMC simulation techniques [34].

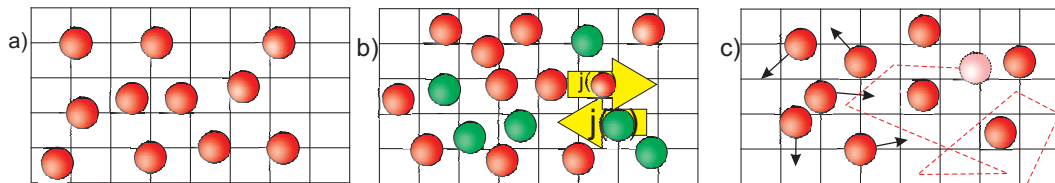


Figure 1.10: Schematic representations for the measurement of (a) transport diffusion and of self-diffusion by (b) following the (counter-) flux of differently labeled molecules (red, green) or by (c) recording the displacement of the individual molecules [36].

In Figure 1.10a, a bunch of particles, moving to the right, in order to increase the randomness of the environment, by following the laws of Fick. In Figure 1.10b, some of the particles are shown as labeled, whereas, in Figure 1.10c the tracking process of the labeled particles is depicted. By tracking the individual labeled particles, a diffusion coefficient is calculated from random walk equations, which is self-diffusivity coefficient. The transport diffusivity and self-diffusivity can be equated with an assumption when each individual particle diffuses independently of each other, such situation may occur in the range of low concentrations of guest molecules, where the rates of transport and self-diffusion are identical.

The explanations above consist of fundamental basics of diffusion. For diffusion in microporous environment, further developments and limitations should be specified to obtain satisfying answers.

1.3.2 Diffusion in porous media

Most of the industrial porous materials are available in pellet form, accordingly microporous crystals are obtained in assembled condition (Figure 1.11). Diffusion of guest particles through microporous materials splits into two ways as micropore and macropore diffusion.

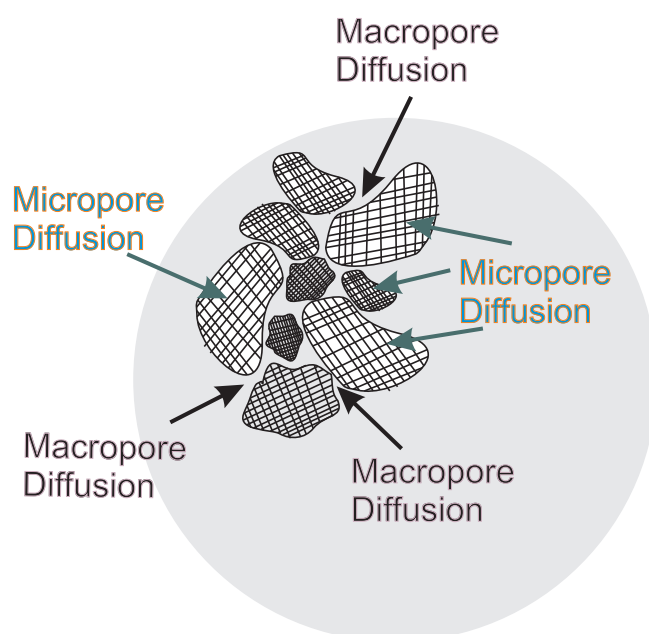


Figure 1.11: Micropore and Macropore Diffusion [36].

In the micropore size, the overlapping surface forces of opposed pore walls are predominant. In the mesopore range, surface forces and capillary forces turn out to be significant, while for the macropores, the contribution of the pore walls is very small.

In the case of **Micropore diffusion** (or intracrystalline diffusion) diffusing guest molecule never escapes from the force field of the adsorbent surface therefore mass transport occurs by an activated process involving jumps between adsorption “sites”. The rate of diffusion between the pellets is too fast, therefore the uptake of guest molecules is controlled in micropores. This is expected in small-pores in which the free aperture of the window is only slightly greater than the critical diameter of the guest molecule, the activation energy correlates directly with critical molecular diameter suggesting that the rate-limiting step is the passage of the molecule through the sieve window.

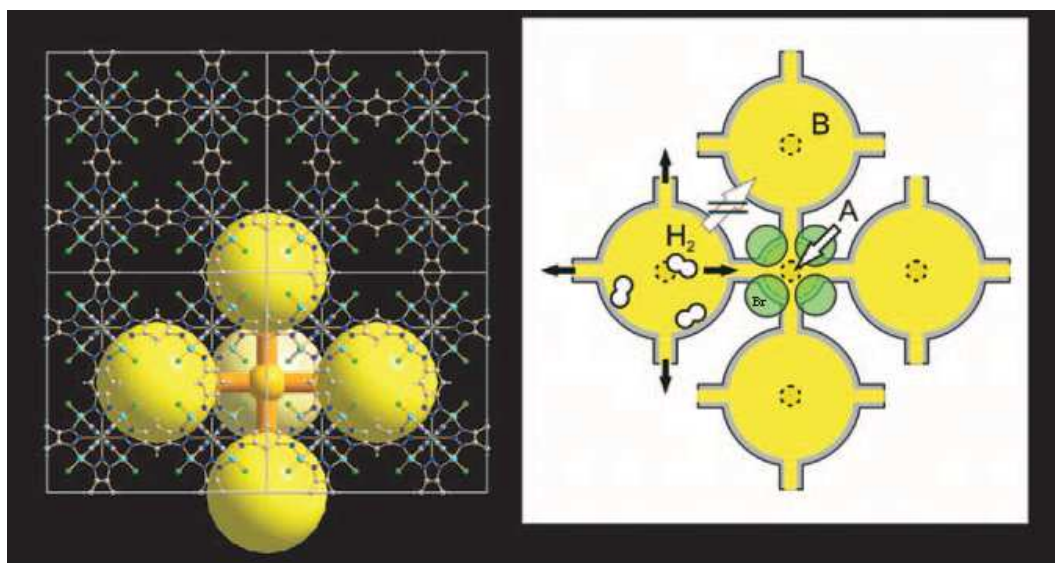


Figure 1.12: Intracrystalline diffusion paths in MFU4.Br structure [35].

In Figure 1.12 (modified version of [35]), the structure of MFU4.Br version (left) and possible diffusion paths in the structure is shown (right). Diffusing H_2 molecules along the MFU4.Br structure should pass the small and large cavities (shown as yellow and dark yellow spheres, 3.88 \AA and 11.94 \AA , respectively) and the aperture connects those cavities to each other for passage (2.52 \AA). Therefore, in this case the aperture controls the kinetic of guest uptake in the adsorption process.

On the other hand, in **Macropore Diffusion**, diffusion occurs in large pores such that the diffusing molecule escapes from the surface field. This is expected for large particles and guest molecules which have sizes much smaller than the pore size. For macropore diffusion, there are four mechanism is defined [36], they describe possible types of progress of guest molecules in the macropore media.

1.3.3 Macropore diffusion mechanisms

Diffusion mechanisms vary with the size of the diffusing particles, therefore, their interactions within the media that they are progressing. For a porous media, a diffusion mechanism depends on the pore diameter of host material compared to the diameter of the guest molecules. As the pore size decreases, the occurring rate of Knudsen diffusivity increases whereas in the large pores diffusion mechanism consist of viscous flow or molecular diffusion.

In an adsorbent porous media, there are many effects influence the diffusivity of the guest particles. The effects can be: pore geometry, pore surface roughness, pore width. For a diffusive process in a porous media, the mechanism that will be effective, mainly depends on the pore diameter of porous material. This relationship can also be seen from the Figure 1.13 [37];

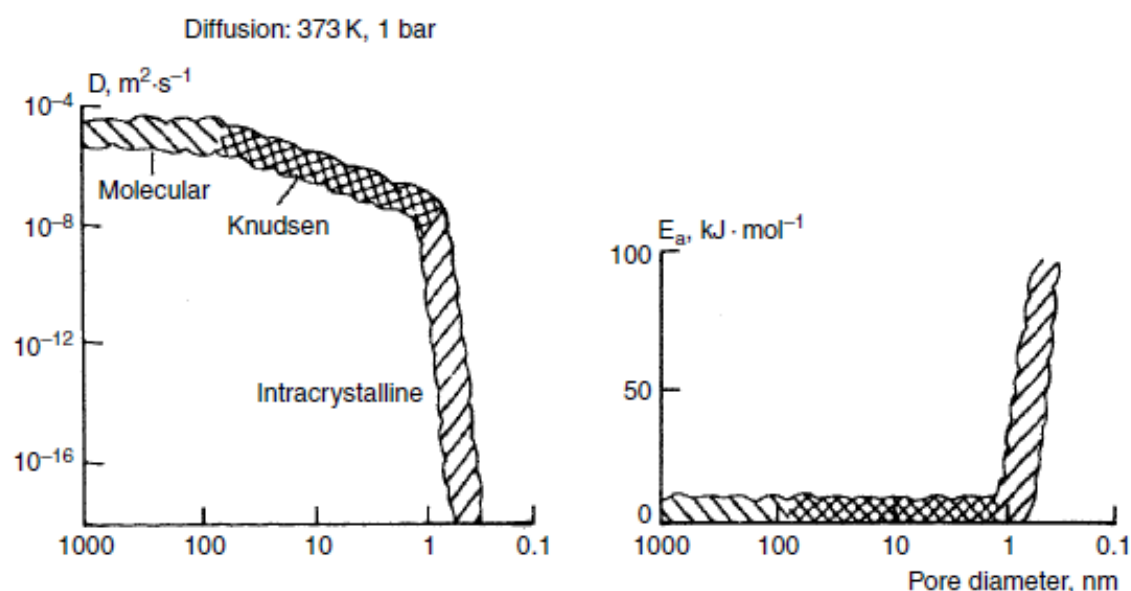


Figure 1.13: Effective diffusion mechanism and corresponding activation energy according to the pore size [37].

Figure 1.13, shows that the effect of pore size on the diffusion mechanism. Accordingly, in a porous material that is having pore size smaller than 1 nm, intracrystalline diffusion will be effective, whereas if pore size larger than 100 nm molecular diffusion will dominate.

To describe the diffusion mechanisms, pore structures have to be simplified, afterwards required constants are added. The mechanisms that they are explained below, start with such simplified models and come to the end with complex structures.

1.3.3.1 Knudsen mechanism

Knudsen mechanism refers to a gas transport regime where the mean free path (λ) between particle-particle collisions is significantly larger than at least one of spatial dimensions of the considered system [38]. Therefore, it becomes effective to overall diffusion, when the pore size is relatively small to the size of guest particles (atoms/molecules). It should be taken into account that Knudsen diffusion occurs with high probabilities at low pressures, since at the low pressures particles collide with wall molecules rather than colliding with each other [39].

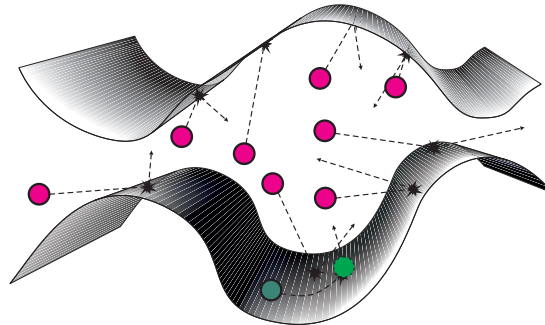


Figure 1.14: Knudsen Diffusion Mechanism: Magenta balls represent the diffusing particles in a pore whereas the green ball refers to particle that is diffusing on the surface [39].

As it is seen in Figure 1.14, when a particle hits the pore wall, it exchanges the energy with the pore atoms or molecules with the result the direction and the velocity of the reflected particle is totally random. In this condition, diffusivity is calculated according to;

$$\mathcal{D}_K = r \left(\frac{32 kT}{9\pi m} \right)^{1/2} \quad (1.30)$$

where r is the pore diameter, k is the Boltzmann coefficient m is the molecular mass of guest particles, in Equation (1.30).

Since the Knudsen mechanism does not depend on the intermolecular collisions, therefore, it deviates with temperature and particle mass, and independent from the pressure (in the range of low pressures).

1.3.3.2 Viscous flow

Viscous flow is occurred, when there is a difference in pressure between the ends of the medium, this pressure difference causes a flow through the medium. For the simplicity we can deal with a capillary Figure 1.15;

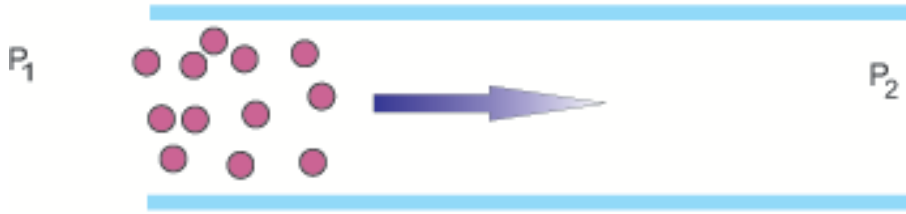


Figure 1.15: A depiction of Viscous Flow [40].

As it is seen in Figure 1.15, there are two different pressures at the ends of capillary ($P_1 \neq P_2$). The laminar flow is assumed to occur resulting from pressure gradient, that is with no slip on the pore wall due to the viscosity of the fluid. Therefore, the viscous flow is defined by Poiseuille's law that is given by Equation (1.31) [40];

$$J_{vis} = \frac{B_0}{\mu} \frac{\bar{P}}{RT} \frac{(P_1 - P_2)}{L} \quad (1.31)$$

where P is pressure, B_0 is flow parameter that is $(r^2/8)$, \bar{P} , is mean pressure and R is universal gas constant. Equation (1.31) valid for such a capillary that is depicted in Figure 1.15. For porous medium, a difference should be inserted to the Equation (1.31), which arises with the definition of the coefficient of B_0 [30].

It should be noted here, a plot of permeability ($J_{vis}/(\delta P/L)$) versus the mean pressure a helpful feature to see which mechanism is effective in the capillary. This plot would give a horizontal line in the conditions of Knudsen mechanism, and a straight line come out if the viscous flow is effective. At the pressures, falling down between these two mechanisms there would be transition region which the effectiveness of those two mechanisms would vary with the changing pressure [30].

1.3.3.3 Molecular diffusion

This type of diffusion mechanism, results from the collision among different type of particles (mixture). As a result of the collisions, there will be a net moment exchange between two particles. Although the significance of this mechanism depends on the ratio of pore diameter and particle diameter, when the large pore is introduced the effect of wall-particle diffusion can be neglected beside the molecular diffusion [41].

1.3.3.4 Surface diffusion

Until here, possible interactions between diffusing particles and the porous host material such as chemical, electrochemical, adsorptive interactions have not been considered. Hence, the equations and models have been given so far, cover the issue that porous medium and the diffusing particles inert to each other. However, since the adsorption phenomenon predominantly depends on such interactions, therefore, the mentioned interactions (Section 1.2), are crucial for the adsorbents. The interactions between the surface and guest molecules are more important for MOFs, since MOFs have high surface area. Considering that, the interactions occur on the surfaces of porous host materials, therefore, they are involved into the surface diffusion mechanism.

Surface diffusion, is a mechanism of moving particles those are adsorbed on the surfaces. Similarly to interstitial diffusion, surface diffusion is an activated process, but its activation energy is less than the activation of interstitial diffusion.

In the adsorption process, particles are able to migrate over the surface of the pore wall, if the binding energy of the particles to the surface wall, is not too great. On the other hand this migrating particles, may collide with the surface molecules, and

they even might be emitted from the surface molecules, if the momentum transfer that arises from the collision of surface molecules with the adsorbed particles, high enough to overcome binding strength to the surface molecule of the adsorbed particle. Moreover, the molecules those constructed the pore surfaces may vary through the pore surface, then the directions of the emitted particles would be independent of the original direction of the incident, as well as from each adsorbed green particle seen in Figure 1.14.

Diffusion on the surface, occurs by hopping mechanism. And its diffusivity given by Equation (1.32);

$$D_s = \frac{1}{4} v_T \delta \exp\left(-\frac{E_s}{RT}\right) = D_{s0} \exp\left(-\frac{E_s}{RT}\right) \quad (1.32)$$

where δ is the distance between jumps, v_T is the thermal velocity of the adsorbed particle, and E_s is the activation energy for the particle jumps.

Besides that, adsorbed amount decreases with increasing temperature, because of the binding energy between the surface molecules and the adsorbed particles is overwhelmed by increased thermal energy of the particles. Since there wouldn't be adsorbed particles to migrate on the surfaces at relatively high temperatures, therefore surface diffusivity can decrease with increasing temperature. So, we can say that there is temperature range to assume whether surface diffusivity will decrease or not. This is true for the linear isotherm systems. On the contrary to that, in the nonlinear isotherm systems, when the surface is highly covered an increase in the temperature cause an increase in the surface diffusivity and little amount of decrease in the adsorbed amount [30].

1.3.4 Measurement techniques

There are several types of methods to measure diffusion in porous materials that they are given in Figure 1.16 [37]. One can use, NMR spectroscopy, by tracking the particles in the porous media, therefore self-diffusion of the guest particle can be calculated [36], or flow methods are used to determine overall diffusivity [42]. There is another method can be used from the view of sorption measurements, that

is, by utilizing the kinetic outputs of sorption measurements, the diffusion of the guest particles which those are adsorbed from the porous materials.

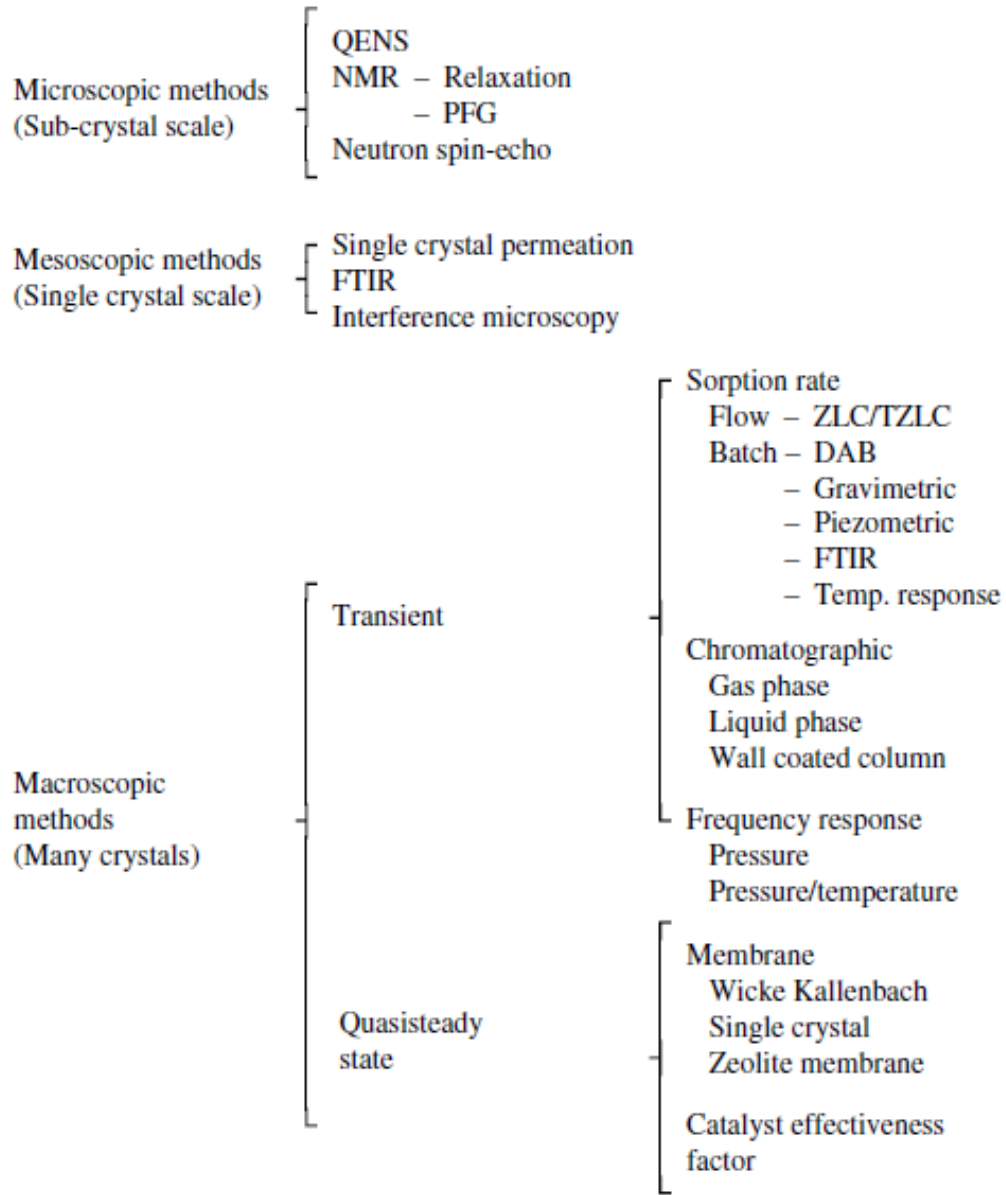


Figure 1.16: Experimental diffusion measurement techniques for porous media [37].

The main microscopic methods are quasi-elastic neutron scattering (QENS) and nuclear magnetic resonance (NMR) based techniques.

On the other hand, direct measurement of the adsorption or desorption rate is possible by macroscopic methods. For a small sample of adsorbent subjected to a well-defined change in ambient concentration (or partial pressure) of sorbate is perhaps the most

obvious way to attempt to measure intracrystalline diffusion. Gravimetric, volumetric and piezometric methods have all been used to follow that sorption process.

1.3.4.1 Sorption kinetics

Sorption kinetics is the most widely used method, to evaluate intra-(micro) or interparticle (macro) diffusivities involves measuring the sorption rate when a sample of adsorbent is subjected to a well-defined change in the pressure or concentration at fixed temperature. After obtaining the sorption data, isotherms (section) are plotted, therefore according to isotherm behavior (shape) its model is fit to theoretical models.

If isotherm of an adsorption measurement is linear (Henry Isotherm), the uptake rate is given by the solution of transient equation. For a spherical particle, diffusion equation may be written as follows [42];

$$\frac{\partial q}{\partial t} = \frac{1}{r^2} \frac{\partial}{\partial r} \left(r^2 D_c \frac{\partial q}{\partial r} \right) \quad (1.33)$$

if the uptake occurs over a small change in the adsorbed phase concentration, a constant diffusivity may be assumed. For a step change in concentration at time zero the relevant initial and boundary condition can be written;

$$\begin{aligned} t < 0, & \quad C = C_0, \quad q = q_0(\text{independent of } r \text{ and } t) \\ t \geq 0, & \quad C = C_\infty, \quad q(r_c, t) \rightarrow q_\infty \\ t \rightarrow \infty & \quad C = C_\infty, \quad q(r, t) \rightarrow q_\infty \\ \frac{\partial q}{\partial r} \Big|_{r=0} = 0 & \quad \text{for all } t \end{aligned} \quad (1.34)$$

and then analytical solution is obtained by using the initial and boundary conditions that are given in Equation (1.34). Therefore, Equation (1.33) yields to;

$$\frac{m_t}{m_\infty} = 1 - \frac{6}{\pi^2} \exp \left[-\frac{\pi^2 D_c t}{r_c^2} \right] \quad (1.35)$$

according to Equation (1.35), a plot of $\ln(1 - m_t/m_\infty)$ versus t will give a straight line with slope $-\pi^2 D_c / r_c^2$ and intercept $\ln(6/\pi^2)$ at $t = 0$.

If the sorption isotherm gives a nonlinear curve (e.g. Langmuir type) therefore another approach should be adopted. For nonlinear isotherms, micropore diffusivity becomes concentration dependent. Therefore diffusivity equation can be written as follows;

$$\frac{\partial q}{\partial t} = \frac{D_c}{r^2} \frac{\partial}{\partial r} \left(\frac{r^2}{1 - q/q_s} \frac{\partial q}{\partial r} \right) \quad (1.36)$$

From the Equation (1.36), concentration dependent diffusivity is calculated by numerical techniques [43].

1.4 Metal-Organic Frameworks

As a basic adsorbent material, Zeolites are aluminosilicate based porous materials. They have been used for many years in petroleum industry as a catalyst, in detergents as water softeners, and they are also being used commonly in the commercial adsorbent sector. There are 206 unique zeolite types have been discovered and classified by Structure Commission of the International Zeolite Association, and their detailed structures can be seen in the book Atlas of Zeolite Types [44]. A zeolitic structure is shown in Figure 1.17 [45].

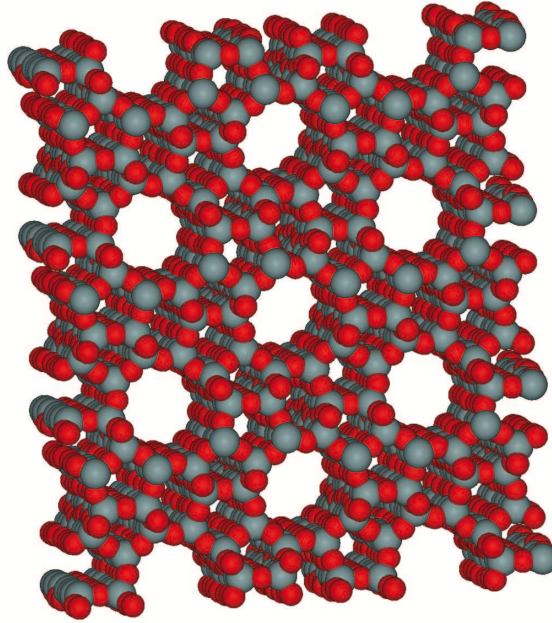


Figure 1.17: Zeolite Structure [45].

Requirements in adsorbent materials, couldn't have been satisfied by zeolites, because of their drastic pore limitation (<1 nm) and poor functionality could not provide the required specifications [46]. Therefore, researches developed a new kind of porous materials, called Metal–Organic frameworks.

Metal–Organic frameworks (MOFs) also known as porous coordination polymers, have been introduced to chemistry field by late 1990s, with their low density, high surface area, high adsorption enthalpy and large porous volume specifications those make MOFs favorable for hydrogen storage materials.

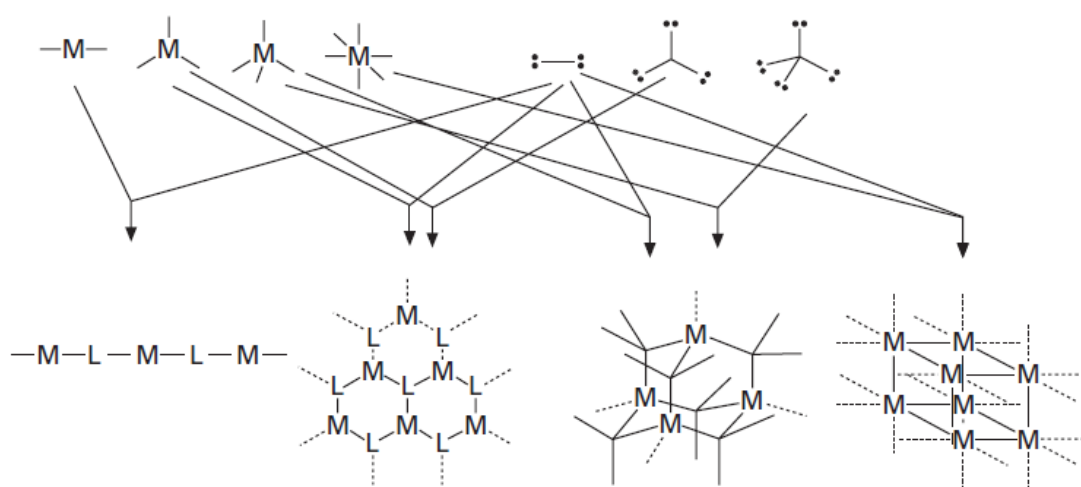


Figure 1.18: Assembly of nodes and linkers to form structures: Nodes on the left top, and linkers on the top right, forming metal-organic structures in the middle [47].

MOFs are crystal structures that are assembled by metal ions or metal clusters (as the nodes) and organic ligands as linkers (Figure 1.18). The most commonly used metal nodes are d-block transition elements. The number of sites (coordination numbers) available for binding ligands at the metal center range from 2 to 12 depending upon the choice of d- or f block metal and its oxidation state. Depending to the valence of an metal-ion, the metal binding sites may afford linear, T-shaped, tetrahedral, square-planar, square-pyramidal, trigonalbipyramidal, octahedral, cubic, trigonal-prismatic and pentagonal-bipyramidal nodes, although the geometries can be distorted by the choice of ligands and co-ligands [47]. Ligands are used as bridges to connect the nodes (metal clusters) to each other, and afford great flexibility in design for the synthesis of MOFs and can incorporate two or more electron donor groups to

bind to metal ions. The various organic molecules offer a wide range of linkers with different lengths, shape and connection numbers.

Characteristics of MOFs are usually specified by their pore volume or surface area, pore diameter, surface area and skeletal density. Pore diameter of a porous structure is defined as the diameter of sphere (such a sphere on Figure 1.19, as a yellow ball) that would fit into pore, as the van–der Waals radii of the wall atoms are considered.

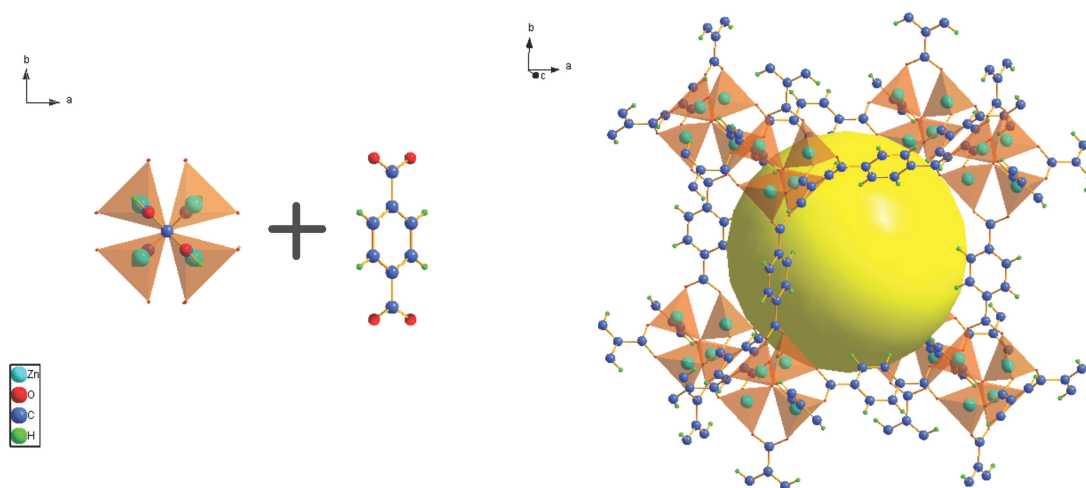


Figure 1.19: MOF-5 Crystal Structure: Metal Zn_4O node and carboxylate linker (left), and the complete structure (right).

The crystal structure of MOF-5 is given in Figure 1.19 as an example of MOF. It is seen from Figure 1.19, each Zn_4O cluster (node) connected with carboxylate organic compound (linker), they form cubic shaped porous structure (right). In some structures (as MOF-5 structure) nodes can be formed by metal-ions as polyhedras, to form the so-called Secondary Building Units (SBUs).

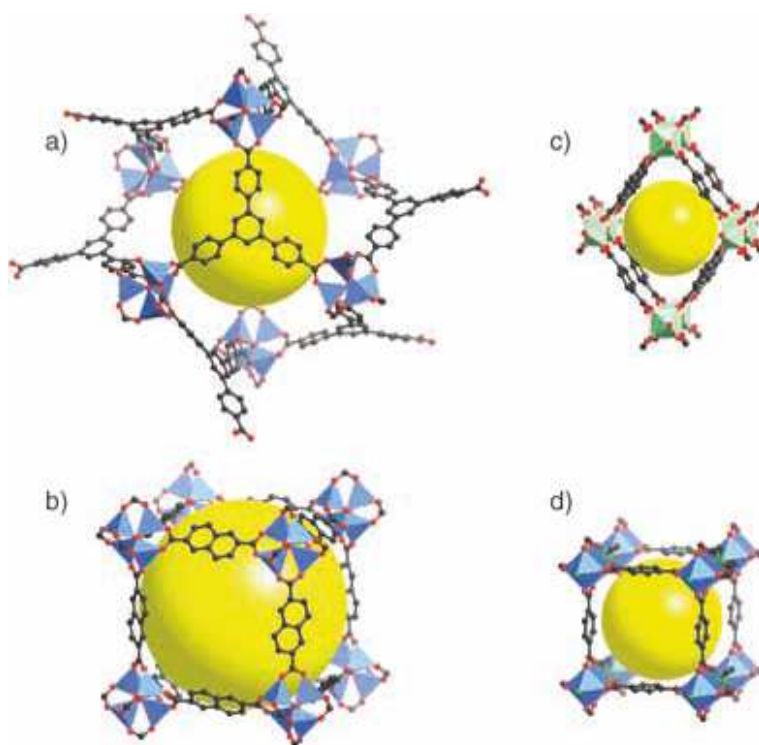


Figure 1.20: Examples of Metal-Organic Frameworks: a)MOF-177
b)IRMOF-8 c) MIL-53s (*Matériaux de l'Institut Lavoisier*)
d) $\text{Zn}_2 - (\text{bdc})_2(\text{dabco})$ ($\text{dabco} = 1,4 - \text{diazabicyclo}[2.2.2]\text{octane}$)
[49].

SBUs are essential to the design of directionality for the construction of MOFs and to the achievement of robust frameworks. They can be named upon their number of connections e.g. triangle, tetrahedron [48]. For example, in Figure 1.20 [49], it is seen that by altering SBUs and/or linkers different structures can be obtained. MOF-177 (Figure 1.20a) is constructed with $[\text{Zn}_4\text{O}]$ clusters and 4,4',4''-*benzene* - 1,3,5-*triyl* - *tribenzoate* (BTB), and each $[\text{Zn}_4\text{O}]$ connected to six carboxylate groups, and each tricarboxylate ligand connects to three $[\text{Zn}_4\text{O}]$ units [50], IRMOF-8 (Figure 1.20b), $[\text{Zn}_4\text{O}]$ node comprises four Zn(II) ions on the vertices of a tetrahedron with an O^{2-} moiety at the center of the tetrahedron. Each pair of Zn(II) ions are bridged by a carboxylate group, and therefore, each $[\text{Zn}_4\text{O}]$ node is connected to six carboxylate linkers constructing a simple cubic topology [47], whereas MIL-53 (Figure 1.20c) has parallel one-dimensional chains of $[\text{AlO}_4(\text{OH})_2]$ octahedra are connected by terephthalic acid linker to form a three-dimensional network.

On the other hand, MOFs could be classified by the linkers as well. For example, carboxylate based MOFs, they are constructed by using an ester or salt of carboxylate acids as linkers. One of the most famous member of this group, MOF-5, is shown in Figure 1.19. Another group of linkers, azolate-based MOFs, which are consist of imidazole, pyrazole, triazole and tetrazole ligands. In Figure 1.21 different type of triazolate linkers are given;

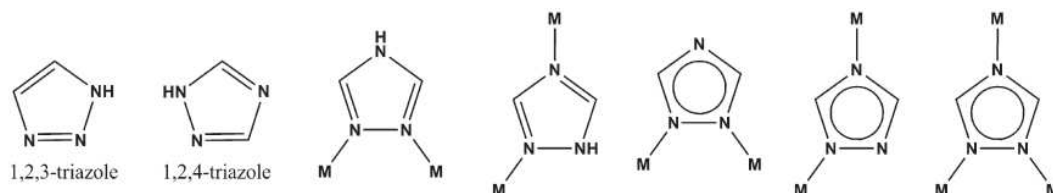


Figure 1.21: Triazolate based linkers: 1,2,3-Triazole, 1,2,4-triazole, and the coordination modes of 1,2,4-triazole and 1,2,4-triazolate [51].

Triazoles (subgroup in the azolates), made up from three nitrogen atoms and carbon atoms, and they can be grouped in two subcategories, by the position of N on the ring, as 1, 2, 3–triazole and 1, 2, 4–triazole (Figure 1.21 [51]). MFU-4 (Metal Organic Framework Ulm) is a metal-organic framework from Ulm University that is triazolate based nanoporous MOF where its crystal structure is given in Figure 1.22;

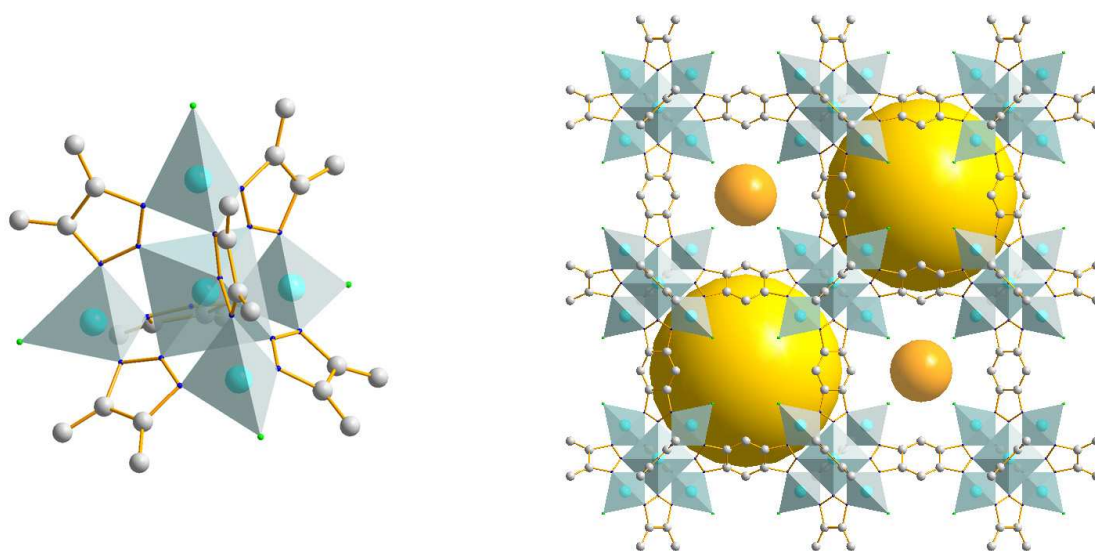


Figure 1.22: MFU4 Crystal Structure

MFU-4 $[\text{Zn}_5\text{Cl}_4(\text{BBTA})_3] \cdot 3\text{DMF}$, is constructed from pentanuclear $\{\text{Zn}_5\text{Cl}_4^{+6}\}$ secondary building units (SBUs) interconnected with BBTA linkers [52]. Each

Zn₅ unit is connected to six BBTA ligands by Zn–N bonds, whereas each ligand coordinating one central, and two peripheral Zn atoms. The framework has two different types of cavities (the smaller and the larger ones) arranged in an alternating fashion. Larger cells are represented by the cubic arrangement of chloride ligands having a minimum non-bonding distance of 4.25 Å to each other. The centre of the larger cells has a distance of 3.68 Å to each Cl atom. The aperture joining the two structurally different cavities is built up by 4 Cl atoms at a distance from 3.01 Å from its geometric centre. Taking the van der Waals radii of Cl atoms (1.75 Å) into account, imaginary spheres with a diameter of 3.87 Å could fit into the larger cells (which roughly corresponds to the van der Waals diameter of Ar atoms), and the aperture would admit the passage of an imaginary sphere with a diameter of 2.52 Å. Each of the larger small cells, on the other hand, is surrounded by twelve phenyl rings, and an imaginary sphere with a diameter of 11.94 Å would fit into it, taking the van der Waals radii of C atoms into account [52].

MFU-4.Br, [Zn₅Br₄(BBTA)₃] a very novel derivation of MFU-4, that is constructed by using {ZnBr₂} instead of {ZnCl₂} as the metal cluster and H₂ – BBTA as the linkers. Framework structure and physical properties of MFU4 and MFU4.Br are similar since the only difference is anions in the clusters, Cl[–] for MFU-4 and Br[–] for MFU-4.Br version. Even this small change may cause different structural behaviors (guest adsorption capacity, kinetics, flexibility etc.), since the strength of interactions in framework depend on the physical nature of nodes and the linkers of framework [53].

As stated above SBUs and linkers construction elements of MOFs, and they naturally control the surface area of a porous framework, which plays important role for gas storage applications. MOF-177 comes with 4526 m² g^{–1} BET surface area, whereas IRMOF-8, and MIL-53 (Figure 1.20b and c) possess 890 m² g^{–1} and 1100 m² g^{–1} BET surface area, and their H₂ storage capacities 7.5 wt%, 1.45 wt% [20], and 1.2 wt% [54] respectively. The relationship between the surface area and excess hydrogen storage capacity is shown in Figure 1.23;

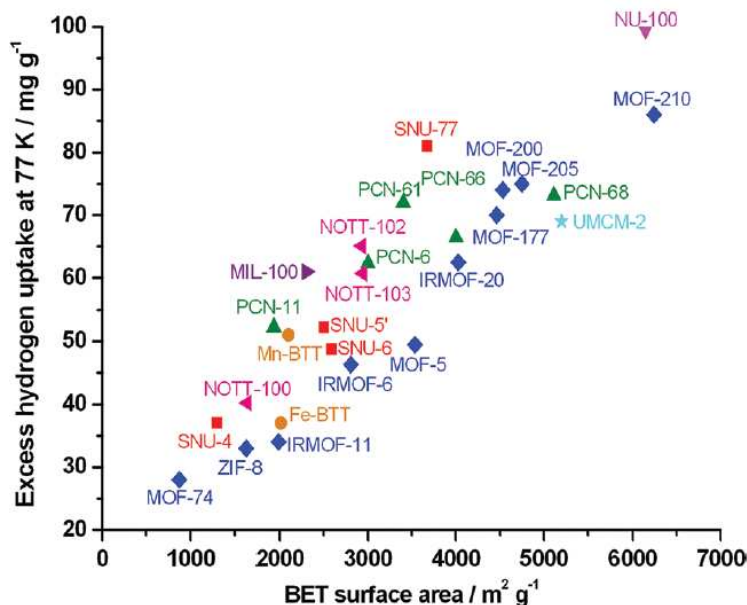


Figure 1.23: Excess high pressure H₂ uptake capacities at 77 K versus BET surface areas for some highly porous MOFs [20].

It is seen in Figure 1.23, excess H₂ storage capacity and BET surface area show linear relationship under high pressure loadings. However, this linear relationship can be broken at low pressure adsorptive loadings. It is because, at low pressure loadings, excess H₂ storage capacity can also be influenced by pore size, catenation, ligand functionalization, and open metal sites [20].

Flexibility is one of the remarkable features of MOF materials, that is a reversible structural transformation property of the most of the MOFs that includes stretching, “breathing”, rotational functions of the framework structure [55, 56]. The inorganic part of MOF is often associated with a rigid behavior, whereas the organic moieties correspond to flexibility. This behavior arise from the presence of external stimuli (e.g., temperature, hydrostatic pressure, presence of a sorbate) which is granted by the weak interactions within the framework structure, including coordination bonds, H-bonds [57], π -electron stacking interactions. To have such flexible framework following criterions needed to be satisfied [58]; SBU in the framework should have mirror plane with carboxylates, ratio of the number of carbons in the carboxylate surrounding the cluster to the number of metallic atoms within the cluster must be greater than two, the carboxylate should be involved to framework and the existence

of odd cycles in the structure, both at the level of the cluster and/or at the level of the topology of the skeleton, is unfavorable for dynamic effects, owing to their rigidity. The porous framework should possess these criteria simultaneously in order to have such flexible behavior. This kind of behavior emphasizes the importance of MOFs as they can be used in drug storage and delivery, adsorption and separation processes, and sensors applications.

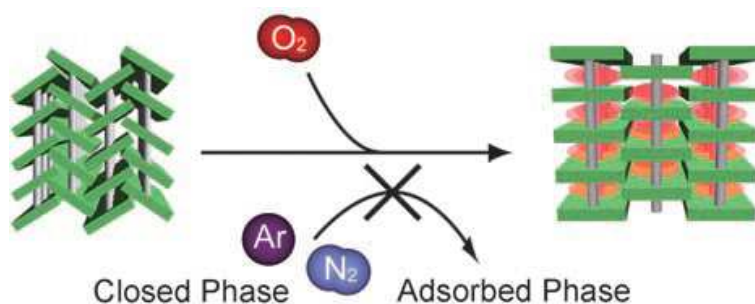


Figure 1.24: A depiction of gate opening process by adsorptive pressure [60].

In the case of rigid frameworks, a guest molecule with a diameter that is higher than the width of the opening between the cavities, would not move along the framework, therefore, such an adsorption process would be failed. Gate-opening process is considered within the sense of flexible behaviors of MOFs (Figure 1.24), that a gate refers to an opening that connects the cavities to each other in the framework structure. Stretching (opening) of gates is a process that is stimulated by external effects such as temperature [59], pressure [60], electric field and concluded to phase transformations in the frameworks [61], therefore, even a guest molecule that is larger than the gate can move along the gates during the adsorption/desorption process [62]. This structural behavior also causes wide hysteresis loop in adsorption/desorption isotherms [63] which is considered storing fluids at high pressure, keeping them adsorbed at much lower pressures (which is good for safety reasons), and releasing them completely at low pressures.

Guest molecules that they are moving throughout the framework, have to pass the gates to proceed among the cavities, which makes the gating effect fundamentally important, since that effect also modifies the diffusivity of guest molecules through the porous network. As a consequence, effective diffusion in the framework can be affected by

two barriers, cavities (small and large pores) and gates. Therefore, if gate structure involved a framework structure, diffusion would be limited by gate opening processes, that needs more activation energy in the comparison of diffusion activation energy of cavities [64].

MFU-4 (Figure (1.22)) and MFU4-type structure MFU-4l, have been investigated by the means of gating effect, also their adsorption and diffusion behavior were examined [35]. In the paper, they have shown that, MFU-4l with 9.1 Å pore aperture allows free diffusion and adsorption different guest molecules whereas MFU-4 with 2.5 Å pore aperture behaves highly selective in the sense of adsorption of guest molecules. Therefore they have proposed the MFU-4 for the molecular sieving applications, which has been successfully carried out by Hirscher M. *et. al.*. Since H₂/D₂ mixture separation is a crucial process for significant applications like fusion reactions, nuclear power production, it is found that H₂/D₂ mixture separated by exploiting narrow openings in MFU-4 structure (2.5 Å), that is called quantum-sieving technique with high selectivity results that had never been achieved before [65].

1.4.1 Production methods

MOFs can be synthesized by self-assembly of organic ligands and metal ions. There are two ways to tune pore size and provide desired surface chemistries: 1) direct assembly of new MOFs from particular metal nodes and organic linkers and 2) the pre-constructed robust precursor MOFs are modified by the post-synthesis. The porous materials in this study were synthesized by using direct assembly method with solvothermal and microwave irradiation synthesis techniques.

1.4.1.1 Solvothermal synthesis

Solvothermal synthesis is a method of producing chemical compounds where the constituents held together in an stainless steel autoclave at specified temperature and pressures for some time. It is similar to hydrothermal route, the only difference is that precursor solution is usually not aqueous. Thus, solvothermal synthesis allows for the precise control over the size, shape distribution, and crystallinity of metaloxide nanoparticles or nanostructures. These characteristics can be altered by changing

certain experimental parameters, including reaction temperature, reaction time, solvent type, surfactant type, and precursor type.

1.4.1.2 Microwave irradiation synthesis

Microwaves act as high frequency electric fields and will generally heat any material containing mobile electric charges, such as polar molecules in a solvent or conducting ions in a solid. Polar solvents are heated as their component molecules are forced to rotate with the field and lose energy in collisions, in other words, an increase in the heat of the material is observed as a consequence of resistance against current which is influenced by applied electric field.

The effect of microwave irradiation on chemical reactions is usually described by comparing time needed to obtain a desired yield of final products compared with conventional thermal heating. Research in the area of chemical synthesis has shown potential that advantages in the ability not only to drive chemical reactions but to perform them more quickly. The benefits of microwave irradiation method over the conventional methods can be itemized as follows [66];

- Microwave processing frequently leads to reduction in reaction times and higher yields
- The choice of solvent for the product is not governed by the boiling point but rather by dielectric properties of the reaction medium which provides an easiness to control of medium by adding polar materials
- The process is more-efficient since the in-core heating of the medium achieves uniform heating of the medium

As a summary, number of MOFs with their production methods and H₂ sorption characteristics are given in Table 1.1;

Table 1.1: Number of MOFs with their production methods and H₂ sorption data.

MOFs	Prod. Met.	Surf. Area (m ² g ⁻¹)	Temp. (K)	P.	H ₂ Uptake (%wt)	Heat of Ads. (kJ mol ⁻¹)	Avg. Grain Size (nm)	Diff. Coeff.(cm ² s ⁻¹)	Ref.
Li-Al(OH)(BDC)	solvothermal	958 (BET)	77	1 bar	1.76	6.3-4.9			[67]
Cu ₂ (abtc)(dmf) ₂		1260 (Langmuir)	77	1 bar	1.83				[68]
Cu ₂ (BPnDC) ₂ (4,4'-bpy)	solvothermal	2590 (BET)	77	1 bar	1.68	7.74			[69]
Co(HBTC)(4,4'-bpy)		887 (BET)	77	72 bar	2.05	7			[70]
Co ₃ (bpdc(4,4'-bpy))	solvothermal	922 (BET)	77	1 bar	1.98	7.1			[71]
Fe ₃ (OH)(pbpc) ₃		1200(BET)	77	1 bar	1.6				[72]
Mg ₃ (OH)(ndc) ₃ (dmf) ₄	solvothermal	190 (BET)	77	1 bar	0.78				[73]
Zn ₅ Cl ₄ BTA		1736 (BET)	77	20 bar	1.4	ca. 7			[35]
Zn ₄ O(BDC) ₃	solvothermal	1157 (Langmuir)	77	800 mmHg	0.5		200-500	2.3x10 ⁻⁹	[74]
Zn ₄ O(BTB) ₂		3275(BET)	77	1 bar	1.32	4<		0.103 (1/r _c ²)	[75]

It is known that mostly transition elements are used with appropriate linkers for the construction of MOFs. It is because, the electrons added to the transition metals go into the d-orbitals, however, because the energy of the 4s orbital is lower than the 3d orbital, the 4s orbital fills first. So, the outermost d orbitals are incompletely filled with electrons, then, transition metals can easily give and take electrons. It is common that metal ions can aggregate around a small anion, such as O^{2-} , OH^- or Cl^- , or with the donors of the bridging linker such as a carboxylate group. Therefore, using transition elements allow to generate framework structures that they can have varied directionality of linkers bringing ability to control pore size and shape. There are tens of zinc or copper based MOFs, but a few magnesium based MOFs because of the reason that d-block metals provide diversity, therefore, varied porous frameworks can be obtained with varying specifications such as pore shape and pore size.

As seen in Table 1.1, number of MOFs are given with their production methods and H_2 sorption data. Their H_2 uptake is surface area, H_2 uptake, and heat of adsorption are varied.

2. EXPERIMENTAL METHOD

Experimentally, the H_2 adsorption properties of two samples have been investigated and samples have been characterized utilizing scanning electron microscopy and XRD.

2.1 Sample Preparation

Both samples were synthesized by S. Biswas *et. al.*, who have investigated a different version of the samples in their study [52]. For the samples those investigated in this study, H_2 BBTA ligand has been synthesized by similar method that *Hart* and *Ok* used [76]. All other starting materials were of reagent grade and used as received from the commercial supplier.

One of the samples, **MFU4.Br-1** (MFU4 bromite version 1), was synthesized with solvothermal method which has been explained in Section 1.4.1.1. Synthesization has been carried out by following steps: a mixture of anhydrous $ZnBr_2$ and $H_2 - BBTA$ was dissolved in DEF, and this solution was placed in a glass tube. The tube was sealed and heated at 120 °C for three days, after cooling the sample was filtered and the remaining microcrystalline solid was washed with DEF. Afterwards $[Zn_5Br_4 (BBTA)_3]$ was dried in air.

Another sample, **MFU4.Br-2** (MFU4 bromite version 2), was produced with microwave irradiation method (see Section 1.4.1.2). A mixture of $ZnBr_2$ and $H_2 - BBTA$ in DEF, was placed in Pyrex sample tube. The sample tube placed in Microwave synthesizer (CEM, Discover S), and heated to 100 °C at 150 W, it was kept under this conditions for 10 minutes and then cooled to room temperature. Afterwards the resulting microcrystalline material, was washed with DEF and methanol, later the sample was allowed to dry at ambient conditions.

2.2 Sample Characterization

2.2.1 Sem & xrd investigations

To elucidate particle shape and particle size of the samples Scanning Electron Microscopy technique has been used. SEM images of the samples were taken by with FEI-Nova 600 NanoLab device, and they are shown on the Figures 2.1 and 2.2.

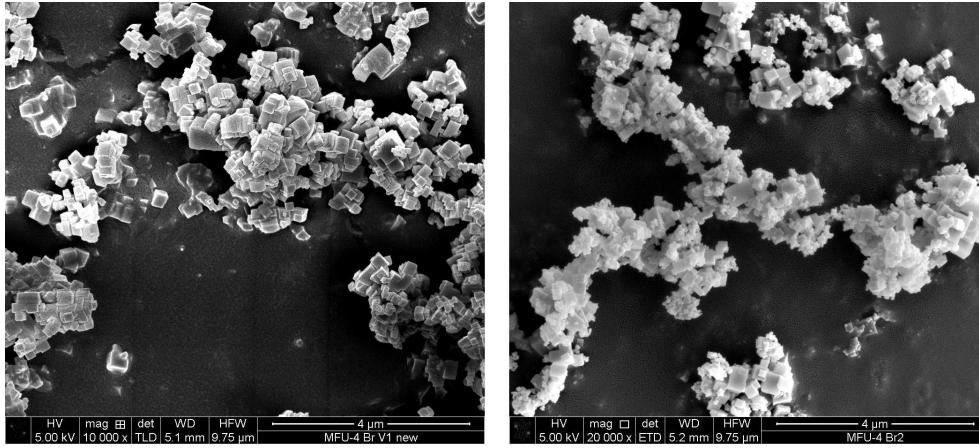


Figure 2.1: SEM Images of the Samples at 20000x magnification. Left: MFU4.Br-1
Right: MFU4.Br-2

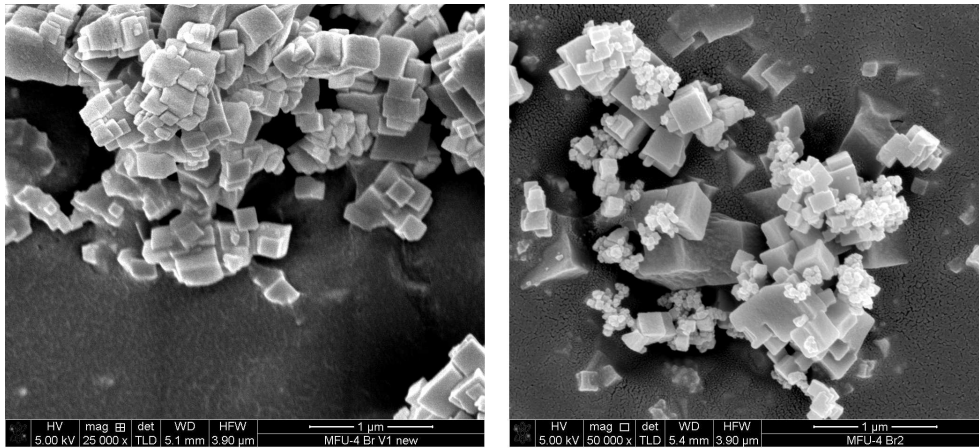


Figure 2.2: SEM Images of the Samples at 50000x magnification. Left: MFU4.Br-1
Right: MFU4.Br-2

As it is seen in Figures 2.1 and 2.2, crystalline shape of both of the samples are cubic. Nevertheless grain size distribution of the samples differs strongly. In order to obtain mean grain size of the samples, Fiji ImageJ, image analysis software has been used.

Images were loaded to the software, and 75 grains of MFU4.Br-1 and 200 grains of MFU4.Br-2 have been picked from the SEM images to calculate mean particle size. MFU4.Br-1 possesses uniform distribution profile, where the all grains show a similar size of about 190 nm (Figure 2.2 left) whereas MFU4.Br-2 possesses bimodal distribution with small and large grains of about 200 nm and 50 nm, respectively, which leads the average grain size of about 102 nm.

X-Ray diffraction method is used to determine the crystal structure of samples. In this study, XRD measurements were performed by the sample synthesizer group, Seifert XRD 3003 TT powder diffractometer equipped with a Meteor1D detector, 40kV, 40mA, $\text{Cu } K\alpha = 1.54178$, scan speed of 10 s per step and a step size of 0.02° in 2θ . For the MFU4.Br samples, there was no reference number to interpret the XRD peaks at that moment. Instead, a comparison between MFU4 and MFU4.Br has been done, since the only difference between MFU4 and MFU4.Br is the existing anion (Br^- instead of Cl^-) in the structures (see Section 1.4) therefore their XRD results should be similar.

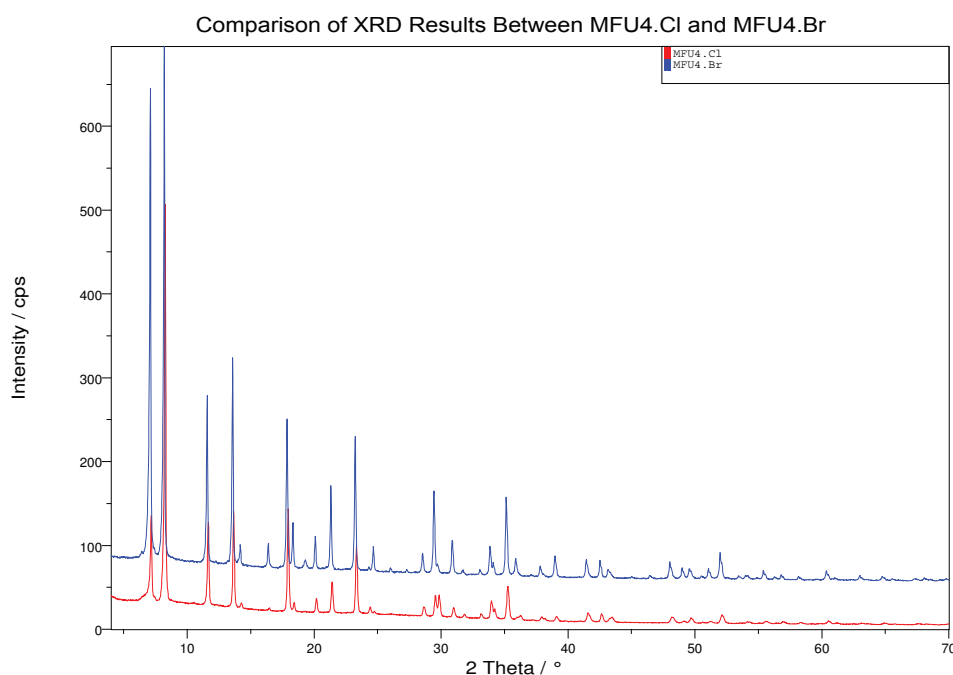


Figure 2.3: A Comparison of XRD Results between MFU4 Samples. Red: MFU4
Blue: MFU4.Br

In Figure 2.3, MFU4 and MFU4.Br XRD results have been compared. As it is seen in the Figure 2.3, the peaks are located almost at the same angles which is a proof of their

structure is the same, and the components of the MFU4 can be seen at the reference CCDC number 723714, 723715 and 723716 for MFU4 ([52]). A comparison of XRD results of MFU4.Br-1 and MFU4.Br-2 samples is given in Figure 2.4.

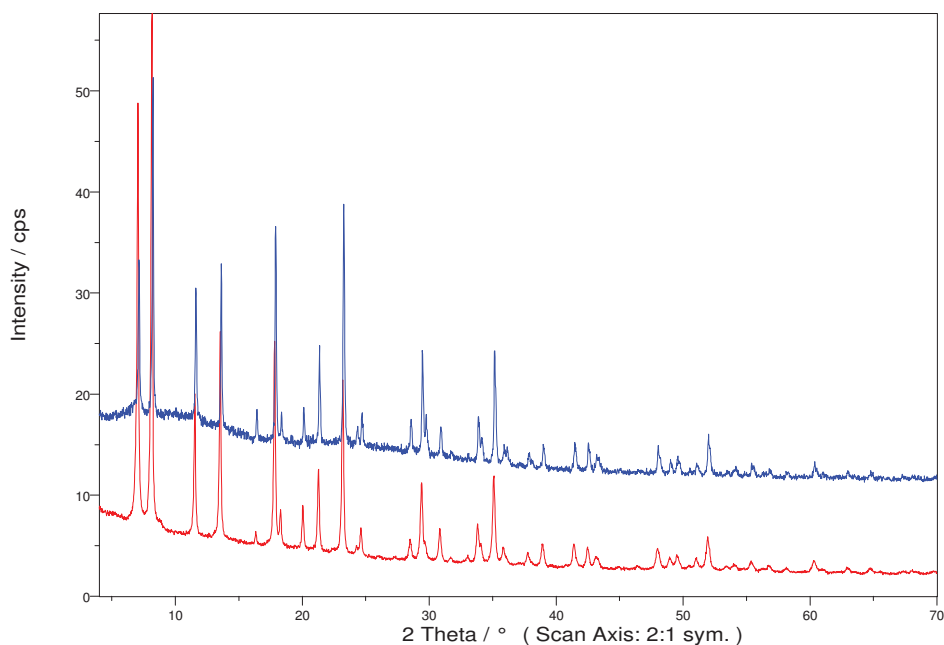


Figure 2.4: XRD Results of the Samples. Red: MFU4.Br-1 Blue: MFU4.Br-2

In Figure 2.4, there is no significant difference between the peaks. The difference can be observed only for the width of the peaks, due to the samples having different grain size distributions.

2.2.2 High pressure hydrogen storage

2.2.2.1 Measurement device

One of the possible ways to measure adsorption properties of porous materials as it is explained Section 1.3.4.1 is, exposing a material with a well-known amount of gas and precisely diagnosing the pressure drop according to adsorption which occurs on material surfaces.

In this study, PCTPro-2000 from HyEnergy LLC (Setaram Inc.) has been used to measure H_2 gas adsorption properties of the samples. The instrument measures adsorbed amount of H_2 using volumetric method (Section 1.3.4.1) employing high and low pressure transducers (from 0.1 to 200 bar). For the security measure, all hydrogen

valves and the pressure regulators are controlled pneumatically and there are no electric solenoid contact with the working gas. Temperature in the gas reservoirs is controlled to maintain a constant gas temperature with $\pm 1^\circ\text{C}$ uncertainty.

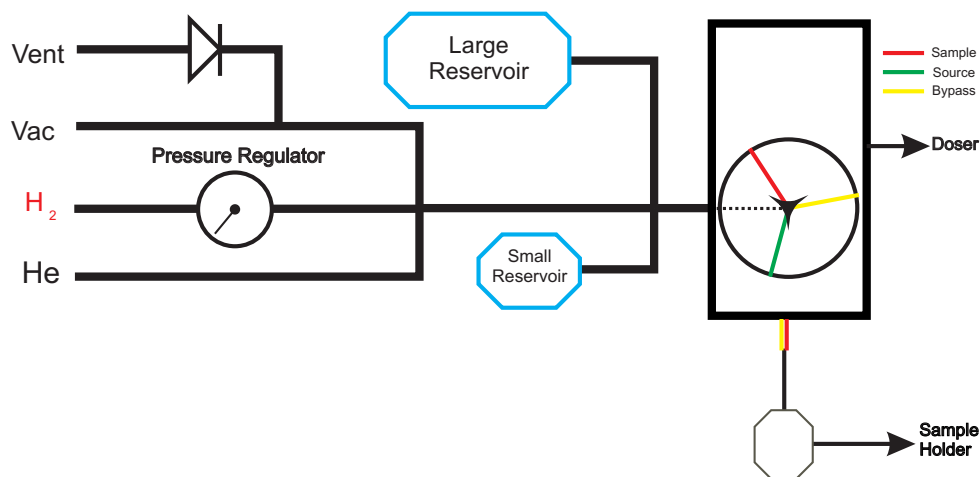


Figure 2.5: Representation of operating system of PCT.

Figure 2.5, shows the operating system of PCTPro-2000. H_2 and He gas supply tubes are connected to lines and the pressure of the tubes are adjusted by ordinary regulators. The amount of gas that will be introduced to the sample holder is adjusted by a pressure regulator (on the figure), then the adjusted amount of gas is released through the lines, to fill up the reservoirs. These reservoirs are connected to a doser which includes a rotating valve that is arranging the gas flow direction with three possible positions on it (the red, yellow and green lines on the doser, Figure 2.5). Position source, connects the reservoirs to a pressure gauge therefore enables the determination of the pressure in the reservoirs, the sample position on the rotating valve, connects the sample line to the gauge which helps to determination of the current pressure of the sample holder, and the third option, bypass, connects the reservoir line to the sample, which loads the gas in the reservoirs to the sample holder. The bypass option also evacuate sample by a turbo molecular pump connected to the V_{ac} line (vacuum line), when adsorption measurement is not in progress. The line **Vent** (ventilation) stands for removing of gas inside the lines, before vacuum process is started.

To start an adsorption measurement, volume of the empty sample holder should be known. Thus, the helium expansion test is performed prior to the adsorption

measurement in order to determine the empty sample holder volume and skeletal volume of materials. For that, the reservoirs and sample holder are evacuated for several hours, and helium gas is introduced into the reservoir. Since the reservoirs volume is already known as 0.51 cc, the amount of gas in the reservoirs can be calculated from the corrected ideal gas law that is given by Equation (2.1);

$$n_{He} = \frac{P_{He} V_{res}}{ZRT} \quad (2.1)$$

releasing the helium gas in the reservoirs and filling up the sample holder, cause a pressure drop in the reservoirs. This drop in the pressure, is used to calculate the sample holder volume by applying Ideal gas law with the correction factor;

$$V_{sh} = \frac{n_{He} \cdot R \cdot T \cdot Z}{P_{eq}} - V_{res} \quad (2.2)$$

The volume of empty sample holder (V_{sh}) is obtained by Equation (2.2). Therefore, skeletal volume of an adsorbent porous material can also be calculated. It should be noted that, before starting to determination of skeletal volume of porous material, porous material should be heated up to high temperatures (~ 200 °C) under evacuation, to remove remaining solvent in pores which comes from the production process of porous materials. Heating process (activation) can be easily carried out by using electrically resisting copper block (Figure 2.6). For the activation process, porous material is placed in the sample holder and heated above the evaporation temperature of solvent and maintained at this temperature for several hours under vacuum.

Afterwards, similar to the determination of the sample holder volume, skeletal volume of the sample is determined by Equation (2.3);

$$V_{sk} = V_{res} + V_{sh} - \frac{n_{He} \cdot R \cdot T \cdot Z}{P_{eq}} \quad (2.3)$$

In the adsorption measurement, adsorbed H_2 amount is calculated using former determinations. First, reservoir is filled with well-known hydrogen gas pressure P_{H_2} ,

then the reservoir valve is opened. In this case, a decrease in the gas pressure, P_{H_2} , arise from the expansion into the volume $V_{sh} - V_{sk}$ and adsorption of H_2 molecules on the surfaces of porous material. The adsorbed amount is the difference between the total amount of gas (n_{total}) and the amount of gas which is present in the gas phase at equilibrium;

$$n_{ads} = n_{total} - n_{H_2} = \frac{P_{ini} \cdot V_{res}}{Z_{P_{ini}} \cdot R \cdot T} - \frac{P_{eq} \cdot (V_{res} + V_{sh} - V_{sk})}{Z_{P_{eq}} \cdot R \cdot T} \quad (2.4)$$

the amount of H_2 obtained from Equation (2.4) (n_{ads}), refers to excess adsorbed amount (see Figure 1.6).

In the equations above (Equations (2.1)-(2.4)) the reservoir volume V_{res} , was already determined by company, once, as 0.51 cm^3 whereas the sample holder volume, V_{sh} , has been calculates as 1.27 cm^3 and these constant volumes were used in the calculations of adsorbed H_2 amount. Typically, 100–200 mg of sample mass is used, and the skeletal volume of sample has been determined prior to the each measurement.

All H_2 adsorption measurements have been performed in this work, following the procedure explained above. Nevertheless, to calculate the heat of adsorption of the sample, H_2 uptake measurements have been performed at varying cryogenic temperatures. These low temperatures allow obtaining precise results, since H_2 uptake is very low at ambient conditions. In this study, to obtain cryogenic temperatures in the sample holder, two substances have been used: one is liquid nitrogen, which has boiling point at 77 K, and the other one is liquid argon having the boiling point around 87 K. The run of the measurements at the cryogenic temperatures is based on cooling down the sample holder, simply, by sinking it down in a cryostat (Figure 2.6: left) which is filled with one of the liquids (argon, nitrogen). Since the liquids are at the ambient conditions, evaporation occurs from the open liquid surface and when the liquid goes down to a critic level which causes fluctuations in the temperature of sample holder. Therefore, the level of liquid in the cryostat has been controlled precisely (Figure 2.6a) during adsorption measurements.

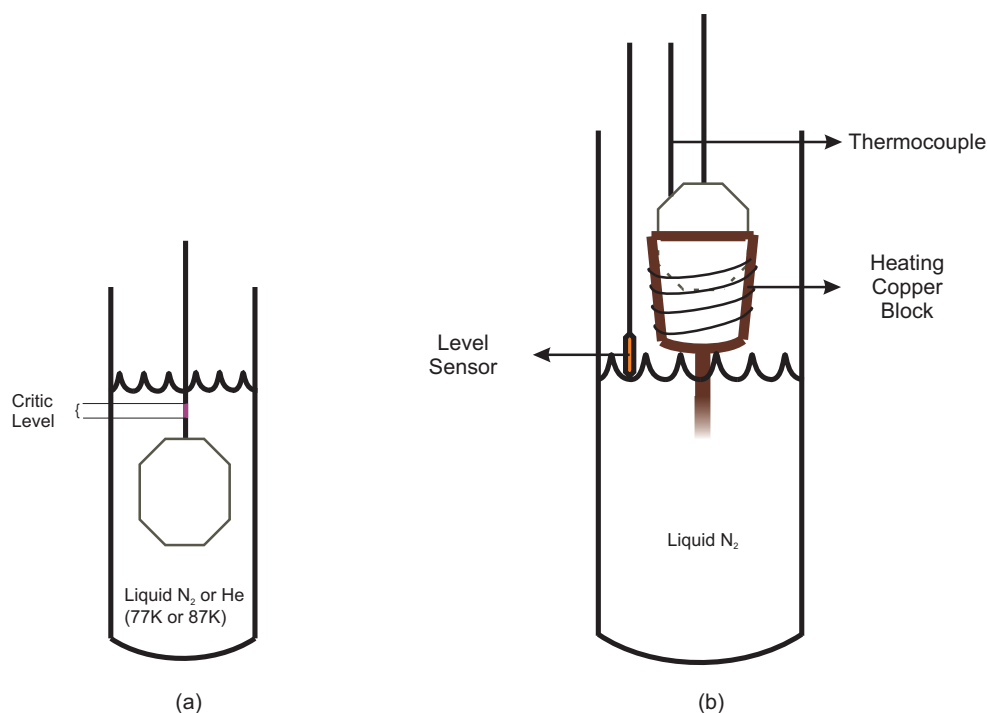


Figure 2.6: Cooling systems for the PCTPro-2000. Cryostat Bath for cooling with liquid nitrogen or liquid argon (a). Cooling system for temperatures above 87 K (b).

In order to obtain a better insight of adsorbate-adsorbent interaction, the sample needs to be cooled to cryogenic temperatures. As it is seen in Figure 2.6b, to perform the measurements at higher temperatures from the boiling temperature of liquid N₂ such those 97 K, 112 K, 127 K, sample holder is heated up to one of the desired temperatures with a resistive copper block. The electric current of resistive element is controlled by a PID controller, and since at these temperatures evaporation of liquid N₂ is fast, level of liquid argon in the cryostat has been checked by a sensor that give alerts when the liquid argon level goes down under the critic level (Figure 2.6b).

However, even the measurement temperature and the pressure in the sample holder is monitored precisely, an error introduced for the evaluation of adsorbed H₂ amount, since the gas densities vary between the cooled sample holder and the reservoir at ambient temperature. Therefore, this error is corrected by calibrating the equipment.

2.2.2.2 Calibration

As it mentioned before two calibration procedures are needed to obtain correct results. One is the calibration of the heating device and the other one is amount of adsorbed H_2 correction.

For the temperature calibration, to maintain the desired temperature in the sample holder (77 K, 87 K), the sample holder is waited at one of the temperatures for some time (approx. 45 mins), which ensures the temperature in the sample is equal with the measured temperature of the copper block. In order to justify that the measured temperature is equal to the actual temperature in sample holder at the temperatures higher than 87 K, H_2 adsorption measurement is performed twice; one is performed with liquid Ar and the second one with resistive block at the adjusted liquid N_2 temperature (87 K) to compare to the result of first one.

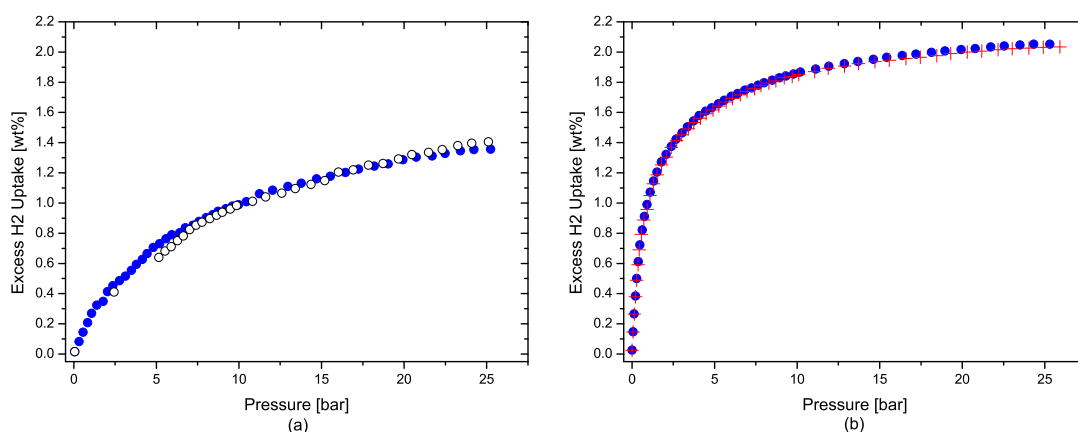


Figure 2.7: The adsorption measurements at 87 K. MFU4.Br-1, blue spheres show the adsorption isotherm at 87 K with liquid argon, and the white spheres show the adsorption isotherm at adjusted liquid nitrogen temperature ~ 87 K (a). MFU4.Br-2 blue spheres show the adsorption isotherm at 87 K with liquid argon and the red plus signs show the adsorption isotherm at adjusted liquid nitrogen temperature ~ 87 K (b).

Figure 2.7 shows, the adsorption measurements of MFU4.Br-1 and MFU4.Br-2 at 87 K with liquid argon and with adjusted liquid nitrogen temperatures, in Figures 2.7a and 2.7b. The adsorbed amounts in Figure 2.7 show a small deviation, arose from the temperature in the sample holder since it is adjusted with the PID controller.

The other calibration is done to eliminate temperature difference of the different regions of the instrument. For example, the temperature of reservoirs always at room temperature whereas the temperature in the sample holder varies by chosen measurement temperature (one of 77 K, 87 K, 97 K, 112 K, 127 K). Therefore the decrease in the pressure when the bypass valve turns to sample, is affected from three variables: one is from the expansion through the sample holder volume, the second one is the temperature difference between the reservoir and the sample holder and the last one from the amount of gas that is adsorbed on the surfaces of adsorbent. Since, the expansion volumes are known and constant, the temperature difference should be corrected to get the adsorbed amount of H₂.

To correct this, the instrument is operated with sea sand. Since H₂ adsorption is very low, -because of extremely low surface area of sea sand- compared to the amount of adsorbed by MOFs, sea sand could be considered as non-adsorbing material. This helps to determine the pressure drop that is affected from the temperature difference of the reservoir volumes and the sample holder. In order to get precise results, 5 different sea sand measurements were taken at each temperature. The plots of concentration in the sample holder against corresponding pressures are given in Figure 2.8

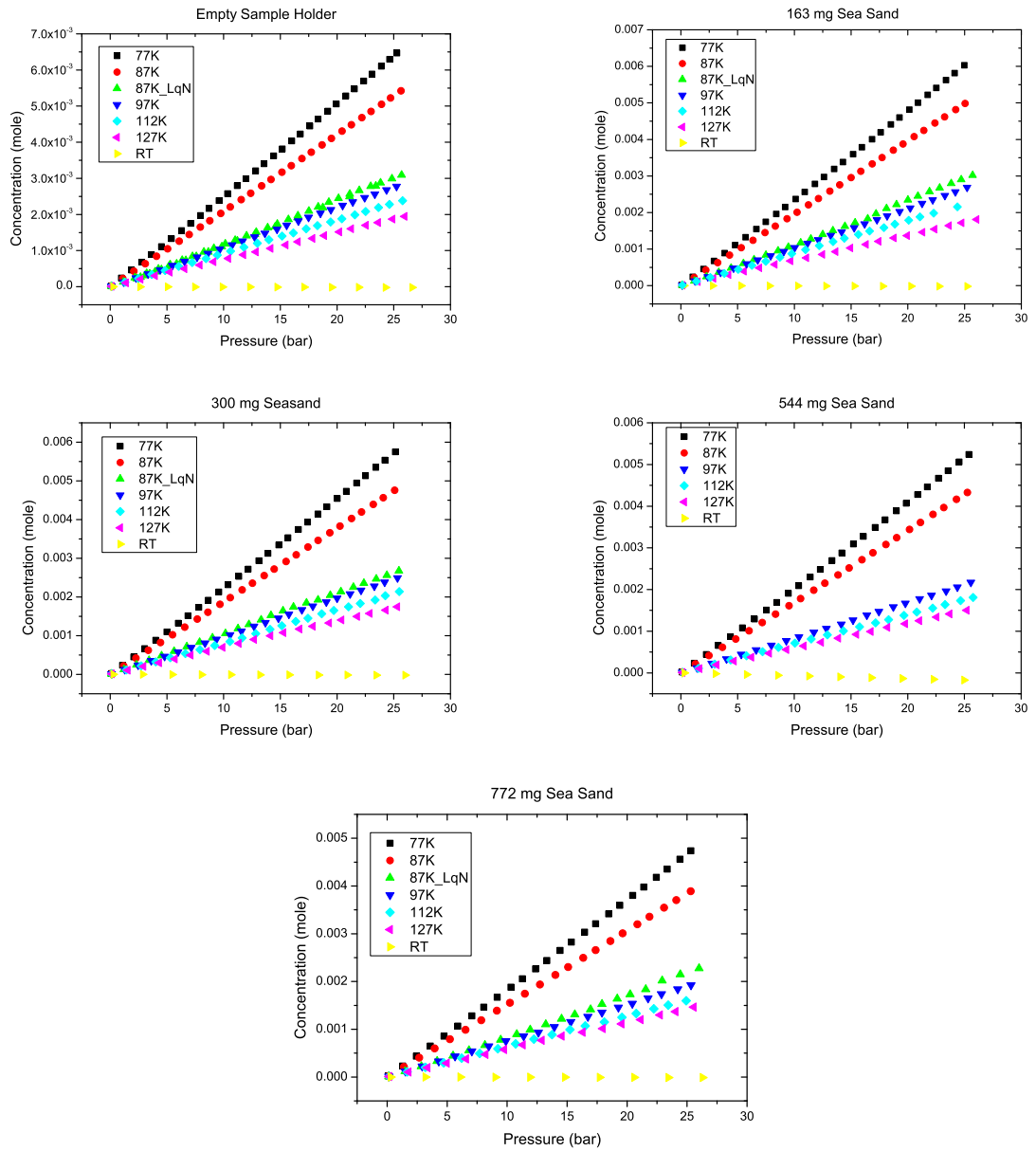


Figure 2.8: The adsorption measurements with different sea sand weights at different temperatures

In Figure 2.8, by decreasing the temperature, and increasing gas density H_2 concentration increases. The slopes in Figure 2.8, is used to derive a second plot which contains the slope of the each lines in Figure 2.8 on the y-axis, and the corresponding sea sand mass on the x-axis in Figure 2.9).

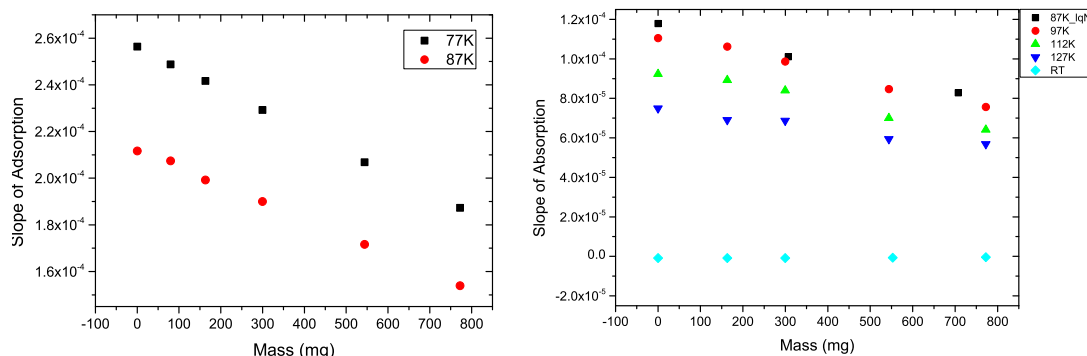


Figure 2.9: The slope of adsorption measurements with different sea sand masses and at different temperatures

In Figure 2.9, each point at the plots refer to the slope of a measurement that has been shown in Figure 2.8, by linear interpolating of these points a slope is obtained. Again the slope of each plot in Figure 2.9 is calculated and these slopes are subtracted from H_2 adsorption measurement plots of adsorbent. Thus, the error which is coming from the different volume expansion at different regions (reservoir and sample holder) is compensated, and the excess uptake of the porous material is obtained.

2.2.2.3 Procedures for measurements

Prior to each measurement, the samples have been activated at 150°C under high vacuum for 6 hours. To prevent any sample contamination by atmosphere, H_2 adsorption and desorption measurements have been performed right after activation process.

Adsorption and desorption measurements of the samples were obtained by Sievert-type apparatus, PCTPro-2000 instrument (Figure 2.5), at several temperatures (77 K, 87 K, 97 K, 112 K, 127 K 298 K) and equilibrium H_2 pressure in the sample holder allowed up to 25 bar. The progresses of the all adsorption measurements are typical and a sequence of an adsorption measurement is shown in Figure 2.10 as an example;

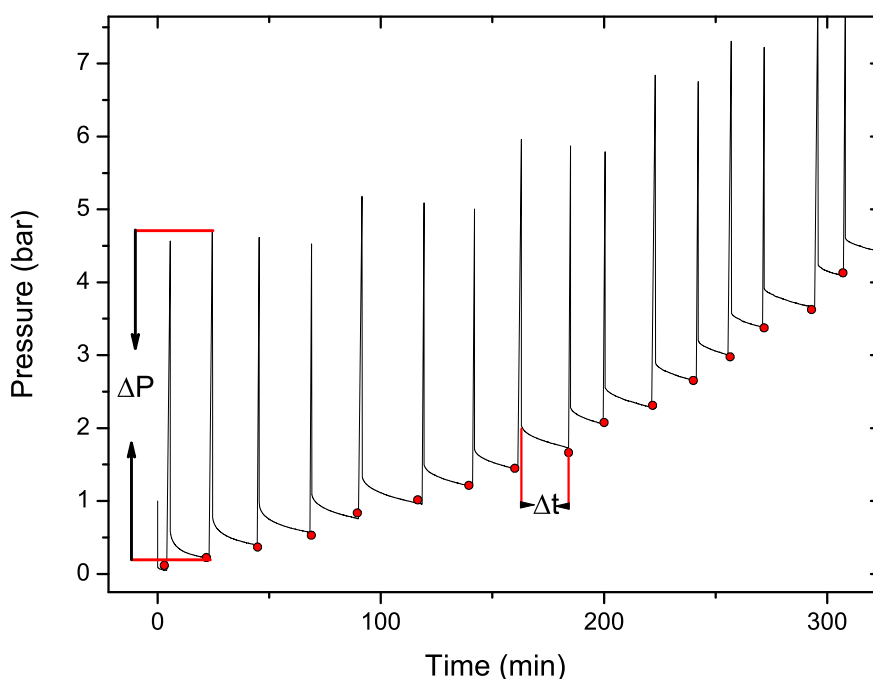


Figure 2.10: Progress of the PCT Measurement

At the beginning of the measurements reservoir in the instrument is filled with 1 bar H_2 pressure, then by-pass valve is released the amount of H_2 through the sample holder. After this point pressure changes in the sample holder is monitored by the instrument for some time (Δt in Figure 2.10) until equilibrium in concentration has been reached (very small changes in concentration). It should be noted that, the Δt depends on a variable that allows controlling the time span that is between the time hydrogen loaded to the sample holder, and the time H_2 pressure changes in the sample holder will be considered by the instrument. For example if the time span is chosen as one minute, after one minute H_2 loaded to the sample holder, the instrument will decide the equilibrium concentration is reached or not. When the H_2 pressure in the sample holder reaches an equilibrium concentration (see red dots in Figure 2.10), then the instrument turns the valve to source position, connection between reservoirs and the sample holder cut and next step takes place. Reservoirs are filled with higher pressure (ΔP on the figure) and then released through the sample holder. This progress goes until 25 bar equilibrium H_2 pressure is reached in the sample holder, and then desorption part of the measurement starts.

The desorption part is exactly reverse of the adsorption process, a lower gas pressure in the reservoirs than the pressure inside the sample holder is created, then the by-pass valve allows to pressure come to an equilibrium, which means H_2 gas pressure in the sample holder is sucked. Since desorption part of measurements is applied to check if the isotherm of sample shows hysteretic behavior or not, measurement is finished either at the pressure that the sample does not possess hysteresis or it shows permanent hysteretic behavior at relevant temperature. Total measurement time vary with the measurement temperature and the adsorption behavior of the sample in the holder.

The sorption measurements in this study have been performed by varying H_2 pressure loadings and the time spans. The details of the sorption measurements have been given in Table 2.1:

Table 2.1: Adsorption and desorption measurement characteristics of MFU4.Br-1 and MFU4.Br-2.

Temperature	No. ^a	MFU4.Br-1	No.	MFU4.Br-2
77 K	1	Adsorption	8	0 > P _{eq} > 10bar → ΔP : 4bar
		Desorption		10 > P _{eq} > 25bar → ΔP : 8bar
		ΔP : 10bar		ΔP : 10bar
		TS : 1 minute		TS : 1 minute
87 K	2	Adsorption	10	0 > P _{eq} > 10bar → ΔP : 4bar
		Desorption		10 > P _{eq} > 25bar → ΔP : 8bar
		ΔP : 10bar		ΔP : 10bar
		TS : 1 minute		TS : 1 minute
87 K	3	Adsorption	11	0 > P _{eq} > 10bar → ΔP : 4bar
		Desorption		10 > P _{eq} > 25bar → ΔP : 8bar
		ΔP : 10bar		ΔP : 10bar
		TS : 1 minute		TS : 1 minute
87 K	4	Adsorption	12	0 > P _{eq} > 10bar → ΔP : 4bar
		Desorption		10 > P _{eq} > 25bar → ΔP : 8bar
		ΔP : 10bar		ΔP : 10bar
		TS : 1 minute		TS : 1 minute

Table 2.1: Adsorption and desorption measurement characteristics of MFU4.Br-1 and MFU4.Br-2.

Temperature	No. ^a	MFU4.Br-1	No.	MFU4.Br-2
97 K	4	Adsorption	13	0 > P _{eq} > 10bar → ΔP : 4 bar
		Desorption		10 > P _{eq} > 25 bar → ΔP : 8 bar
	5	Adsorption	14	ΔP : 10bar
		Desorption		TS: 1 minute
112 K	6	Adsorption	15	0 > P _{eq} > 10bar → ΔP : 4 bar
		Desorption		10 > P _{eq} > 25 bar → ΔP : 8 bar
	7	Adsorption	16	ΔP : 10bar
		Desorption		TS: 1 minute
RT	8	Adsorption	17	0 > P _{eq} > 10bar → ΔP : 4 bar
		Desorption		10 > P _{eq} > 25 bar → ΔP : 8 bar
	9	Adsorption	18	ΔP : 10bar
		Desorption		TS: 1 minute

^a Number of measurements, and they are not related with experimental order.

TS The time span of relevant measurement.

In Table 2.1, there are different number of measurements at different temperatures and, applied H₂ pressures and time spans. The adsorption measurements below room temperature have been performed under the following conditions at once: between 0 and 10 bar equilibrium pressures, increment in H₂ pressure at each step (ΔP) has been applied as 4 bar whereas between 10 bar and 25 bar equilibrium pressures, H₂ pressure increment changed to 8 bar (ΔP). Nevertheless, in some of the measurements, applied H₂ pressure has been kept constant (measurement numbers: 9,11, and 12) and for measurement number 3, applied H₂ pressure changed 3 times as 4 bar, between 0 and 1.44 bar; as 10 bar between 1.44 bar and 4.19 bar; as 4 bar again between 4.19 bar and 4.46 bar; finally, applied H₂ pressure has been kept constant as 28 bar between 4.46 and 25 bar equilibrium pressures. For the desorption part of the measurements, 10 bar H₂ pressure difference has been applied between the sample holder and the reservoirs, until the pressures that hysteresis is not seen. For most of the sorption measurements, time span has been chosen as one minute, in the case of hysteretic behavior has been observed in a measurement, applied H₂ pressure and the time span conditions have been varied to eliminate the hysteretic behavior (77 K, 87 K measurements in Table 2.1).

When H₂ sorption measurement of sample is completed, equilibrium H₂ concentrations (red dots on Figure 2.10) at corresponding pressure are saved by the device, and these data have been reported as excess H₂ uptake isotherms.

3. RESULTS AND DISCUSSION

3.1 H₂ Uptake Results

H₂ adsorption and desorption properties of MFU4.Br-1 and MFU4.Br-2, have been investigated and the results are given below. The adsorbed H₂ amount has been reported in wt%, that is defined in the following equation;

$$\%uptake = \frac{m_{ads}}{m_{ads} + m_s} \quad (3.1)$$

where m_{ads} in the Equation (3.1) is the amount of hydrogen that is adsorbed on the surface of the samples, and m_s is the weight of samples.

H₂ adsorption isotherms of MFU4.Br-1 are shown in Figure 3.1;

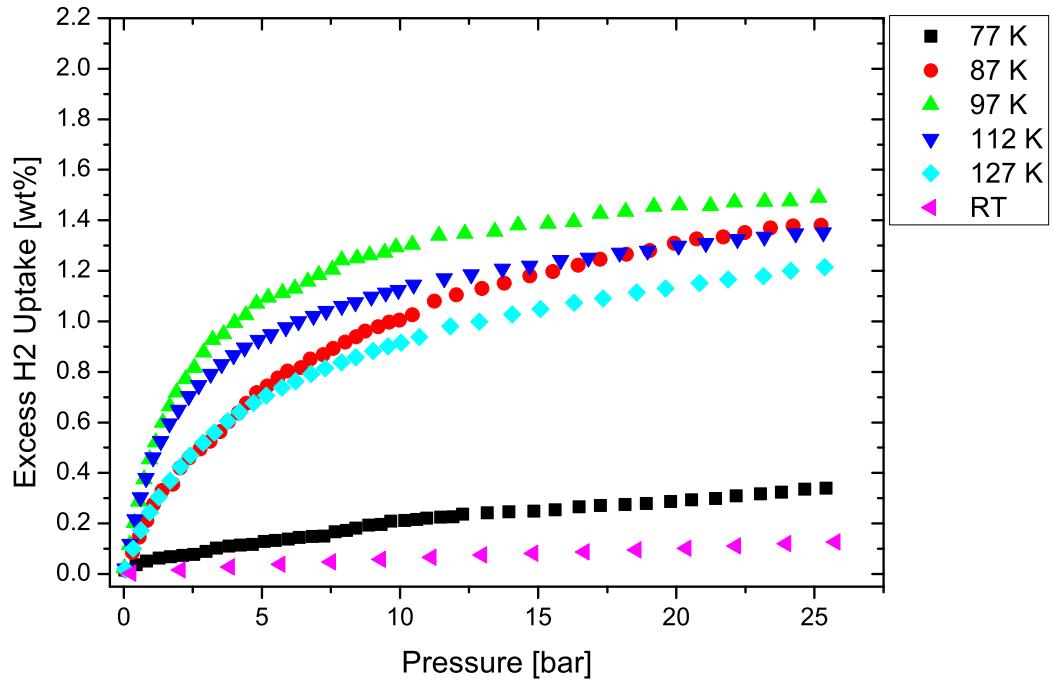


Figure 3.1: Full isotherm of MFU4.Br-1 at 77 K¹, 87 K², 97 K⁴, 112 K⁶, 127 K⁷, and RT⁸.

As seen in Figure 3.1, a distinct difference in the adsorbed H_2 amount has been observed at 77 K among the cryogenic temperatures, that the lowest H_2 uptake has been obtained at the lowest temperature (77 K). The adsorbed amount is increased by increasing pressure (isotherm shape is linear), indicating MFU4.Br-1 is not saturated at the given pressure range.

H_2 uptake increases and shows typical type I BET isotherm at 87 K. The isotherm shows a steep increase at low pressures and this steepness gets less pronounced as the loading pressure increases. Similar to the measurement at 77 K, maximum uptake could not be obtained at 87 K.

Likewise the isotherm at 87 K, the isotherm at 97 K shows a steep increase at low pressures that is getting saturated at high pressures. Additionally, as seen in Figure 3.1, the highest H_2 uptake has been obtained at 97 K.

H_2 uptake at 112 K, shows lower uptake than the uptake at 97 K, and similarly, the measurement at 127 K, exhibit lower uptake than the 112 K. Whereas at room temperature, the H_2 uptake increases linearly with increasing pressure that is due to H_2 uptake mainly correlates with the free volume, as the interaction between hydrogen molecule and the host surface is very weak at room temperature [20].

The adsorbed H_2 amount is increased by increasing temperature in the temperature range of 77 K-97 K, such behavior would not be expected in an exothermic process. However, this behavior has been observed with CuTEI by Zhao *et. al.*, that H_2 uptake at 77 K is less than that of 87 K, and in addition, H_2 uptake decreases where the measurement temperature is increased to 113 K [77]. Similarly, MFU4.Br-1 shows the lowest uptake at 77 K, that is due to strong blocking effect of the narrow apertures between the large and small cavities in the framework structure with the opening length of 2.52 Å. The apertures lead an inaccessible pore structure for the diffusing H_2 molecules with the kinetic diameter of 2.89 Å, these cannot overcome potential barrier of the aperture at 77 K. The H_2 uptake increases with increasing temperature up to the measurement at 97 K. The increase in the thermal energy leads to an increase in the kinetic energy of diffusing H_2 molecules while decrease in the kinetic barrier effect of the aperture. Therefore, H_2 molecules pass through the apertures and get

adsorbed into the large and small cavities. Subsequent to 97 K, H₂ uptake decreases as the measurement temperature is increased to 112 K and 127 K. Because the increase in the thermal energy interrupts H₂ molecules adsorbed on the surface of MFU4.Br-1. Apart from the adsorption isotherms, the H₂ uptake measurements at 77 K, 87 K, and 97 K show hysteresis. The isotherms are given in Figure 3.2;

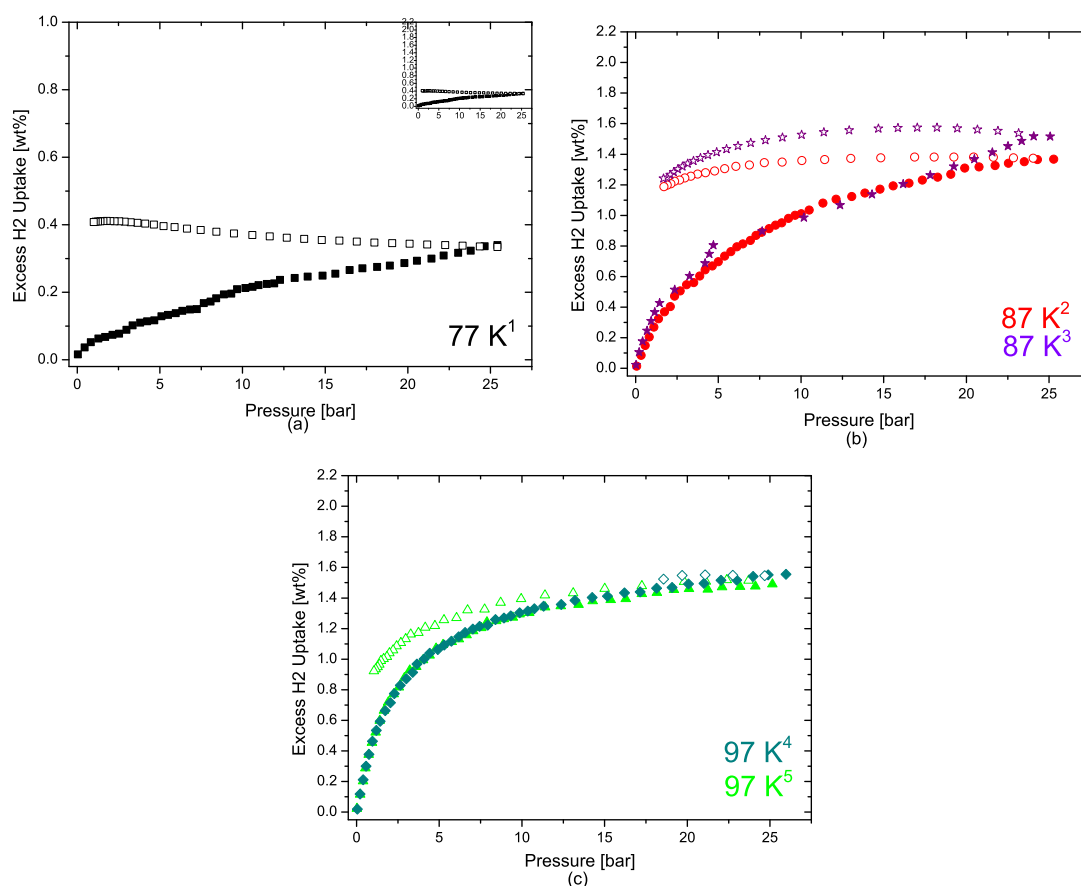


Figure 3.2: Adsorption and desorption measurements of MFU4.Br-1 at 77 K, 87 K, and 97 K: The full symbols show adsorption part of the measurement whereas the open symbols indicate the desorption part. The small numbers in upercase refers to the measurement number in Table 2.1

As seen in Figure 3.2, a difference exists in the adsorbed and desorbed amounts of H₂ in all three isotherms and it is getting more pronounced at low pressures. Particularly at 77 K, adsorbed H₂ amount increases with decreasing pressure in the whole desorption part of the measurement. However, H₂ uptake starts to decrease below ca. 18 bar for both of the measurement, no:2 and 3 at 87 K, and this decrease occurs below ca. 22 bar in the desorption part of the measurement taken at 97 K. Nevertheless, the difference

in the adsorbed and desorbed H_2 amounts get less pronounced as the measurement temperature increases.

The hysteresis mechanism at all three temperatures is the same: H_2 molecules still diffuse into the grains of MFU4.Br-1, even in the desorption part. This is because of the fact that a real equilibrium time needed for the sorption process in those kinetically closed pores is much longer than the experimental time scale [77]. The kinetic energy of the diffusing H_2 molecules is not sufficient to pass through the apertures, also fill the grains in a reasonable time in the adsorption part. As a consequence of that, H_2 molecules get adsorbed in the desorption part of the measurements, as well.

The reason for the progressive uptake behavior in the desorption part of the measurement at 77 K is that the kinetic blocking effect so strong that the H_2 concentration cannot reach an equilibrium at any given pressure in the provided time of the adsorption, therefore, they still diffuse into the grains in the whole desorption part of the measurement.

Nevertheless, since the mobility of the H_2 molecules at 87 K is faster than that of 77 K, H_2 molecules fill the grains completely within the less time compared to 77 K, but still in the desorption part. Subsequent to grain filling, H_2 uptake decreases with decreasing pressure, because H_2 molecules start to be sucked out from the grains, after the filling time in the desorption part. Although the time span has been increased to 40 minutes (check the measurement conditions on Table 2.1) to remove the hysteresis at 87 K, the difference in the adsorption and desorption isotherm became wider, that is because less time spent for the adsorption isotherm in middle pressure range (less points obtained in the middle pressures, see in Figure 3.2b) than the desorption part pressure ranges.

However, the hysteresis becomes narrower at 97 K (Figure 3.2c), that is due to mobility of the H_2 molecules increases, so they fill and empty the grains faster in comparison to measurements performed at 77 K and 87 K.

H_2 uptake results for MFU4.Br-2, are shown in Figure 3.3;

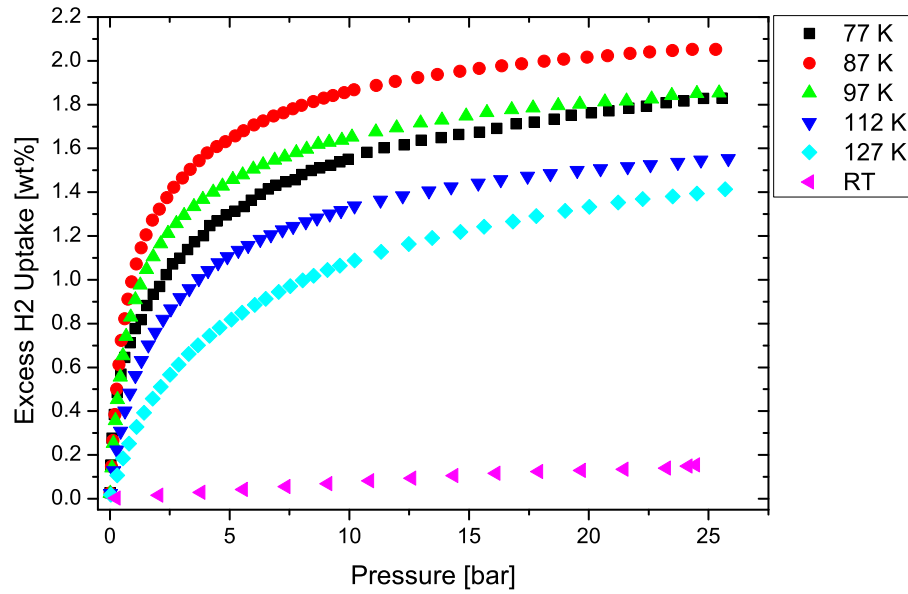


Figure 3.3: Full isotherm of MFU4.Br-2 at 77 K⁸, 87 K¹⁰, 97 K¹³, 112 K¹⁴, 127 K¹⁵, and RT¹⁶.

As seen in Figure 3.3, adsorption isotherms of MFU4.Br-2 similar to the adsorption isotherms of MFU4.Br-1, except 77 K. In spite of the hysteretic behavior of MFU4.Br-1, the hysteresis disappears above 77 K, indicating smaller diffusion barrier exist within the grains of MFU4.Br-2, leading to higher uptakes at each temperature than that of MFU4.Br-1 (see table 3.1).

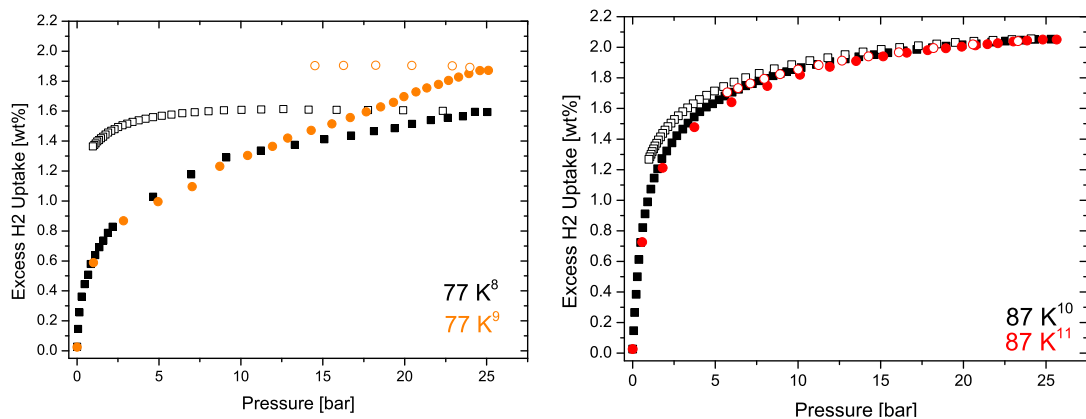


Figure 3.4: Adsorption and desorption measurements of MFU4.Br-2 at 77 K, and 87 K: The full symbols show adsorption part of the measurement whereas the open symbols indicate the desorption part. The small numbers in uppercase refers to the measurement number in Table 2.1

As seen in Figure 3.4, MFU4.Br-2 possesses hysteretic sorption behavior at 77 K and 87 K. The mechanism of the hysteresis of MFU4.Br-1 is the same as MFU4.Br-1 that, the H₂ molecules diffuse into MFU4.Br-2 grains in the desorption part. In the measurement no.8, below ca. 12 bar H₂ molecules come out from the MFU4.Br-2 grains in the desorption part. Even the time span has been increased to 30 minutes, hysteretic behavior remained at 77 K. The hysteresis became narrower at 87 K with the time span conditions of 1 minute and 20 minutes (measurement no.10 and 11). However, when the time span is increased to 40 minutes, the hysteresis disappeared at 87 K.

Table 3.1: H₂ uptakes in wt% and corresponding measurement times of MFU4.Br-1 and MFU4.Br-2.

	MFU4.Br-1	MFU4.Br-2	Ratio of [wt %]s*
	[wt %]	[wt %]	
77 K	0.33 ¹	1.82 ⁸	5.52
87 K	1.38 ²	2.05 ¹⁰	1.49
97 K	1.49 ⁴	1.85 ¹³	1.24
112 K	1.35 ⁶	1.55 ¹⁴	1.15
127 K	1.21 ⁷	1.41 ¹⁵	1.17
RT	0.12 ⁸	0.15 ¹⁶	-

*: Ratios have been calculated as ratio of MFU4.Br-2 to MFU4.Br-1.

The numbers in uppercase refers to the measurement numbers in Table 2.1.

As seen in Table 3.1, H₂ uptake increases with increasing temperature among the varying temperature ranges between the samples. H₂ uptake of MFU4.Br-1 increases at all temperatures (77 K, 87 K, and 97 K), whereas, MFU4.Br-2 shows similar increase after the temperature of 77 K to 87 K. The difference in the temperature range between the samples, arises from the mobility of H₂ molecules is being higher in MFU4.Br-2 than that of MFU4.Br-1. The ratio of H₂ uptake of the samples is very high at 77 K, and it starts to decrease by increasing the measurement temperature, indicating that the temperature dependence of MFU4.Br-1 (large grains) is stronger than MFU4.Br-2. The stronger temperature dependence probably arises from the differences in the average grain sizes between the samples.

H₂ uptake isotherms at 112 K and 127 K are fully reversible (showing no hysteresis) for both of the sample, and a comparison between the isotherms are given in Figure 3.5.

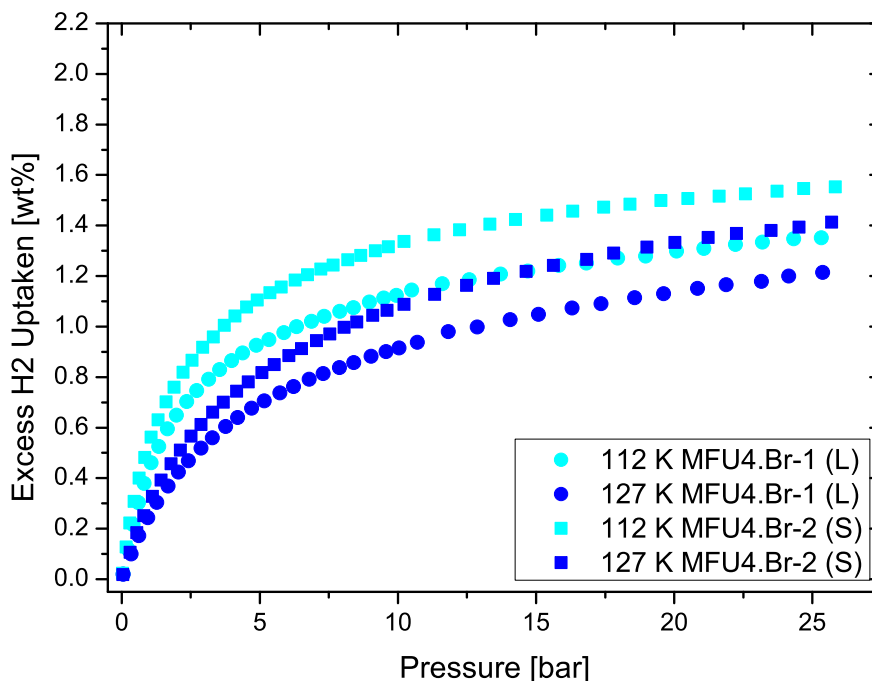


Figure 3.5: Excess uptake comparison between MFU4.Br-1 and MFU4.Br-2 at reversible temperatures, 112 K and 127 K. Same colors indicate same temperatures whereas same symbols indicate the uptake data for that sample at different temperatures. L and S in the figure, indicate the mean particle size as large and small, respectively.

As seen in Figure 3.5, a difference has been observed in the H₂ adsorption isotherms between the samples, at 112 K and 127 K. This difference would not be expected at the temperatures where the isotherms are reversible, since the chemical composition and the crystal structure of the samples are the same. The only difference between the samples, is their grain size distribution. However, no reason could have been told with the grain size distributions that would elucidate the difference in the uptake of MFU4.Br-1 and MFU4.Br-2 at the temperatures where the isotherms are reversible.

3.1.1 Heat of adsorption

In the previous section, the H_2 uptake of the samples and their hysteretic behavior has been discussed. Although the amount of H_2 that is taken up from the sample is important property among the porous H_2 storage materials, in addition to that, the binding strength of the H_2 molecules on the surface of the materials has a great importance, as it has been explained in Section 1.2.2.3.

The binding strength of H_2 molecule on a surface is determined by isosteric heat of adsorption. The isosteric heat of adsorption of the samples, has been calculated from the absolute adsorption isotherms and Clausius-Clapeyron equation (see Equation (1.2) in Section 1.3.4.1) and the results are given in Figure 3.6;

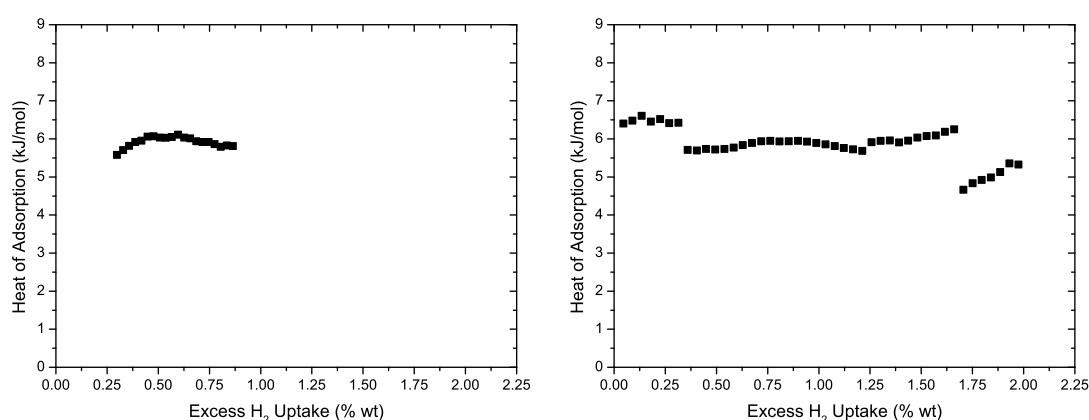


Figure 3.6: Heat of adsorption of MFU4.Br-1 (left) and MFU4.Br-2 (right).

As seen in Figure 3.6, MFU4.Br-1 and MFU4.Br-2 possesses $\sim 6 \text{ kJ mol}^{-1}$ heat of adsorption. In a microporous structure with a varying pore size, its heat of adsorption would be expected as distinct regions indicating the heat of adsorption in the small pores and the large pores. However, in Figure 3.6 almost constant high heat of adsorption has been observed due to the diffusion of H_2 molecules controlled by the small pore or aperture [35, 78]. Since the small and large pores exist in an alternating fashion in the MFU4.Br structure, H_2 molecules cannot diffuse independently from the pore size therefore the distribution of the heat of adsorption cannot be separated upon the pore sizes.

It should be noted that, since the four adsorption isotherms are reversible (87 K, 97 K, 112 K, and 127 K), the heat of adsorption of MFU4.Br-2 have been determined over a wide range of surface coverage (Figure 3.6 right). On the other hand, since only the two isotherms are reversible (at 112 K and 127 K, see Figure 3.2) for MFU4.Br-1,

therefore the heat of adsorption of MFU4.Br-1 has been calculated in limited range of uptake. At low pressures the uptake curve is very steep and at high pressures a large error in the uptake is introduced, therefore the heat of adsorption of MFU4.Br-1 has been calculated in medium pressure ranges of the measurements at 112 K and 127 K. Even though initial and final heat of adsorptions of MFU4.Br-1 are missing in Figure 3.6, middle ranges overlap with MFU4.Br-2 as expected for the same structures.

3.2 Kinetic Evaluations

To interpret the progress of the diffusing H_2 molecules in the samples, the kinetics of the adsorption measurements of the samples have been investigated. For a comparison, the plots of H_2 uptakes, fractional concentrations and the duration of samples are given in one figure. It should be noted that the plots are given below, evaluated from identical measurement conditions among the samples. The fractional concentration refers to the ratio of each concentration to 25 bar equilibrium concentration. The results are as following;

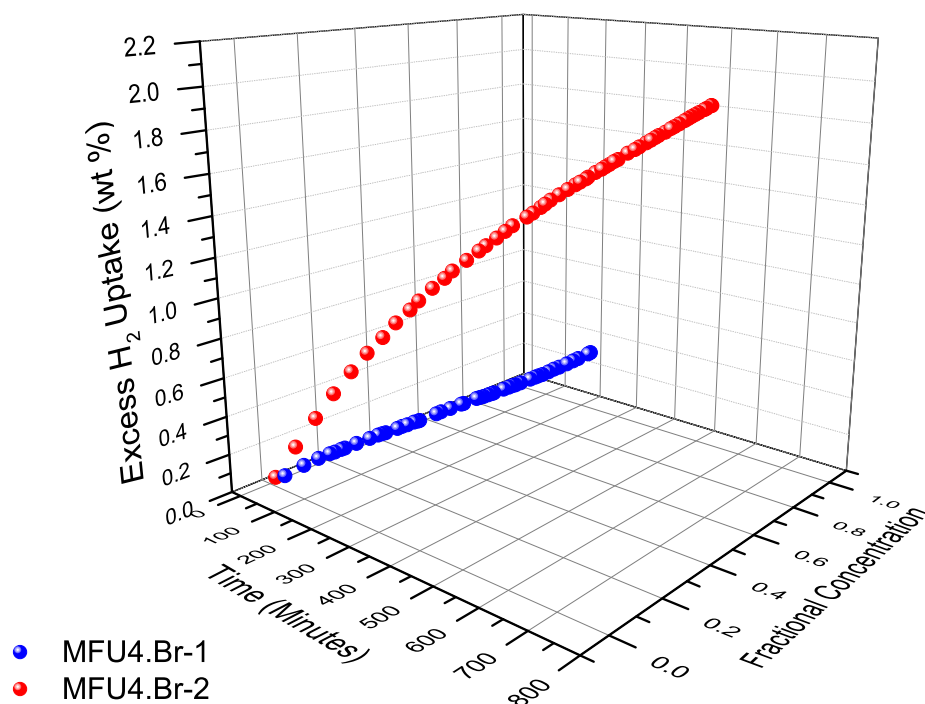


Figure 3.7: Kinetic Behavior Comparison between MFU4.Br-1 and MFU4.Br-2 at 77 K

As seen in Figure 3.7, MFU-4.Br-1 shows very low uptake in a short time. As it is stated before that because of the kinetic barrier effect is strong at 77 K, the measurement has been completed in short time (~ 200 minutes). However, the measurement time of MFU4.Br-2 at 77 K is longer due to lower kinetic barrier effect comparison to MFU4.Br-1 which allows the H_2 molecules diffuse through the framework, leading to the longer measurement time (~ 700 minutes).

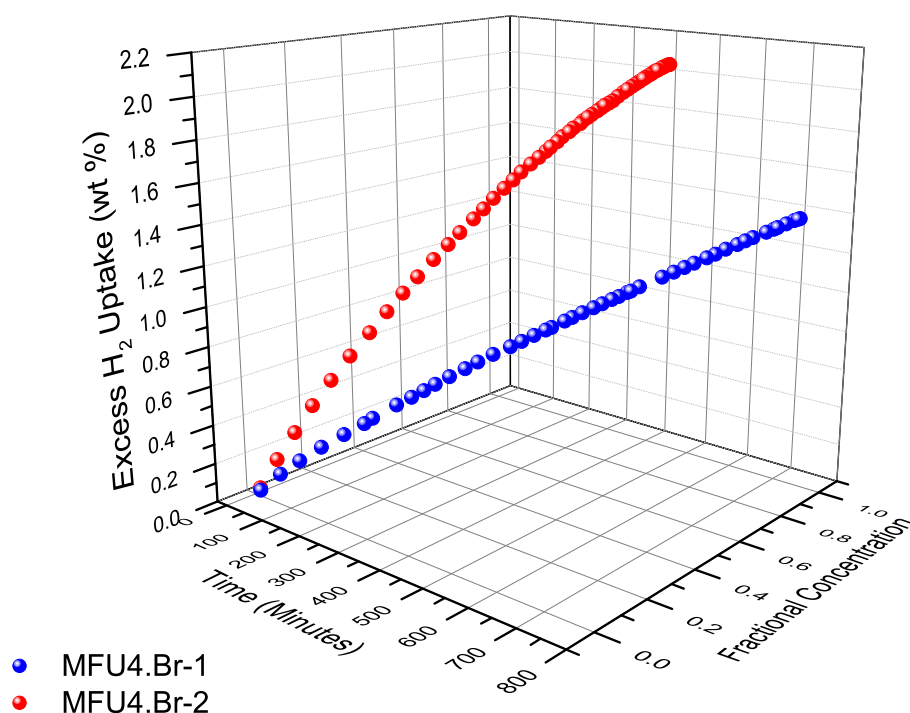


Figure 3.8: Kinetic Behavior Comparison between MFU4.Br-1 and MFU4.Br-2 at 87 K

As seen in Figure 3.8, when the measurement temperature increased to 87 K, duration of MFU4.Br-1 measurement became longer whereas the duration of MFU4.Br-2 took less than that of at 77 K. Besides, the H_2 uptake of the both samples have been enhanced.

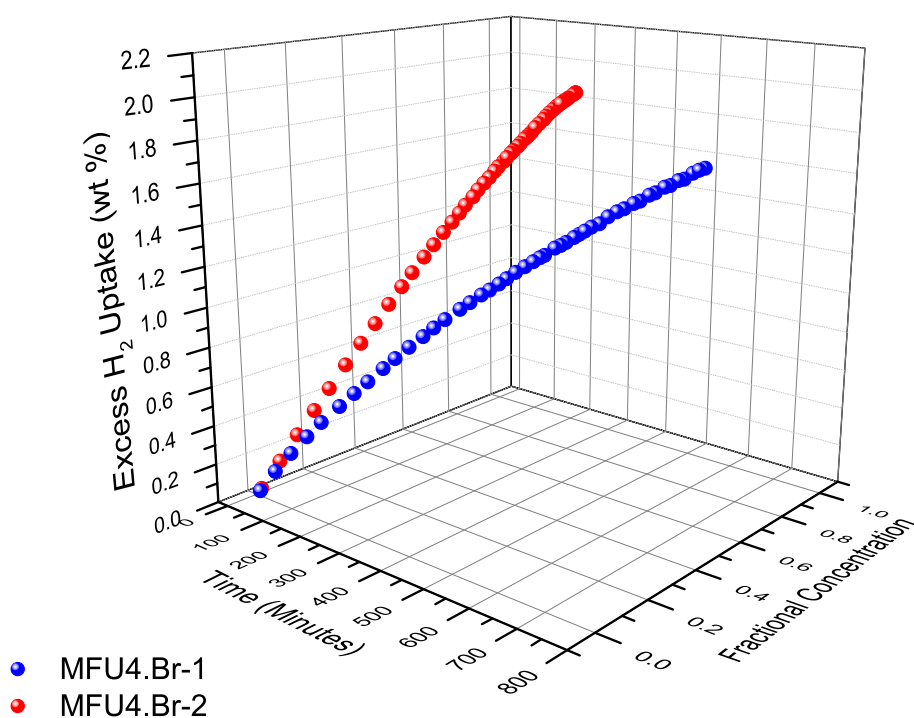


Figure 3.9: Kinetic Behavior Comparison between MFU4.Br-1 and MFU4.Br-2 at 97 K

Uptake measurements get shorter for both of the samples after 87 K. However, H₂ uptake of MFU4.Br-1 increases whereas the H₂ uptake of MFU4.Br-2 decreases when the temperature is increased to 97 K from 87 K (Figure 3.9).

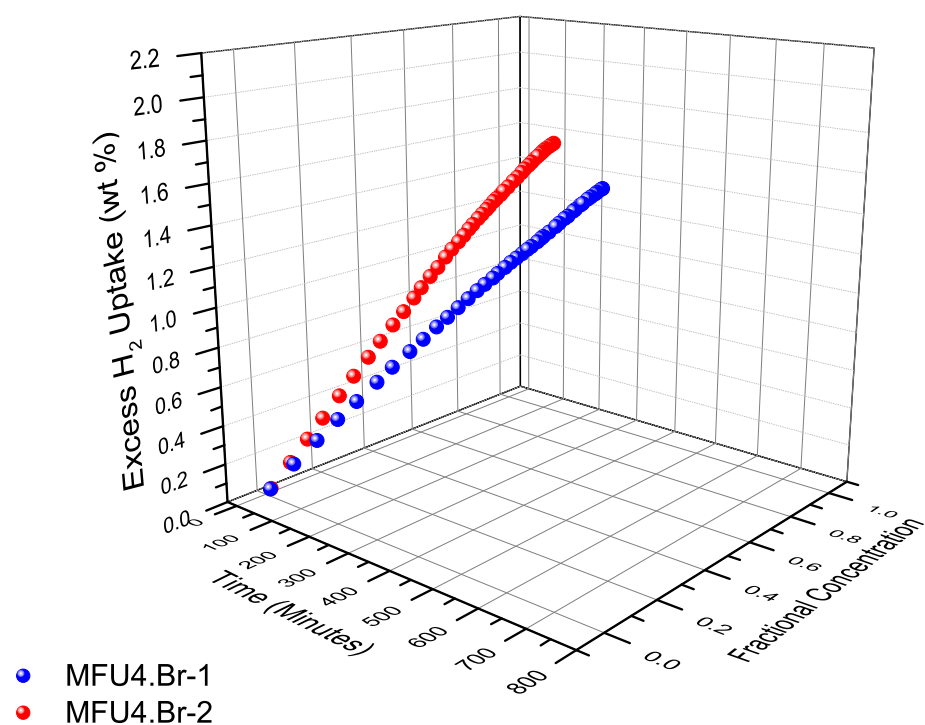


Figure 3.10: Kinetic Behavior Comparison between MFU4.Br-1 and MFU4.Br-2 at 112 K

Similarly, measurement times get closer to each other, at the measurement 112 K. As seen in Figure 3.10, H₂ uptake and the measurement time are both decreased.

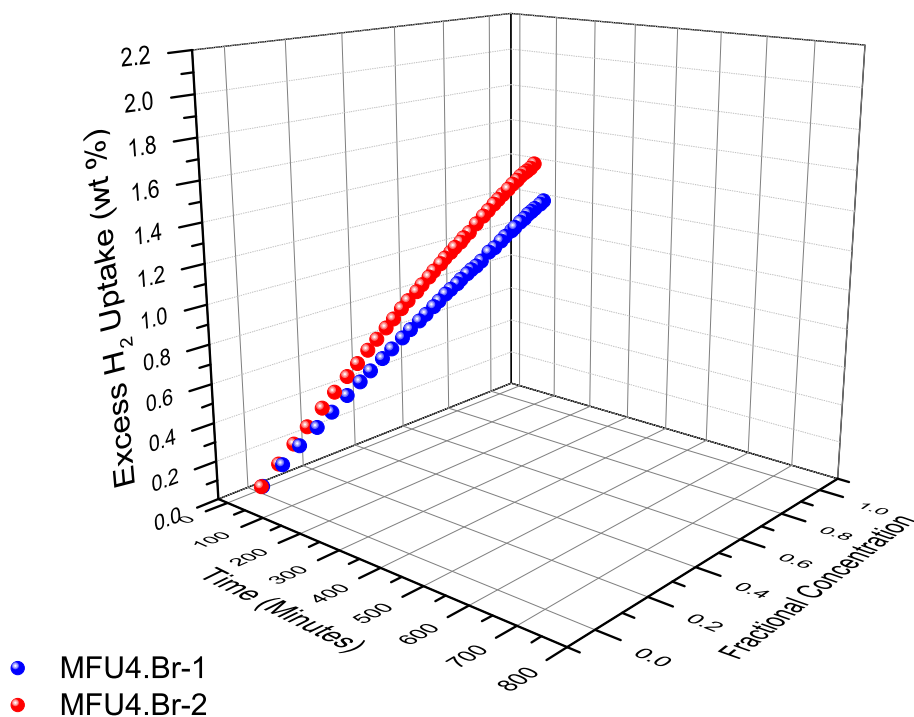


Figure 3.11: Kinetic Behavior Comparison between MFU4.Br-1 and MFU4.Br-2 at 127 K

As seen in Figures 3.7-3.11, measurement time become shorter for MFU4.Br-2 as the measurement temperature is increased. However, for MFU4.Br-1, the measurement time increases when the temperature has been increased to 87 K from 77 K. Additionally, the adsorbed amount difference between the samples decreases while the measurement temperature increasing. The exact values for uptake and durations are given, in the Table 3.2.

As seen in Table 3.2, the ratio of the times to complete measurements of the samples decreases with increasing temperature in the range of 77 K-97 K, and it increases as the temperature is increased further. At 77 K, the ratio is very high, because of the almost closed pore structure of MFU4.Br-1 does not allow H₂ molecules pass through the grains at that temperature. The ratio decreases steeply at 87 K, that it is because H₂ molecules pass through the grains and get adsorbed but the process is very slow. The ratio reaches its lowest value at 97 K, after 97 K it increases as the temperature increases. This indicates that the kinetics of MFU4.Br-1 is strongly affected by the increase in the temperature.

Table 3.2: H₂ uptake measurement completion time of MFU4.Br-1 and MFU4.Br-2.

	MFU4.Br-1	MFU4.Br-2	Ratio of the measurement times*
	(hrs)	(hrs)	
77 K	3.74	8.44	2.26
87 K	12.16	7.23	0.59
97 K	9.52	3.43	0.36
112 K	5.29	2.05	0.39
127 K	2.06	1.64	0.80
RT	28.43	28.44	1.00

*: Ratios have been calculated as ratio of MFU4.Br-2 to MFU4.Br-1.

MFU4.Br-2 has smaller average grain size than MFU4.Br-1, therefore it offers larger open surface, which increases the possibility of the entrance of H₂ molecules into the grains and provides the molecules get adsorbed in less diffusion lengths. This issue will be explained by the help of Figure 3.12;

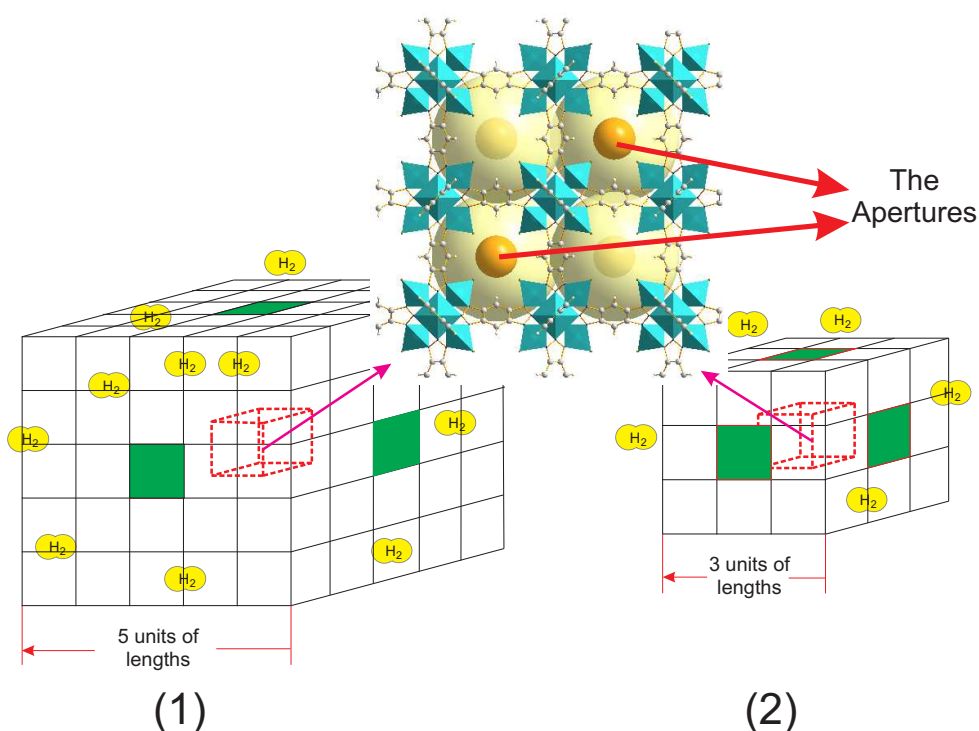


Figure 3.12: A depiction of diffusion ways for large and small grain.

In Figure 3.12, two different grains are given as large and small (1 and 2) with their 5 and 3 units of length, respectively. These grains are assumed to be consist of MFU4.Br

crystals. At the top of the figure, the crystal structure of MFU4.Br is given with its two possible voids for the adsorption of H₂ molecules: small cavities (orange spheres in the figure) and large cavities (pale yellow spheres in the figure). H₂ molecules should pass the narrow aperture (2.52 nm, apertures in the figure) between the small and large cavities, to continue to next cell, thus, fill up the grains.

In the scenario of filling the cell that exist in the middle of the grains in Figure 3.12, H₂ molecules should progress through the unit cells till the last cell is filled (the dashed cell in the figure), which means an amount of distances has to be covered in the grains will depend on the grain size. For example, to fill the grain 1 in Figure 3.12, for the first layer of cells $((5 + 4 + 4 + 3) \times 5) + 18) \times \frac{1}{2}$ unit length should be covered and, for the second layer of cells and last cell, $((3 + 2 + 2 + 1) \times 3) + 2) \times \frac{3}{2}$ and $(1) \times \frac{5}{2}$ units of length have to be progressed by H₂ molecules, respectively. Therefore to fill 125 unit cells 90.5 units of length has to be covered for the grain 1 in Figure 3.12. By using same evaluation to fill the grain 2, 14.5 units of length should be covered in total. For the same amount of masses of those two samples that amount of distance yields to, 2443.5 units of length (90.5×27) for the grain 1 and, 1812.5 units of length (14.5×125) in the grain 2 has to be covered. The longer units of distance means, there are more unit cells exist on the way to fill up grain 1, therefore more apertures, and empty/filled small cavities (those interrupt diffusion of H₂ molecules) need to be passed, in comparison to the grain 2. This approximation also convenient for MFU4.Br-1 and MFU4.Br-2 since their average grain size ratio (190/102, respectively) is close to grain size ratio of the samples (5/3) given in Figure 3.12. Therefore, H₂ adsorption process occurs faster in MFU4.Br-2 than MFU4.Br-1, since MFU4.Br-2 has smaller grain size than MFU4.Br-1. That also explains that MFU4.Br-1 requires longer measurement time to be filled.

In order to gather information of diffusing H₂ molecules in the samples at different temperatures, diffusivity of H₂ molecules are calculated.

Diffusion Calculations

To calculate the diffusion coefficients, natural logarithm of the ratio of concentrations to equilibrium concentrations at each step ($\ln(1 - (C/C_\infty))$) is calculated, and a plot is drawn, $\ln(1 - (C/C_\infty))$ against time that gives a line with slope $-\pi^2 D_c / r_c^2$.

To elucidate the calculation of diffusivity, a sequence of H₂ uptake kinetic data is shown in Figure 3.13:

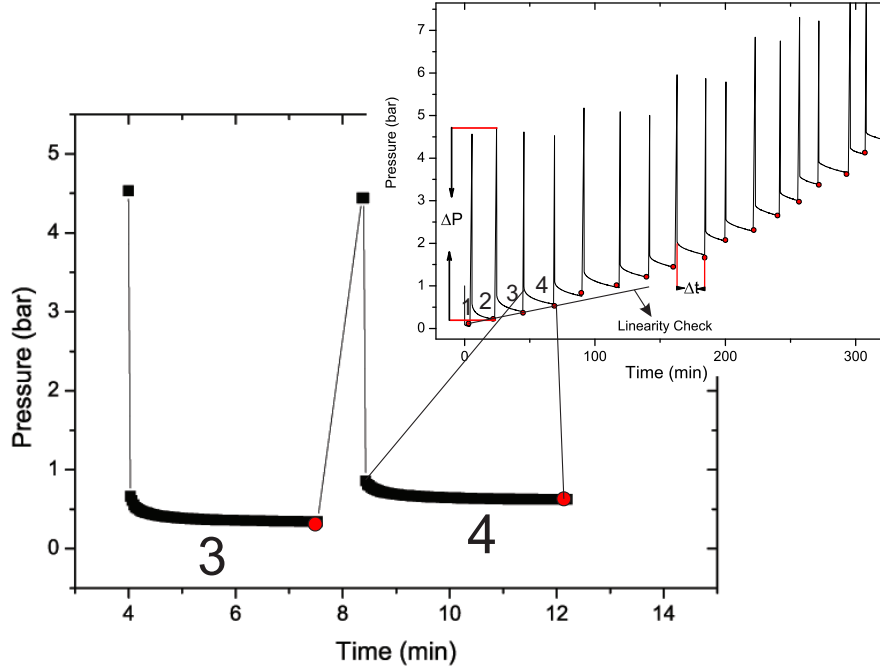


Figure 3.13: A visual depiction for the diffusion calculation.

As seen in Figure 3.13, uptake measurements consist of H₂ concentration checks at corresponding pressure and time. During a measurement, when concentration change is small enough, then the instrument “decides” equilibrium has been reached (red dots in Figure 3.12), therefore next H₂ loading step is applied. For the diffusion calculation, each concentration step is considered individually. For example, in the figure, step 4 has been magnified and each black point at magnified plot refers to H₂ concentration at corresponding pressure. Therefore, according to Equation (1.35) a plot of $\ln(1 - (C/C_{\infty_4}))$ (C refers to concentration, and C_{∞_4} refers to equilibrium concentration of step 4) is drawn that gives a straight line, and by multiplication of slope of that line with $4a^2/\pi$ (a is the mean particle size), diffusivity of H₂ molecules is obtained in that step.

It should be noted that the availability of these plots are limited up to pressures that the adsorption isotherm is linear. Since the linearity of the isotherms vary with the samples and the measurement temperatures, therefore, for each sample diffusion coefficient calculated at each step till the linearity of isotherm ends (see the linearity check on Figure 3.13), and the average value of the slope of each step is used to calculate the diffusivity of H₂ molecules at relevant measurement.

In Figure 3.14, a plot of $\ln(1 - (C/C_\infty))$ versus time at 127 K of MFU4.Br-1 is given;

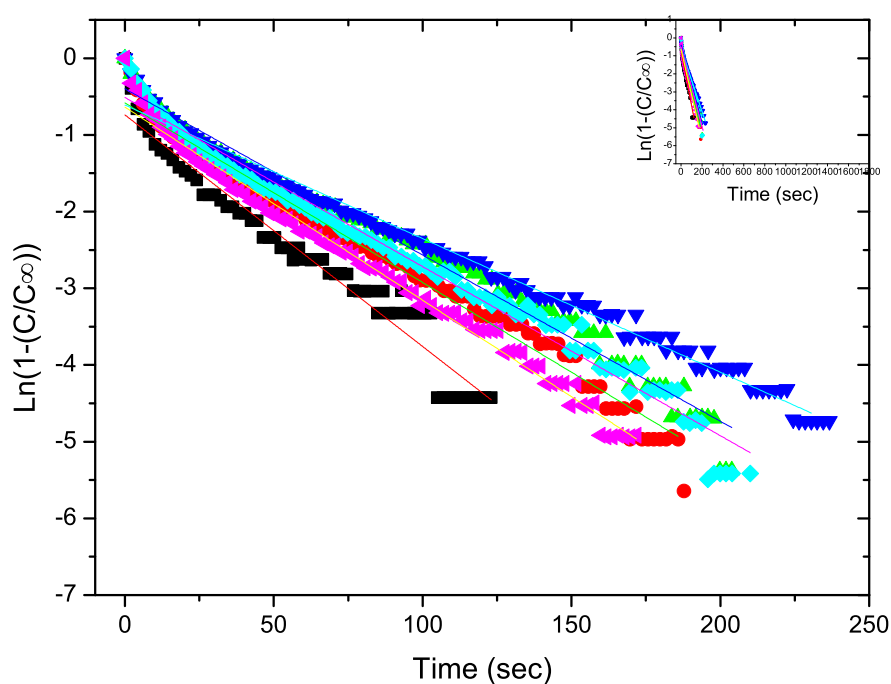


Figure 3.14: Plot of $\ln(1 - (C/C_\infty))$ versus time for MFU4.Br-1 at 127 K.

As it is seen in Figure 3.14, it consists of plots of $\ln(1 - (C/C_\infty))$ versus time for each step of the measurement. To calculate the diffusivity of MFU4.Br-1 at 127 K, these plots should be drawn within the linear region of its excess uptake isotherm. For MFU4.Br-1 at 127 K, the steps up to 1.67 bar have been chosen to calculate the diffusivity.

The remaining plots of $\ln(1 - (C/C_\infty))$ versus time of MFU4.Br-1 and MFU4.Br-2 at corresponding temperatures, are given in APPENDIX A.1 and A.2, respectively.

The slopes of those plots were obtained by line fitting, and results were multiplied with $4a^2/\pi$ (a is the mean particle size) to obtain the diffusion coefficients of the samples. The results are given in Table 3.3;

Table 3.3: Diffusion Coefficients of MFU4.Br-1 and MFU4.Br-2 at different temperatures.

	MFU4.Br-1 ($\text{cm}^2/\text{sec}^{-1}$)	MFU4.Br-2 ($\text{cm}^2/\text{sec}^{-1}$)
77 K	5.51×10^{-12}	1.05×10^{-12}
87 K	2.34×10^{-12}	1.95×10^{-12}
97 K	1.80×10^{-12}	2.77×10^{-12}
112 K	4.05×10^{-12}	6.34×10^{-12}
127 K	1.07×10^{-11}	1.27×10^{-11}

Diffusion coefficients compared between the samples at different temperatures in Figure 3.15;

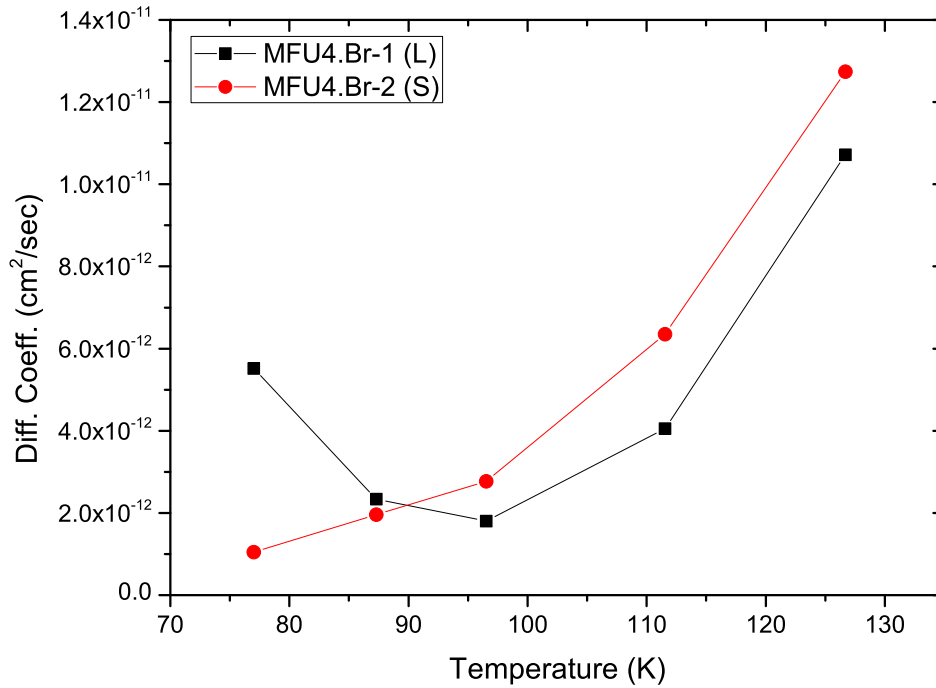


Figure 3.15: Diffusion Coefficients of MFU4.Br-1 and MFU4.Br-2 at different temperatures. L and S in the figure, indicate the mean particle size as large and small, respectively.

Figure 3.15 indicates that at 77 K, MFU4.Br-1 possesses higher diffusivity than MFU4.Br-2, which actually is a misleading result since both of the samples are in non-equilibrium state at 77 K (isotherms are not reversible at 77 K, Figures 3.2 and 3.4). Thus, for the same reason, it is not reasonable to compare diffusivity of the samples at 87 K and 97 K.

A comparison between the diffusivities of the samples at 112 K and 127 K can be done, since the adsorption measurements at 112 K and 127 K are reversible for both of the samples. As seen in Table 3.3, at 112 K and 127 K, diffusivity of H₂ molecules in MFU4.Br-2 is slightly higher than that of MFU4.Br-1. That is due to less kinetic barrier effect exist in MFU4.Br-2 having smaller average grain size. In Figure 3.15, it is clear that diffusion is a temperature controlled process, after reversible isotherm is obtained, diffusivity increases with increasing temperature for both of the samples.

4. CONCLUSION

In this study, H₂ adsorption of two samples of nanoporous MOF [Zn₅Br₄(BBTA)₃] MFU4.Br-1 and MFU4.Br-2 materials were studied using a PCTPro-2000 manometric adsorption device, produced by different production methods solvothermal, and microwave synthesis, respectively. The following conclusions have been obtained:

- H₂ uptake of MFU4.Br-2 is higher than MFU4.Br-1 at all measurement temperatures. The difference in the uptakes gets less pronounced as the measurement temperatures are increased. This is related with that large grains possess stronger kinetic blocking effect than the small grains and this blocking effect gets less effective as the temperature is increased.
- H₂ uptakes of MFU4.Br-1 and MFU4.Br-2 have been measured at 77 K, 87 K, 97 K, 112 K, 127 K and room temperature. The highest H₂ uptake of MFU4.Br-1 has been obtained at 97 K as 1.49 wt%, whereas MFU4.Br-2 shows the highest H₂ uptake at 87 K as 2.05 wt%.
- Grain size distribution of the samples, has an effect on where the adsorption isotherm will be reversible. For the sample MFU4.Br-1 has almost uniform grain size distribution of around 190 nm, hysteresis disappears at 112 K whereas for the sample MFU4.Br-2 containing bimodal distribution as small and large grains of about 50 nm and 200 nm respectively, the hysteresis disappears at 87 K.
- An unexpected difference in the uptakes of MFU4.Br-1 and MFU4.Br-2 have been observed at the temperatures where H₂ uptake is reversible, showing no hysteresis (112 K and 127 K).
- H₂ adsorption enthalpy of the samples has been calculated as $\sim 6 \text{ kJ mol}^{-1}$ from a limited range of uptake for MFU4.Br-1 whereas MFU4.Br-2 shows almost constant enthalpy over wide range of uptake. This almost constant enthalpy indicates diffusion is controlled by the small pores or apertures in the crystal structure.

- H₂ adsorption measurements take longer time in large grains, assigned as kinetic barrier effect is stronger in the larger grains since there are more apertures and/or voids (filled or empty) to fill the grains completely.
- Diffusivity of H₂ molecules in MFU4.Br-1 and MFU4.Br-2 has been calculated at 77 K, 87 K, 97 K, 112 K, and 127 K. The decreasing diffusion coefficient of MFU4.Br-1 with increasing temperature in the range of 77 K-97 K correlated with the temperature dependence of the kinetic barrier effect of the large grains.
- Diffusion coefficient increases with increasing temperature after the measurement of 97 K for MFU4.Br-1 whereas diffusion coefficient of MFU4.Br-2 increases at all measurement temperatures. The highest diffusivity in MFU4.Br-1 at 127 K has been determined to be $1.07 \times 10^{-11} \text{ cm}^2 \text{ s}^{-1}$ whereas in MFU4.Br-2 the diffusivity has been found to be $1.27 \times 10^{-11} \text{ cm}^2 \text{ s}^{-1}$.

REFERENCES

- [1] **Oakhire, O.**, 2012. Hydrogen Untapped Energy ?, Technical Report, IGEM, <http://www.igem.org.uk/media/232929/hydrogen-Report-Complete-web.pdf>, date retrieved: 10.01.2013.
- [2] **Thomas, C.E.**, 2009. Fuel cell and battery electric vehicles compared, *International Journal of Hydrogen Energy*, **34(15)**, 6005–6020.
- [3] 2013. Using the Existing Natural Gas System for Hydrogen, Technical Report, http://www.naturalhy.net/docs/Naturalhy_Brochure.pdf, date retrieved: 02.03.2013.
- [4] **Venera Barsaku**, 2011, Europe, Asia Plan Hydrogen Highways – U.S. Should Take Note, <http://fchea.posterous.com/europe-asia-plan-hydrogen-highways-us-should>.
- [5] **Broom, D.P.**, 2011. Hydrogen Storage Materials: The Characterisation of Their Storage Properties, Springer, 1st edition.
- [6] **Steele, B.C.H. and Heinzl, A.**, 2001. Materials for fuel-cell technologies, *Nature*, **414(6861)**, 345–352.
- [7] 2010, DOE Targets for Onboard Hydrogen Storage Systems for Light-Duty Vehicles, http://www1.eere.energy.gov/hydrogenandfuelcells/storage/pdfs/targets_onboard_hydro_storage.pdf. date retrieved: 10.03.2013.
- [8] **Schlapbach, L. and Züttel, A.**, 2001. Hydrogen-storage materials for mobile applications, *Nature*, **414(6861)**, 353–358.
- [9] **Farrusseng, D.**, editor, 2011. Metal-Organic Frameworks: Applications from Catalysis to Gas Storage, Wiley-VCH, 1 edition.
- [10] **Hua, T., Ahluwalia, R., Peng, J.K., Kromer, M., Lasher, S., McKenney, K., Law, K. and Sinha, J.**, 2011. Technical assessment of compressed hydrogen storage tank systems for automotive applications, *International Journal of Hydrogen Energy*, **36(4)**, 3037–3049.
- [11] **Ahluwalia, R., Hua, T. and Peng, J.**, 2012. On-board and Off-board performance of hydrogen storage options for light-duty vehicles, *International Journal of Hydrogen Energy*, **37(3)**, 2891–2910.
- [12] **Züttel, A.**, 2003. Materials for hydrogen storage, *Materials Today*, **6(9)**, 24–33.

- [13] **Eberle, U., Felderhoff, M. and Schüth, F.**, 2009. Chemical and Physical Solutions for Hydrogen Storage, *Angewandte Chemie International Edition*, **48(36)**, 6608–6630.
- [14] **Sakintuna, B., Lamari-Darkrim, F. and Hirscher, M.**, 2007. Metal hydride materials for solid hydrogen storage: A review, *International Journal of Hydrogen Energy*, **32(9)**, 1121–1140.
- [15] **Müller, K., Stark, K., Müller, B. and Arlt, W.**, 2012. Amine borane based hydrogen carriers: An evaluation, *Energy and Fuels*, **26(6)**, 3691–3696.
- [16] **Wagemans, R.W.P., van Lenthe, J.H., de Jongh, P.E., van Dillen, A.J. and de Jong, K.P.**, 2005. Hydrogen Storage in Magnesium Clusters: Quantum Chemical Study, *Journal of the American Chemical Society*, **127(47)**, 16675–16680.
- [17] **Hirscher, M.**, editor, 2010. Handbook of Hydrogen Storage, Wiley-VCH, 1 edition.
- [18] **Ruthven, D.M.**, 1984. Principles of Adsorption and Adsorption Processes, Wiley-Blackwell.
- [19] **Murata, K., Kaneko, K., Kokai, F., Takahashi, K., Yudasaka, M. and Iijima, S.**, 2000. Pore structure of single-wall carbon nanohorn aggregates, *Chemical Physics Letters*, **331(1)**, 14–20.
- [20] **Suh, M.P., Park, H.J., Prasad, T.K. and Lim, D.W.**, 2012. Hydrogen Storage in Metal–Organic Frameworks, *Chemical Reviews*, **112(2)**, 782–835.
- [21] **Rosi, N.L., Eckert, J., Eddaoudi, M., Vodak, D.T., Kim, J., O’Keeffe, M. and Yaghi, O.M.**, 2003. Hydrogen Storage in Microporous Metal–Organic Frameworks, *Science*, **300(5622)**, 1127–1129.
- [22] **Streppel, B.**, 2011. Hydrogen adsorption on metal-organic frameworks, Ph.D. thesis, Universität Stuttgart, Retrieved from <http://elib.uni-stuttgart.de/opus/volltexte/2011/6502/>.
- [23] **Sing, K.S.W.**, 1985. Reporting physisorption data for gas/solid systems with special reference to the determination of surface area and porosity (Recommendations 1984), *Pure and Applied Chemistry*, **57(4)**, 603–619.
- [24] **Masel, R.I.**, 1996. Principles of Adsorption and Reaction on Solid Surfaces, Wiley-Interscience, 1 edition.
- [25] **Brunauer, S., Emmett, P.H. and Teller, E.**, 1938. Adsorption of Gases in Multimolecular Layers, *Journal of the American Chemical Society*, **60(2)**, 309–319.
- [26] **Lowell, S., Shields, J.E., Thomas, M.A. and Thommes, M.**, 2006. Characterization of Porous Solids and Powders: Surface Area, Pore Size and Density, Springer.

- [27] **Walton, K.S. and Snurr, R.Q.**, 2007. Applicability of the BET Method for Determining Surface Areas of Microporous Metal-Organic Frameworks, *Journal of the American Chemical Society*, **129(27)**, 8552–8556.
- [28] **Callister, W.D. and , R.**, 2011. Materials science and engineering, Wiley, Hoboken, NJ.
- [29] **Crank, J.**, 1979. The Mathematics Diffusion, Oxford University Press.
- [30] **Duong, D.D.**, 1998. Adsorption Analysis: Equilibria and Kinetics, Imperial College Press.
- [31] **Ziller, M. and Miller, R.**, 1986. On the solution of diffusion controlled adsorption kinetics by means of orthogonal collocation, *Colloid and Polymer Science*, **264(7)**, 611–615.
- [32] **Shewmon, P.**, 1989. Diffusion in Solids, Wiley, 2 edition.
- [33] **Einstein, A.**, 2011. Investigations on the Theory of the Brownian Movement, BN Publishing.
- [34] **Adhangale, P. and Keffer, D.J.**, 2004. Obtaining transport diffusion coefficients from self-diffusion coefficients in nanoporous adsorption systems, *Molecular Physics*, **102(5)**, 471–483.
- [35] **Denysenko, D., Grzywa, M., Tonigold, M., Streppel, B., Krkljus, I., Hirscher, M., Mugnaioli, E., Kolb, U., Hanss, J. and Volkmer, D.**, 2011. Elucidating Gating Effects for Hydrogen Sorption in MFU-4-Type Triazolate-Based Metal–Organic Frameworks Featuring Different Pore Sizes, *Chemistry – A European Journal*, **17(6)**, 1837–1848.
- [36] **Karger, J., Kärger, J., Ruthven, D.M. and Theodorou, D.N.**, 2012. Diffusion in Nanoporous Materials, John Wiley & Sons.
- [37] **Cejka, J., Bekkum, H.v., Corma, A. and Schueth, F.**, 2007. Introduction to Zeolite science and practice, Volume 168, Third Edition, Elsevier Science, 3 edition.
- [38] **Gruener, S. and Huber, P.**, 2008. Knudsen Diffusion in Silicon Nanochannels, *Physical Review Letters*, **100(6)**, 064502.
- [39] **<Url-1>Knudsen diffusion**, http://en.wikipedia.org/w/index.php?title=Knudsen_diffusion&oldid=555995585, Date Retrieved: 04.06.2013
- [40] **Roque-Malherbe, R.M.**, 2007. Adsorption and diffusion in nanoporous materials, Taylor & Francis, Boca Raton.
- [41] **Cunningham, R.**, 1980. Diffusion in Gases and Porous Media, Plenum Press, 1 edition.
- [42] **Kärger, J. and Ruthven, D.M.**, 1992. Diffusion in zeolites and other microporous solids, Wiley.

- [43] **Garg, D. and Ruthven, D.**, 1972. The effect of the concentration dependence of diffusivity on zeolitic sorption curves, *Chemical Engineering Science*, **27(2)**, 417–423.
- [44] **Baerlocher, C., McCusker, L.B. and Olson, D.H.**, 2007. Atlas of Zeolite Framework Types, Sixth Edition, Elsevier Science, 6 edition.
- [45] <Url-2>Zeolite, <http://en.wikipedia.org/w/index.php?title=Zeolite&oldid=573296299>, Date retrieved: 05.06.2013
- [46] **MacGillivray, L.R.**, editor, 2010. Metal-Organic Frameworks: Design and Application, Wiley, 1 edition.
- [47] **Walker, G. and Institute of Materials, M.**, 2008. Solid-state hydrogen storage: materials and chemistry, Woodhead Pub. ; Maney Pub. ; CRC Press, Cambridge, England; [England?]; Boca Raton, FL.
- [48] **Tranchemontagne, D.J., Mendoza-Cortés, J.L., O’Keeffe, M. and Yaghi, O.M.**, 2009. Secondary building units, nets and bonding in the chemistry of metal–organic frameworks, *Chemical Society Reviews*, **38(5)**, 1257–1283.
- [49] **Rowsell, J.L.C. and Yaghi, O.M.**, 2005. Strategies for Hydrogen Storage in Metal–Organic Frameworks, *Angewandte Chemie International Edition*, **44(30)**, 4670–4679.
- [50] **Furukawa, H., Miller, M.A. and Yaghi, O.M.**, 2007. Independent verification of the saturation hydrogen uptake in MOF-177 and establishment of a benchmark for hydrogen adsorption in metal–organic frameworks, *Journal of Materials Chemistry*, **17(30)**, 3197–3204.
- [51] **Aromí, G., Barrios, L.A., Roubeau, O. and Gamez, P.**, 2011. Triazoles and tetrazoles: Prime ligands to generate remarkable coordination materials, *Coordination Chemistry Reviews*, **255(5–6)**, 485–546.
- [52] **Biswas, S., Grzywa, M., Nayek, H.P., Dehnen, S., Senkovska, I., Kaskel, S. and Volkmer, D.**, 2009. A cubic coordination framework constructed from benzobistriazolate ligands and zinc ions having selective gas sorption properties, *Dalton Transactions*, **(33)**, 6487–6495.
- [53] **Nijem, N.**, 2012. Molecular interactions in metal organic frameworks for optimized gas separation, storage and sensing applications, Ph.D., The University of Texas at Dallas, United States – Texas, <http://search.proquest.com/docview/1074792089/abstract/13C3B2BC25C773CB7D5/20?accountid=105221>.
- [54] **Mulder, F.M., Assfour, B., Huot, J., Dingemans, T.J., Wagemaker, M. and Ramirez-Cuesta, A.J.**, 2010. Hydrogen in the Metal-Organic Framework Cr MIL-53, *The Journal of Physical Chemistry C*, **114(23)**, 10648–10655.

- [55] **Fletcher, A.J., Thomas, K.M. and Rosseinsky, M.J.**, 2005. Flexibility in metal-organic framework materials: Impact on sorption properties, *Journal of Solid State Chemistry*, **178(8)**, 2491–2510.
- [56] **Serra-Crespo, P., Gobechiya, E., Ramos-Fernandez, E.V., Juan-Alcañiz, J., Martinez-Joaristi, A., Stavitski, E., Kirschhock, C.E.A., Martens, J.A., Kapteijn, F. and Gascon, J.**, 2012. Interplay of Metal Node and Amine Functionality in NH₂-MIL-53: Modulating Breathing Behavior through Intra-framework Interactions, *Langmuir*, **28(35)**, 12916–12922.
- [57] **Kitagawa, S. and Uemura, K.**, 2005. Dynamic porous properties of coordination polymers inspired by hydrogen bonds, *Chemical Society Reviews*, **34(2)**, 109–119.
- [58] **Férey, G. and Serre, C.**, 2009. Large breathing effects in three-dimensional porous hybrid matter: facts, analyses, rules and consequences, *Chemical Society Reviews*, **38(5)**, 1380–1399.
- [59] **Liu, Y., Her, J.H., Dailly, A., Ramirez-Cuesta, A.J., Neumann, D.A. and Brown, C.M.**, 2008. Reversible Structural Transition in MIL-53 with Large Temperature Hysteresis, *Journal of the American Chemical Society*, **130(35)**, 11813–11818.
- [60] **Tanaka, D., Nakagawa, K., Higuchi, M., Horike, S., Kubota, Y., Kobayashi, T.C., Takata, M. and Kitagawa, S.**, 2008. Kinetic Gate-Opening Process in a Flexible Porous Coordination Polymer, *Angewandte Chemie International Edition*, **47(21)**, 3914–3918.
- [61] **Triguero, C., Coudert, F.X., Boutin, A., Fuchs, A.H. and Neimark, A.V.**, 2011. Mechanism of Breathing Transitions in Metal–Organic Frameworks, *The Journal of Physical Chemistry Letters*, **2(16)**, 2033–2037.
- [62] **Fairen-Jimenez, D., Moggach, S.A., Wharmby, M.T., Wright, P.A., Parsons, S. and Düren, T.**, 2011. Opening the Gate: Framework Flexibility in ZIF-8 Explored by Experiments and Simulations, *Journal of the American Chemical Society*, **133(23)**, 8900–8902.
- [63] **Kang, J., Wei, S.H. and Kim, Y.H.**, 2010. Microscopic Theory of Hysteretic Hydrogen Adsorption in Nanoporous Materials, *Journal of the American Chemical Society*, **132(5)**, 1510–1511.
- [64] **Fletcher, A.J., Cussen, E.J., Bradshaw, D., Rosseinsky, M.J. and Thomas, K.M.**, 2004. Adsorption of Gases and Vapors on Nanoporous Ni₂(4,4'-Bipyridine)₃(NO₃)₄ Metal-Organic Framework Materials Templated with Methanol and Ethanol: Structural Effects in Adsorption Kinetics, *Journal of the American Chemical Society*, **126(31)**, 9750–9759.
- [65] **Teufel, J., Oh, H., Hirscher, M., Wahiduzzaman, M., Zhechkov, L., Kuc, A., Heine, T., Denysenko, D. and Volkmer, D.**, 2013. MFU-4 – A Metal-Organic Framework for Highly Effective H₂/D₂ Separation, *Advanced Materials*, **25(4)**, 635–639.

- [66] **Antonio de la, H. and Loupy, A.**, 2012. *Microwaves in Organic Synthesis*, volume 1, Wiley-VCH, Weinheim.
- [67] **Kubo, M., Shimojima, A. and Okubo, T.**, 2012. Effect of Lithium Doping into MIL-53(Al) through Thermal Decomposition of Anion Species on Hydrogen Adsorption, *The Journal of Physical Chemistry C*, **116(18)**, 10260–10265.
- [68] **Lee, Y.G., Moon, H.R., Cheon, Y.E. and Suh, M.P.**, 2008. A Comparison of the H₂ Sorption Capacities of Isostructural Metal–Organic Frameworks With and Without Accessible Metal Sites: [Zn₂(abtc)(dmf)₂₃] and [Cu₂(abtc)(dmf)₂₃] versus [Cu₂(abtc)₃], *Angewandte Chemie International Edition*, **47(40)**, 7741–7745.
- [69] **Park, H.J. and Suh, M.P.**, 2008. Mixed-Ligand Metal–Organic Frameworks with Large Pores: Gas Sorption Properties and Single-Crystal-to-Single-Crystal Transformation on Guest Exchange, *Chemistry – A European Journal*, **14(29)**, 8812–8821.
- [70] **Li, Y., Xie, L., Liu, Y., Yang, R. and Li, X.**, 2008. Favorable Hydrogen Storage Properties of M(HBTC)(4,4'-bipy) .3DMF (M = Ni and Co), *Inorganic Chemistry*, **47(22)**, 10372–10377.
- [71] **Lee, J.Y., Pan, L., Kelly, S.P., Jagiello, J., Emge, T.J. and Li, J.**, 2005. Achieving High Density of Adsorbed Hydrogen in Microporous Metal Organic Frameworks, *Advanced Materials*, **17(22)**, 2703–2706.
- [72] **Jia, J., Lin, X., Wilson, C., Blake, A.J., Champness, N.R., Hubberstey, P., Walker, G., Cussen, E.J. and Schröder, M.**, 2007. Twelve-connected porous metal–organic frameworks with high H₂ adsorption, *Chemical Communications*, **(8)**, 840–842.
- [73] **Senkovska, I. and Kaskel, S.**, 2006. Solvent-Induced Pore-Size Adjustment in the Metal–Organic Framework [Mg₃(ndc)₃(dmf)₄] (ndc = naphthalenedicarboxylate), *European Journal of Inorganic Chemistry*, **2006(22)**, 4564–4569.
- [74] **Saha, D., Deng, S. and Yang, Z.**, 2009. Hydrogen adsorption on metal-organic framework (MOF-5) synthesized by DMF approach, *Journal of Porous Materials*, **16(2)**, 141–149.
- [75] **Saha, D., Wei, Z. and Deng, S.**, 2008. Equilibrium, kinetics and enthalpy of hydrogen adsorption in MOF-177, *International Journal of Hydrogen Energy*, **33(24)**, 7479–7488.
- [76] **Hart, H. and Ok, D.**, 1986. Synthesis of 1,5-diamino-1,5-dihydrobenzo[1,2-d:4,5-d']bistriazole (DABT) and its use as a 1,4-benzadiyne equivalent, *The Journal of Organic Chemistry*, **51(7)**, 979–986.

- [77] **Zhao, D., Yuan, D., Krishna, R., Baten, J.M.v. and Zhou, H.C.**, 2010. Thermosensitive gating effect and selective gas adsorption in a porous coordination nanocage, *Chemical Communications*, **46(39)**, 7352–7354.
- [78] **Yang, S., Martin, G.S.B., Titman, J.J., Blake, A.J., Allan, D.R., Champness, N.R. and Schröder, M.**, 2011. Pore with Gate: Enhancement of the Isothermic Heat of Adsorption of Dihydrogen via Postsynthetic Cation Exchange in Metal-Organic Frameworks, *Inorganic Chemistry*, **50(19)**, 9374–9384.

APPENDICES

APPENDIX A.1 : The plots of $\ln(1 - (C/C_\infty))$ versus time at the measurement temperatures (MFU4.Br-1)

APPENDIX A.2 : The plots of $\ln(1 - (C/C_\infty))$ versus time at the measurement temperatures (MFU4.Br-2)

APPENDIX A.1

The plots of $\ln(1 - (C/C_\infty))$ versus time for MFU4.Br-1 at the temperatures between 77 K-127 K, are given below.

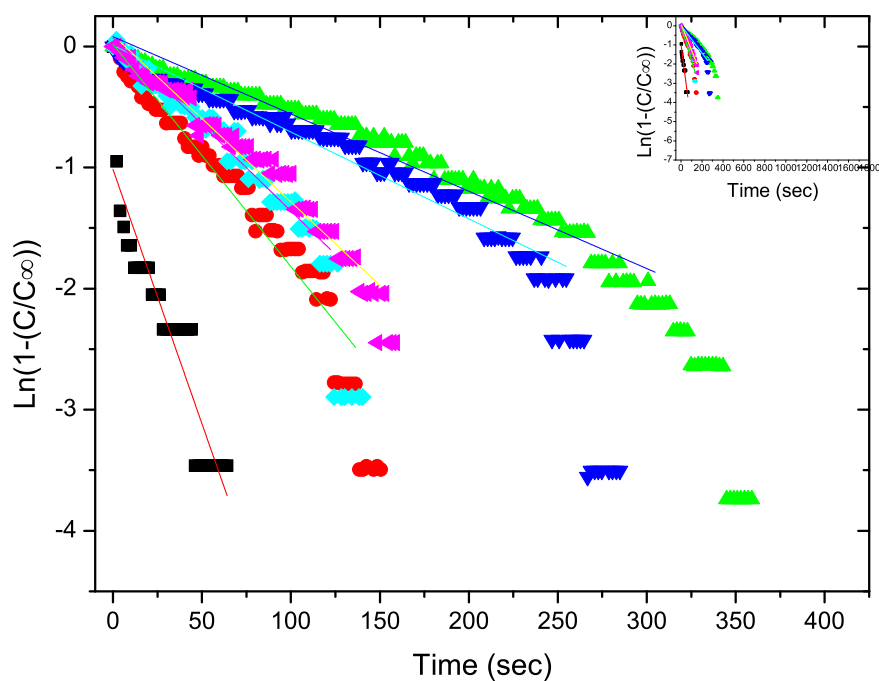


Figure A.1: Plot of $\ln(1 - (C/C_\infty))$ versus time for MFU4.Br-1 at 77 K.

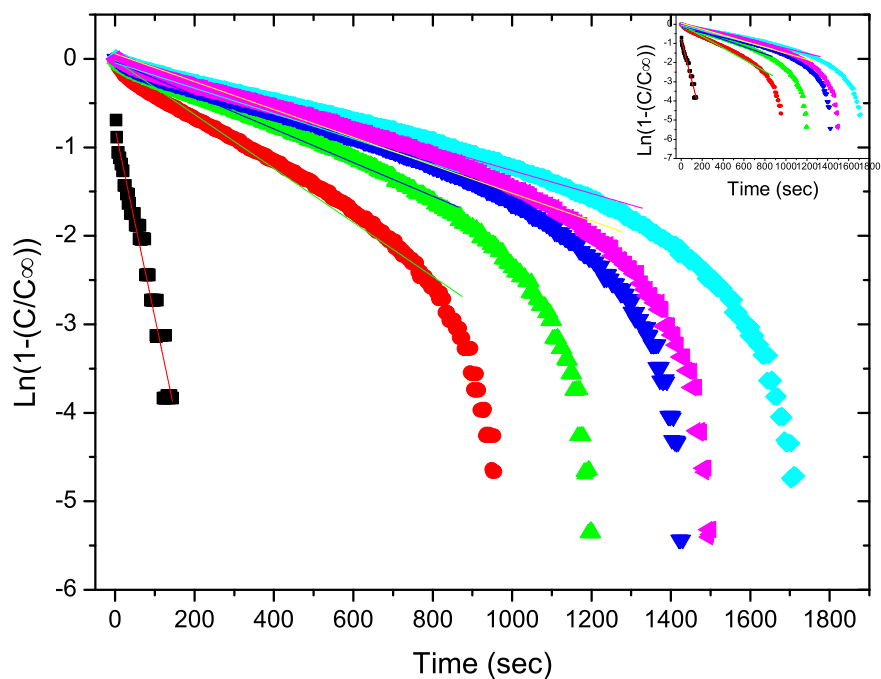


Figure A.2: Plot of $\ln(1 - (C/C_\infty))$ versus time for MFU4.Br-1 at 87 K.

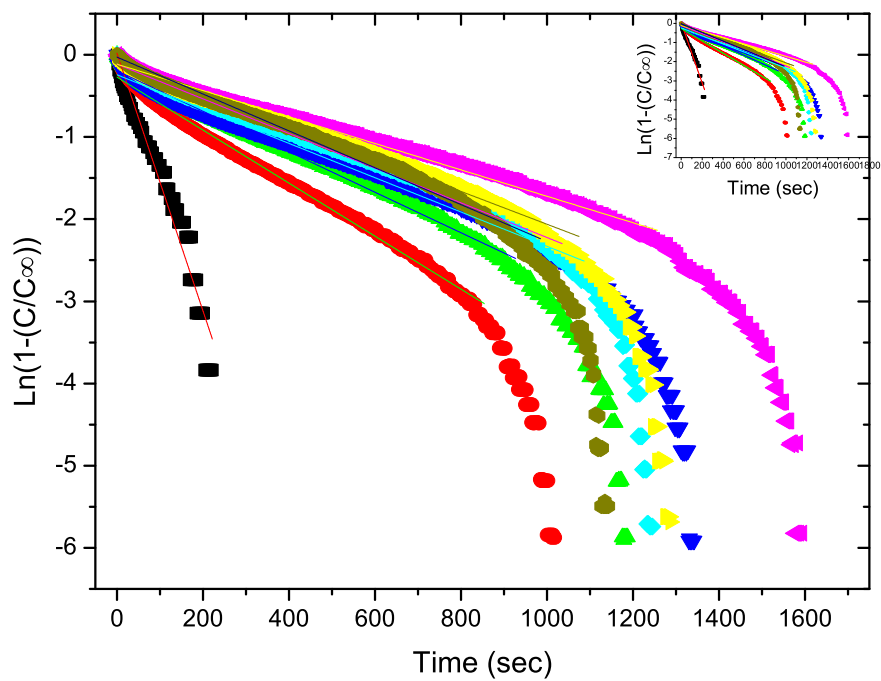


Figure A.3: Plot of $\ln(1 - (C/C_\infty))$ versus time for MFU4.Br-1 at 97 K.

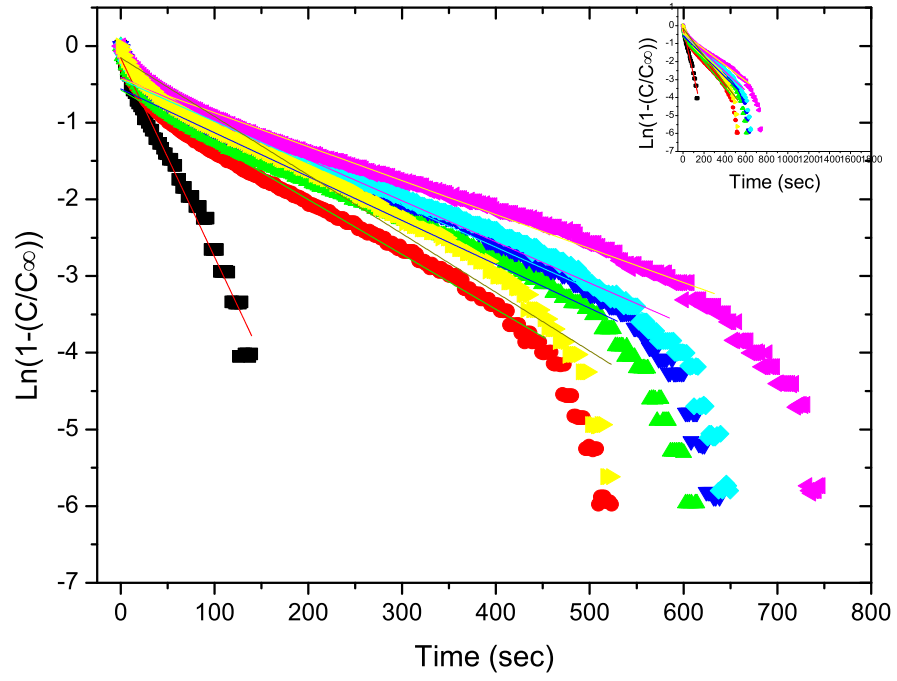


Figure A.4: Plot of $\ln(1 - (C/C_\infty))$ versus time for MFU4.Br-1 at 112 K.

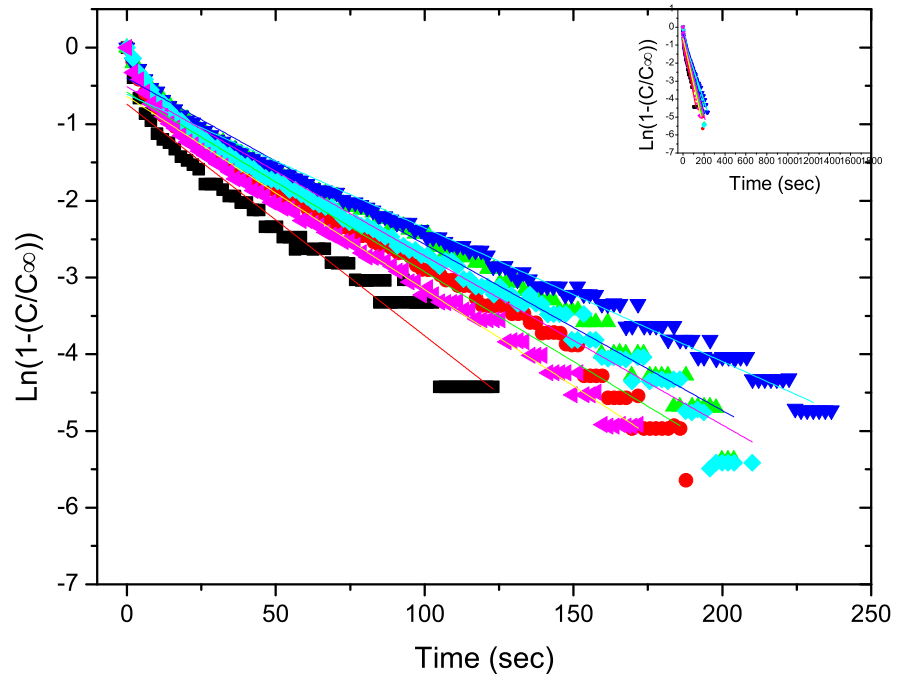


Figure A.5: Plot of $\ln(1 - (C/C_\infty))$ versus time for MFU4.Br-1 at 127 K.

APPENDIX A.2

The plots of $\ln(1 - (C/C_\infty))$ versus time for MFU4.Br-2 at the temperatures between 77 K-127 K, are given below.

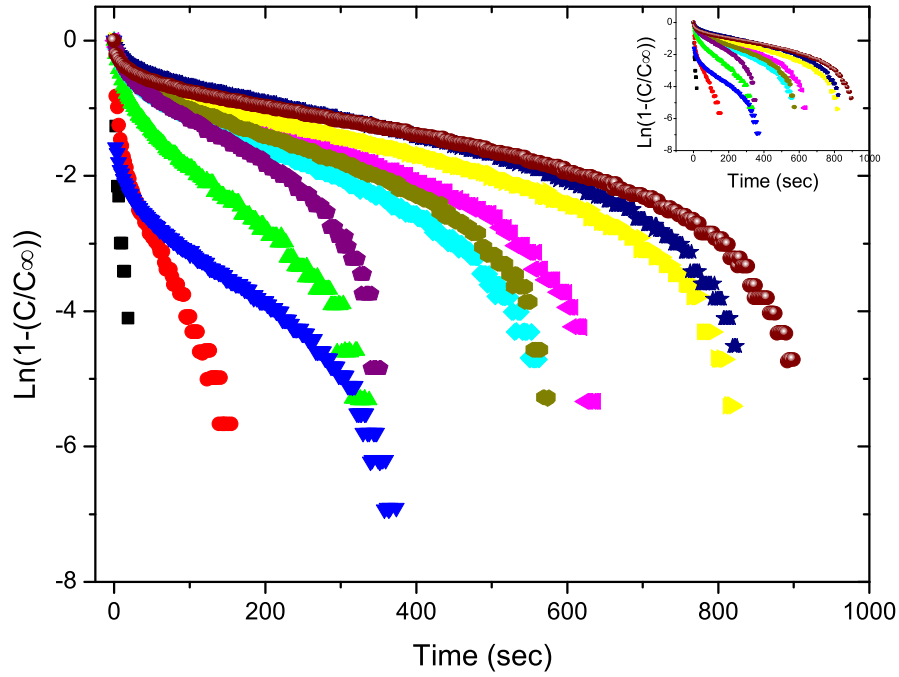


Figure A.6: Plot of $\ln(1 - (C/C_\infty))$ versus time for MFU4.Br-2 at 77 K.

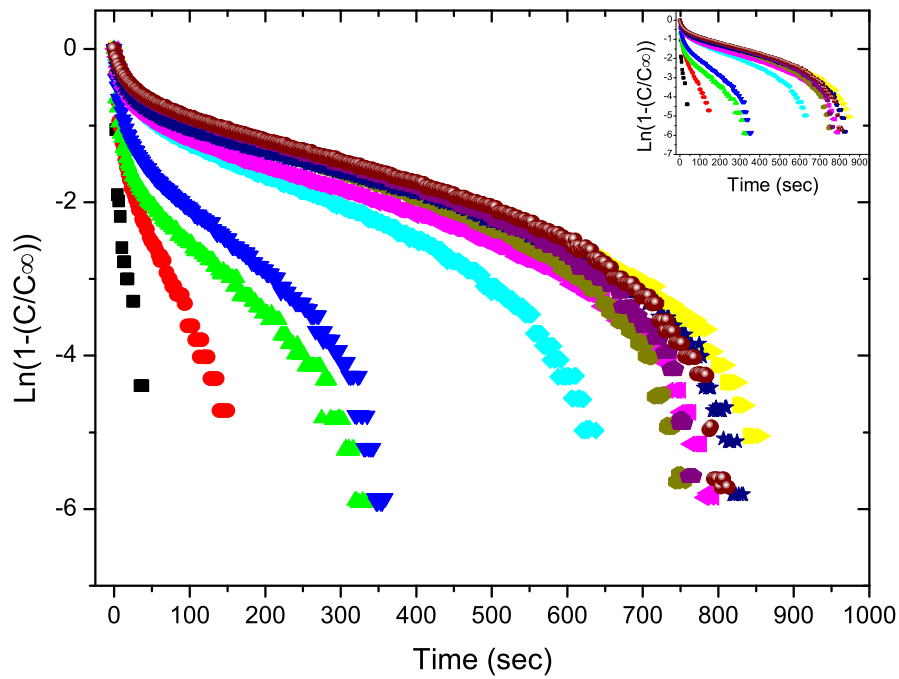


Figure A.7: Plot of $\ln(1 - (C/C_\infty))$ versus time for MFU4.Br-2 at 87 K.

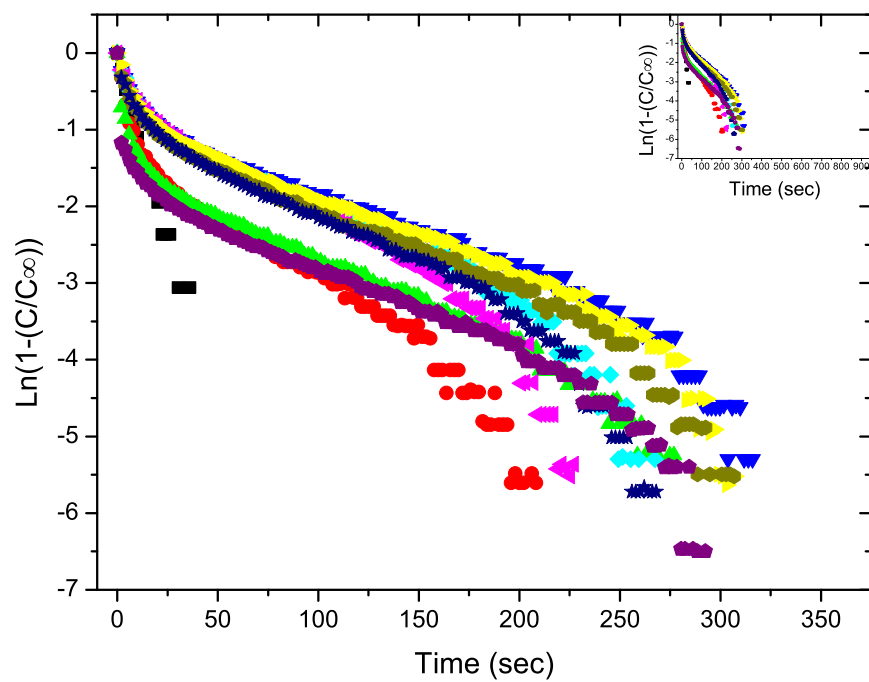


Figure A.8: Plot of $\ln(1 - (C/C_\infty))$ versus time for MFU4.Br-2 at 97 K.

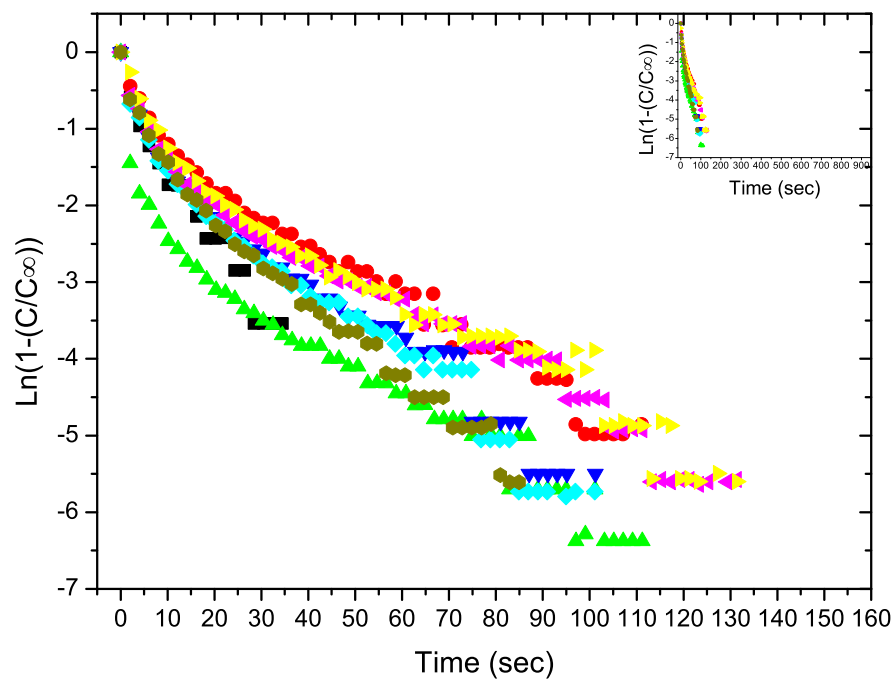


Figure A.9: Plot of $\ln(1 - (C/C_\infty))$ versus time for MFU4.Br-2 at 112 K.

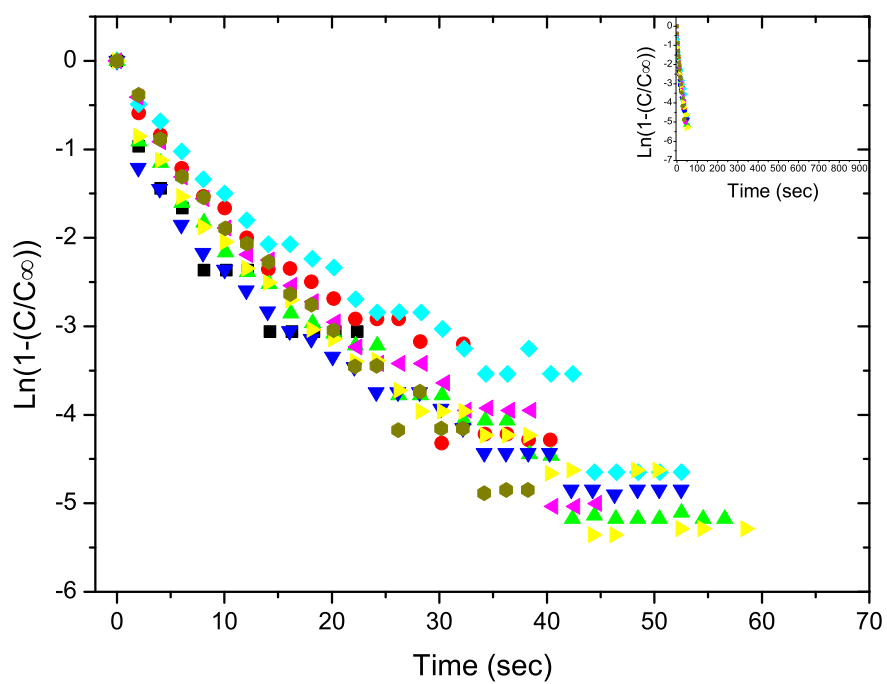
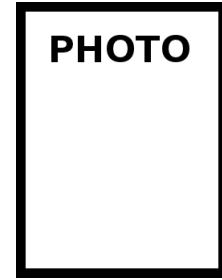


Figure A.10: Plot of $\ln(1 - (C/C_\infty))$ versus time for MFU4.Br-2 at 127 K.

CURRICULUM VITAE



Name Surname: Fatih KUZAK

Place and Date of Birth: Bursa, 29.06.1988

Adress: Konak cad. Fırat sk. Nilüfer Apt. No:7 Nilüfer/BURSA 16110

E-Mail: fkuzak@itu.edu.tr

B.Sc.: 2006-2010 Sakarya University Metallurgical and Materials Engineering

M.Sc.: 2010-Present, Istanbul Technical University, Materials Engineering

Professional Experience and Rewards: